

Computational Modelling and Experimental Evaluation of Fluid and Mass Transport in Lymph Node with Implications in Inflammation

A Thesis

by

Mohammad Jafarnejad

Imperial College London
Department of Bioengineering
Prince Consort Road
London SW7 2AZ

This thesis is submitted for the degree of Doctor of Philosophy of
Imperial College London.

2016

ABSTRACT

The lymphatic system plays a critical role in normal physiology and is associated with pathologies from lymphoedema to cancer metastasis. A primary role of the lymphatic system is to transport lymph containing pathogens and immune cells from tissues to lymph nodes (LNs) where humoral and cellular adaptive immune response is initiated. Despite the importance of fluid and proteins transport to specific regions of the LN in proper immune response, little is known about fluid distribution and its modulation under different pathologic conditions such as inflammation.

Four studies in this thesis set out to improve our understanding of how lymph transport in the LN modulates its function. The first study established a computational model of fluid flow in the LN demonstrating its important role in fluid exchange with blood vessels, and determined medulla hydraulic conductivity as the key parameter for controlling hydraulic resistance of the LN. In the second study, the experimentally measured LN resistance showed an increase after inflammation, which was associated with medulla hydraulic conductivity. The third study demonstrated an application of this model in providing insight into the role of lymph transport in formation of interfollicular chemokine gradients in the LN that are crucial for antigen presenting cell entry to LN paracortex. In the fourth study, the effect of shear stress that is present in the sinuses of the LN was examined on the calcium dynamics of the lymphatic endothelium.

Overall, this research revealed that lymph flow both modulates (e.g. chemokine gradient formation and calcium signalling) and is modulated by (e.g. hydraulic resistance change with inflammation) LN function. The lymph flow plays a critical role in fluid balance and immune response and has a great potential as a therapeutic target for modulating immune response.

“It seems that for success in science or art, a dash of autism is essential.”

Dr. Hans Asperger (1906 - 1980)

TABLE OF CONTENTS

	Page
ABSTRACT.....	2
TABLE OF CONTENTS.....	4
DEDICATION.....	8
ACKNOWLEDGEMENTS	9
ORIGINALITY AND CONTRIBUTION STATEMENT.....	13
COPYRIGHT DECLARATION	15
ASSOCIATED PUBLICATIONS.....	16
LIST OF ABBREVIATIONS.....	19
LIST OF FIGURES	23
LIST OF TABLES.....	25
CHAPTER	
1 INTRODUCTION AND BACKGROUND.....	27
1.1. Introduction.....	28
1.2. Specific Aims	31
1.3. Background.....	32
1.3.1. Pathologies Associated with the Lymphatic System	32
1.3.2. Anatomy of the Lymphatic System	35
1.3.2.1. Initial Lymphatics.....	36
1.3.2.2. Pre-collectors and Collecting Lymphatic Vessels	37
1.3.2.3. Lymph Nodes.....	39
1.3.3. Immune Response in Lymph Nodes.....	40
1.3.4. Lymph Node Chemokines and Their Receptors	41
1.3.4.1. Ligands	42
1.3.4.2. Receptors.....	43
1.3.5. Computational Modelling in Lymphatic System	45

2	MODELING LYMPH FLOW AND FLUID EXCHANGE WITH BLOOD VESSELS IN LYMPH NODES.....	49
	2.1. Introduction.....	50
	2.2. Methods.....	52
	2.2.1. Geometry Model.....	52
	2.2.2. Computational Fluid Dynamics.....	54
	2.2.3. Animals.....	56
	2.2.4. In vivo Labelling.....	57
	2.2.5. LN Clearing and Whole Organ Imaging.....	57
	2.2.6. Blood Vessel Segmentation.....	57
	2.2.7. Parameter Estimation.....	58
	2.2.8. Parameter Sensitivity Analysis.....	59
	2.3. Results.....	60
	2.3.1. Flow Patterns under Baseline Conditions.....	60
	2.3.2. Parameter Sensitivity Analysis.....	63
	2.4. Discussion.....	68
3	EXPERIMENTAL MEASUREMENT OF THE HYDRAULIC RESISTANCE OF MOUSE POPLITEAL LYMPH NODE.....	79
	3.1. Introduction.....	80
	3.2. Methods.....	84
	3.2.1. Mouse Popliteal LN Isolation and Cannulation.....	84
	3.2.2. Footpad Injection of TLR Agonists.....	85
	3.2.3. LN Resistance Measurement Apparatus.....	86
	3.2.4. LN Flow Model.....	88
	3.2.5. Statistical Analysis.....	88
	3.3. Results.....	89
	3.3.1. Measurement of the Resistance of Mouse Popliteal LN.....	89
	3.3.2. Hydraulic Conductivity of Medulla Determines LN Resistance.....	91
	3.3.3. Higher LN Resistance Results in Greater Central Flow.....	92
	3.4. Discussion.....	94

4	DEVELOPMENT OF A COMPUTATIONAL MODEL FOR TRANSPORT OF CHEMOKINES AND FORMATION OF GRADIENTS IN LYMPH NODE	101
	4.1. Introduction.....	102
	4.2. Methods.....	106
	4.2.1. Modelling LN Fluid Transport.....	106
	4.2.2. Chemokine Transport.....	106
	4.2.3. CCL21 Binding to Matrix.....	108
	4.2.4. CCR7 Binding Dynamics.....	109
	4.2.5. ACKR4-mediated Chemokine Degradation.....	111
	4.2.6. Chemokine Transport to Blood Vessels.....	113
	4.2.7. Parameter Estimation.....	114
	4.2.8. Parameter Sensitivity Analysis.....	117
	4.2.9. Concentration Difference Calculation Across Cells.....	118
	4.3. Results.....	118
	4.3.1. Chemokine Gradient Formation under Baseline Conditions ...	118
	4.3.2. Parameter Sensitivity Analysis.....	121
	4.3.3. Role of ACKR4 in LN versus Collecting Lymphatic Vessels ...	124
	4.3.4. Bound CCL21 Gradient Requires either LN ACKR4 or Afferent Flow.....	126
	4.3.5. Cell Size Matters.....	128
	4.4. Discussion.....	129
5	MEASUREMENT OF SHEAR STRESS-MEDIATED INTRACELLULAR CALCIUM DYNAMICS IN HUMAN DERMAL LYMPHATIC ENDOTHELIAL CELLS	137
	5.1. Introduction.....	138
	5.2. Methods.....	140
	5.2.1. Cell Culture.....	140
	5.2.2. Shear Stress Apparatus.....	142
	5.2.3. Calcium Measurement.....	143
	5.2.4. Curve-fits.....	144
	5.2.5. Statistical Analysis.....	145
	5.3. Results.....	145
	5.3.1. $[Ca^{2+}]_i$ Dynamics in HDLEC Is Shear Stress Sensitive.....	145

5.3.2. Contribution of Intracellular Calcium Release versus Extracellular Calcium Entry	148
5.3.3. Intracellular Calcium Release Is Essential for Shear-mediated Response	150
5.3.4. CRAC Channels Contribute to Extracellular Calcium Entry	153
5.3.5. Rates of the Calcium Dynamics.....	154
5.4. Discussion	155
6 CONCLUSIONS AND FUTURE WORK	167
6.1. Conclusions	168
6.2. Recommendations and Future Work.....	171
BIBLIOGRAPHY	177
APPENDIX A	198

DEDICATION

This thesis is dedicated to

Samira,

my best friend,

my supporting partner,

and the love of my life.

ACKNOWLEDGEMENTS

I am grateful to my supervisor, Prof. Jimmy Moore, for supporting me during the course of my PhD and helping me to develop my academic character. He has provided a stimulating environment in the lab, and has encouraged and supported me to pursue my research interests. All the experiences from collaborative projects and attending conferences have only been possible because of the opportunities he offered me and for that I am indebted to him.

I thank Prof. David Zawieja for always providing his physiological insight in the lymphatic-related projects that attracted my interest, Dr. Walter Cromer for helping me with lymphatic endothelial cell culture during my visit to Temple, Texas, Dr. Shenyuan Zhang for teaching me how to ratiometrically measure calcium dynamics and offered his microscope during my visit to Temple, Prof. Michael Carroll and Dr. Matthew Woodruff for having many fruitful discussions on how the lymph node is organized and advising me on the immunological relevance of the findings of my computational model.

I would like to express my sincerest gratitude to Prof. Mike Davis from University of Missouri. He has been my role model in research since my first collaborative visit to his lab in the Summer of 2014. His insight, diligence, organization and compassion, has inspired me in my research and personal life. I would like to specially thank Dr. Joshua Scallan for taking the challenge of cannulating mouse popliteal LN and making the Summer visits to Columbia, Missouri a fun and productive experience for my wife and me. Additionally, I wish to thank Dr. Joseph Sherwood from Dr. Overby's group for helping me in building the iPerfusion system that he had designed and also for many discussions about the proper use of statistics in the context of hydraulic resistance, Dr. Bindi Brook and Dr.

Rob Nibbs for providing critical comments to help guide the development of the chemokine model in lymph node.

Although many projects reached the end in time for the thesis submission, there are always the projects that remain to be completed in the transition and by the help of the collaborators and the rest of the lab members. I would like to thank Dr. Gowsihan Poologasundarampillai for having a persistent interest in micro-computed tomography scanning of LN microvasculature in Diamond synchrotron, Dr. Delfim Duarte for enthusiastically providing the samples for LN microvasculature corrosion casts and for always being available for the long days of sequential vessel casting, Dr. Alexandra Porter and especially Dr. Angela Goode for imaging the conduit structure of the lymph node using FIB-SEM and spending many late nights in the expedition for a properly oriented collagen fibres, Dr. Christina Fotopoulou for providing the clinical samples for mechanical characterization of lymphatic vessels, Prof. David Jackson and Dr. Kayla Holder for helping with shear-mediated LYVE-1 expression regulation in lymphatic endothelium.

Finally, I would like to think that my life has only been complete from the day I saw my beautiful wife, Samira Jamalian, in college. Since then, we have always been working in the same labs during the undergraduate project in Tehran, masters studies in Texas, and now PhD in London. It has been an exciting and eventful journey. I cannot thank her enough for her endless support during the days and nights that I felt breaking down. We have been comforting each other during the hard times and celebrating together during the joyous moments of the PhD. Samira is my best friend, labmate, and life partner who solely brings meaning to my life. It is impossible to thank her enough. I would also like to thank my in-laws, Nooshin,

Mammad and Nima for being supportive of us taking part in this long journey around the world.

I would like to thank my mom (Robabeh), brothers (Sasan and Abbas) and sister (Raheleh) for being there for me when growing up with dreams. Many friends and labmates made my time in the PhD more enjoyable. I would like to thank my former and current labmates, Dr. Elaheh Rahbar, Dr. William Richardson, Dr. John Wilson, Dr. Danika Hayman, Christine Otieno, Sarah Johnson, Arsham Gahramani, Karthik Ravichandran, Dimitrios Athanasiou, Candice Hureaux-Perron, Dana Tahboub, Elijah Choi, Emma Cooke, Dr. Lowell Edgar, Ahmed Ismail, Willy Bonneuil, Sam Banisadr, and my life-long friends, Hamed Zandieh, Khashayar Asadi, Amir Teymourpour, Hamoon jafarian, Amirhossein Taghavi, and our close friends here in London, Maryam Davari and Mohammadreza Jozi. In particular, I would like to thank Dr. John Wilson, our “long-time labmate”, who moved with us from Texas to London where we spent more than three years to explore our interests in science with non-stopping discussions about what the future brings us. That future is now. This thesis closes this chapter of our life and opens new and exciting opportunities.

این قافله عمر عجب میگذرد
دریاب دمی که با طرب میگذرد
ساقی غم فردای حریفان چه خوری
پیش آر پیاله را که شب میگذرد

The caravan of life shall always pass
Beware that is fresh as sweet young grass
Let's not worry about what tomorrow will amass
Fill my cup again, this night will pass, alas.

Omar Khayyám (1048 - 1131)

ORIGINALITY AND CONTRIBUTION STATEMENT

The work included in this submission is mainly performed by Mohammad Jafarnejad. Each chapter presented here is a result of collaborative work of many researchers and their contributions are acknowledged here:

Chapter 1: This chapter is in part taken from my two first author publications produced in Prof. Jimmy Moore lab.

Chapter 2: Dr. Matthew Woodruff performed mouse popliteal LN *in vivo* staining, dissection, optical clearance and confocal image acquisition. The idealized geometry was designed by Mohammad Jafarnejad after extensive discussions with Dr. Matthew Woodruff and Prof. Michael Carroll. Image processing, computational model development, case design and parameter sensitivity analysis were performed by Mohammad Jafarnejad.

Chapter 3: Dr. Joshua Scallan prepared micropipettes and performed mouse popliteal LN isolation and cannulation in Prof. Michael Davis's laboratory in University of Missouri. The LN resistance apparatus was built by Mohammad Jafarnejad with the help of Dr. Joseph Sherwood. This system was originally developed by Dr. Joseph Sherwood in Dr. Darryl Overby's laboratory at Imperial College to measure mouse eye facility. The experimental resistance measurement, and data analysis were performed by Mohammad Jafarnejad. Dr. Joseph Sherwood advised on statistical analysis of experimental data. Development of the new geometries, readjustment of the computational model and parameter sensitivity analysis were done by Mohammad Jafarnejad.

Chapter 4: The mass transport model development, simulation setup, parameter sensitivity analysis, and data analysis were done by Mohammad Jafarnejad.

Chapter 5: Dr. Walter Cromer helped with HDLEC culture. Chamber fabrication, part of cell culture, flow experiments, ratiometric microscopy and data analysis were done by Mohammad Jafarnejad.

I declare that the works presented in this thesis are my own work and performed in Prof. Jimmy Moore's Laboratory at Imperial College London. I certify that this thesis complies with copyright laws with appropriate reference to the third party published work. The contributions of the collaborators on each chapter have been acknowledged above. The granted permissions for the reuse of the already published materials are included in the Appendix A. The American Physiological Society granted permission to reproduce the figures, text and tables from my published work in American Journal of Physiology - Heart and Circulatory Physiology. Mary Ann Liebert, Inc. granted permission for the reuse of text and figures of my own first author paper published in Lymphatic Research and Biology.

COPYRIGHT DECLARATION

The copyright of this thesis rests with the author and is made available under a Creative Commons Attribution Non-Commercial No Derivatives licence. Researchers are free to copy, distribute or transmit the thesis on the condition that they attribute it, that they do not use it for commercial purposes and that they do not alter, transform or build upon it. For any reuse or redistribution, researchers must make clear to others the licence terms of this work.

ASSOCIATED PUBLICATIONS

Journal Publications:

- **Jafarnejad M**, Woodruff MC, Zawieja DC, Carroll MC, Moore JE, Jr. Modeling Lymph Flow and Fluid Exchange with Blood Vessels in Lymph Nodes. *Lymphatic Research and Biology*. December 2015, 13(4): 234-247.
- **Jafarnejad M**, Cromer WE, Kaunas RR, Zhang SL, Zawieja DC, and Moore JE, Jr. Measurement of shear stress-mediated intracellular calcium dynamics in human dermal lymphatic endothelial cells. *American journal of physiology Heart and circulatory physiology* 308: H697-h706, 2015.

Conference Presentations:

- **Jafarnejad M**, Brook BS, Nibbs R, Moore JE Jr. Computational Model of CCL19 and CCL21 Transport in the Lymph Node. *Chemotactic Cytokine Gordon Research Conference and Seminar*, Girona, Spain, May 28 – June 3, 2016. (Podium Presentation)
- **Jafarnejad M**, Behringer EJ, Scallan JP, Davis MJ, Segal SS, Moore JE Jr. Mathematical Model of Calcium and Electrical Dynamics in Lymphatic Endothelium. *Experimental Biology*, San Diego, CA, April 2016 (Poster Presentation)
- **Jafarnejad M**, Scallan JP, Jamalian S, Sherwood JM, Overby DR, Zawieja DC, Davis MJ, Moore JE Jr. Dynamic Changes of Lymph Node Substructures Control Hydraulic Resistance of the Lymph Node during Inflammation. *Lymphatic Gordon Research Conference and Seminar*, Ventura, California, March 19–25, 2016. (Poster Presentation)
- **Jafarnejad M**, Scallan JP, Sherwood JM, Overby DR, Zawieja DC, Davis MJ, Moore JE Jr. Local Inflammation Increases Hydraulic Resistance of Lymph Nodes. *2015 BSI Immunology Summer School*, York, UK, July 2015. (**Winner of Best Poster Award supported by Nature Immunology**)
- **Jafarnejad M**, Scallan JP, Sherwood JM, Overby DR, Zawieja DC, Davis MJ, Moore JE Jr. Modulation of Lymph Node Resistance during Inflammation: Experimental Measurement and Computational Modeling. *2015 Summer Biomechanics, Bioengineering and Biotransport Conference (SB³C)*, Snowbird,

UT, USA, June 2015. (Podium Presentation, **PhD Student Paper Competition Finalist**)

- Jamalian S, **Jafarnejad M**, Bertram CD, Zawieja DC, Davis MJ, Moore JE Jr. Suction Effect Produced by Active Contraction of Collecting Lymphatic Vessels Facilitates Lymphatic Filling. *2015 Summer Biomechanics, Bioengineering and Biotransport Conference (SB³C)*, Snowbird, UT, USA, June 2015. (Podium Presentation by Jamalian S, **Awarded 2nd place in PhD Student Paper Competition**)
- **Jafarnejad M**, Woodruff MC, Zawieja DC, Carroll MC, Moore JE Jr. The Exchange of Fluid Between Lymph and Blood in Lymph Nodes. *MEC Annual Meeting and Bioengineering14*, London, UK, September 7–8, 2014. (Podium Presentation)
- **Jafarnejad M**, Cromer WE, Kaunas RR, Zhang SL, Zawieja DC, and Moore JE Jr. Measurement of Shear Stress-Mediated Intracellular Calcium Dynamics in Lymphatic Endothelial Cells. *7th World Congress of Biomechanics*, Boston, MA, July 6–11, 2014. (Podium Presentation)
- **Jafarnejad M**, Woodruff MC, Zawieja DC, Carroll MC, Moore JE Jr. Computational Modeling of Lymph Flow in Lymph Nodes. *7th World Congress of Biomechanics*, Boston, MA, July 6–11, 2014. (Podium Presentation)
- **Jafarnejad M**, Cromer WE, Kaunas RR, Zhang SL, Zawieja DC, and Moore JE Jr. Shear Stress-Mediated Intracellular Calcium Measurement in Lymphatic Endothelial Cells. *Lymphatic Gordon Research Conference and Seminar*, Lucca, Italy, March 8–14, 2014. (Poster Presentation)
- **Jafarnejad M**, Cromer WE, Kaunas RR, Zhang SL, Zawieja DC, Moore JE Jr. Calcium Regulation in Lymphatic Endothelial Cells under Flow. *2013 ASME Summer Bioengineering Conference (SBC)*, Sunriver, OR, June 26-29, 2013, SBC2013-14828, pp. V01AT05A019. (Poster Presentation)

LIST OF ABBREVIATIONS

LN	lymph node
APC	antigen-presenting cell
DC	dendritic cell
CCL	CC chemokine ligand
LEC	lymphatic endothelial cell
BEC	blood endothelial cell
ApoE	Apolipoprotein E
WT	wild type
FRC	fibroblastic reticular cell
HIV	human immunodeficiency virus
TGF β	transforming growth factor beta 1
FDC	fibroblastic dendritic cells
SCS	subcapsular sinus
HEV	high-endothelial venule
Af	afferent vessel
BF	B cell follicle
TC	T cell cortex
M	medulla
Ef	efferent vessel
GPCR	G protein coupled receptor
CCR	CC chemokine receptor
ACKR	atypical chemokine receptor
CXCL	CXC chemokine ligand
HS	heparan sulphate

GAG	glycosaminoglycan
BV	blood vessel
CFD	computational fluid dynamics
LYVE-1	lymphatic vessel endothelial hyaluronan receptor-1
PLVAP	plasmalemma vesicle-associated protein
VEGF	vascular endothelial growth factor
TLR	Toll-like receptor
LPS	lipopolysaccharide
Poly I:C	polyinosinic:polycytidylic acid
IACUC	Institutional Animal Care and Use Committee
STD	standard deviation
SEM	standard error of mean
S1PR	sphingosine-1-phosphate receptor
ECM	extracellular matrix
PDE	partial differential equations
M ϕ	macrophage
ImmGen	Immunological Genome Project
PRCC	Partial rank correlation coefficient
KO	knock out
T _{FH}	follicular helper T cell
CXCR	CXC chemokine receptor
ABM	agent-based model
PDE	partial differential equations
eNOS	endothelial nitric oxide synthase
NO	nitric oxide

MLCK	myosin light chain kinase
RTK	receptor tyrosine kinase
PLC	phospholipase C
PIP2	phosphatidylinositol bisphosphate
IP ₃	inositol (1,4,5)-triphosphate
PLC	phospholipase C
IP ₃ R	inositol (1,4,5)-triphosphate receptor
HDLEC	human dermal lymphatic endothelial cell
PDMS	polydimethylsiloxane
DIC	differential interference contrast
ROI	region of interest
ER	endoplasmic reticulum
PSS	physiological saline solution
PLC	phospholipase C
SERCA	sarco/endoplasmic reticulum calcium ATPase
CRAC	calcium release-activated calcium channel
Tg	thapsigargin
BAEC	bovine aortic endothelial cell
MV2	endothelial cell growth medium MV2
DPBS	Dulbecco's phosphate-buffered saline
HBSS	Hanks' balance salt solution
FRET	fluorescence resonance energy transfer
FBS	fetal bovine serum
PMCA	plasma membrane calcium ATPase
μCT	micro computed tomography
PTA	phosphotungstic acid

LIST OF FIGURES

Figure	Page
1.1.	Schematic of lymphatic vessels from interstitium to LN.	34
1.2.	Schematic of LN structure with lymph flow paths.	38
2.1.	LN imaging and blood vessel reconstruction.	52
2.2.	Idealized geometry and the flow paths in the LN.	53
2.3.	Peripheral velocity contours and velocity profiles along the SCS.	60
2.4.	Pressure contours and lymph velocities.	61
2.5.	Shear stress contours in SCS and differences between shears on the SCS ceiling and floor.	62
2.6.	Parameter sensitivity analysis for surface area density and hydraulic conductivity of the blood vessels.	63
2.7.	Parameter sensitivity analysis for hydraulic conductivity of medulla.	65
2.8.	Parameter sensitivity analysis for average blood vessel pressure.	66
2.9.	Parameter sensitivity analysis for efferent pressure.	67
2.10.	Comparison to experimental data from Adair and Guyton.	70
3.1.	Mouse LN isolation and cannulation, and adjuvant treatment.	85
3.2.	Measurement setup and sample pressure and flow traces for resistance calculation.	87
3.3.	LN resistance changes with inflammation at 24 hr and 72 hr.	90
3.4.	Computational model prediction of possible mechanism of resistance increase and resulting flow redistribution.	93
3.5.	Scaling of LN resistance with animal body mass.	96

4.1.	Schematic of the LN with details of CCL19 and CCL21 interactions.	108
4.2.	Reaction equations for CCR7 and ACKR4 dynamics.	111
4.3.	LN geometry and distribution of CCL19 and CCL21 productions, as well as CCR7 and matrix binding site densities.	116
4.4.	CCL19 and CCL21 gradients in the interfollicular regions of the LN.	119
4.5.	Regional variations in the state of CCR7 receptors.	120
4.6.	Parameter sensitivity analysis.	123
4.7.	LN ACKR4 versus afferent vessel ACKR4 states.	125
4.8.	LN ACKR4 or afferent flow effect.	127
4.9.	Chemokine concentration difference across cells in interfollicular region.	128
5.1.	$[Ca^{2+}]_i$ increased with step changes in shear stress.	141
5.2.	$[Ca^{2+}]_i$ dynamics under different levels of shear stress.	147
5.3.	Effect of extracellular calcium concentration on $[Ca^{2+}]_i$ dynamics.	149
5.4.	Effect of Tg on shear-mediated calcium changes.	151
5.5.	Effect of a CRAC channel blocker S66 on $[Ca^{2+}]_i$ dynamics to shear. ...	152
5.6.	Curve-fit to the upstroke and downstroke of the calcium spike.	153
5.7.	Schematic of shear-mediated calcium dynamics in HDLEC.	156
A.1.	Permission for reprint of Chapter 2.	198
A.2.	Permission for reprint of Chapter 5.	199

LIST OF TABLES

Table	Page
3.1. Comparison of measured LN resistance across species.	83
4.1. Total cell numbers (N_k) and the percentage of cell types ($P_{k,j}$) present in different regions of the LN.	114
4.2. Normalized RNA expression of proteins by different cell types of LN from ImmGen database.	115
4.3. Input parameter range for latin hypercube sampling.	117
4.4. Results of parameter sensitivity analysis are summarized for key model outputs (for CCL19 and CCL21) and significantly correlated input parameters.	124
5.1. Shear stress level, extracellular calcium concentration and curve-fit parameters for the experiments.	154
5.2. Summary of shear-mediated calcium dynamics data available in the literature.	157

CHAPTER 1

INTRODUCTION AND BACKGROUND

1.1. Introduction

The lymphatic system has many recognized important roles in normal physiology and in a variety of disease conditions. In addition to returning fluid from interstitial tissue spaces to the blood circulation, it serves as an important transport route for immune cells. Lymph nodes (LN) are important outposts for cellular interactions essential for immune response, inflammation and fluid balance. Transport of exogenous antigen and pathogen as well as self-antigen via lymph to LN is shown to be essential for adaptive immune response and induction of immunological tolerance by regulatory T cells [1]. Furthermore, tumour-draining LNs exhibit diminished anti-tumour immunity [2], and are increasingly being targeted for delivery of therapeutic drug to enhance tumour-specific immune response [3-5]. Despite the importance in establishing the defence against deadly pathogens and cancer, little is actually known about fluid and molecule transport mechanisms in the LNs.

Lymph carrying peptides, proteins and immune cells enters the initial lymphatics and is transported by active contraction of collecting lymphatic vessels to downstream LN(s). In the case of peripheral infection, lymph flow is required for the delivery of pathogenic material to the draining lymph node where it can stimulate immune responses. In the B cell follicle, lymph-transported antigen can be scavenged from the lymph by subcapsular sinus macrophages and handed off to waiting B lymphocytes for initiation of humoral immune response [6-8]. Additionally, cytokines and chemokines released at the site of infection can be carried via the lymph to the draining lymph node, and have been shown to contribute to the quality and quantity of immune response [9, 10]. Furthermore, LNs are one of the points in the body where lymph that is transported from draining tissue can enter the blood vasculature, hence contributing to fluid balance role of lymphatic system. Despite the

importance of flow-mediated transport of antigen and other signalling molecules to specific compartments of the LN for proper function of immune system, flow distribution and exchange with blood vessels has received little attention.

The LN, being a passive and non-contractile component of the lymphatic system, imposes a hydraulic resistance against flow propelled by contracting collecting lymphatic vessels. Hence the organization of this porous structure not only is important for necessary cellular interactions, but also determines the afterload for collecting vessels. Remarkably, pathogen-driven inflammation results in cellular reorganization and (in the longer time points) swelling of the draining LN [11]. This change is mainly due to enhanced lymphocyte recruitment compared to egress as well as proliferation of both hematopoietic and stromal cell populations [12, 13]. However, it is unclear if it affects the flow distribution in the LN, and if yes, which compartment regulates this flow redistribution.

Peripheral infectious challenge can also result in cellular immune response via T lymphocyte activation in LN. Activated antigen-presenting cells (APC), most importantly dendritic cells (DCs), from the periphery capture, process and transport antigen along a carefully groomed chemokine gradient to the lymphatics (initials and collecting lymphatic vessels) [14-17]. When in the collecting lymphatic vessels, DC is carried by the flow to the draining LN where they again utilize the gradients of CC chemokine ligands 19 and 21 (CCL19 and CCL21) to enter the cortex through interfollicular region and facilitate T cell response [18, 19]. Lack of these gradients are shown to result in diminished immune response due to DCs being unable to enter the LN cortex from subcapsular sinus [19]. Although these interfollicular gradients are stable in presence of normal lymph flow, the role of flow in formation of the gradients remains to be elucidated.

In collecting lymphatic vessels, pumping appears to rely on specific mechanical cues (e.g., flow and pressure) to modulate pumping activity [20]. When a flow (shear) is induced in these vessels, the contraction frequency drops three-fold supporting the importance of mechanotransduction in regulation of pumping activity [20, 21]. Because LEC are subjected to both flow-induced shear stress and stretching as the vessel contracts and relaxes, these cells represent a logical target for investigating important mechanosensitive control mechanisms. Additionally, lymphatic endothelial cells (LECs) lining LN sinuses are subject to shear stress. Although the importance of mechanical shear stress has been investigated extensively in blood endothelial cells (BECs) [22-29], very few studies have attempted to unveil the effect of mechanical forces on LECs both *ex vivo* and *in vitro* [30, 31].

Despite the importance of lymph flow in many aspects of LN function (i.e. fluid balance, antigen transport to specific compartments, chemokine gradient formation, and shear-induced LEC signalling), little is known about flow distribution and its Immunomodulatory role in LN. Therefore, studying fluid and mass transport in LN is critical for comprehensive understanding of the immune response. The two main goals of this work are: 1) to understand how lymph is distributed and exchanged with blood vessels in homeostasis and during inflammation, and 2) to investigate the role of flow in chemokine transport, gradient formation and LEC signalling. To achieve these objectives, we formulated four specific aims each of which is addressed in a separate chapter.

1.2. Specific Aims

Specific Aim 1: Construct the first computational model of lymph flow through

LN. A computational fluid dynamic model of LN will be built and the distribution of flow through different paths will be quantified. Parameter sensitivity will be used to characterise the model and to identify key parameters that influence the flow patterns. We will then determine which parameters of the model have greater effect on the outputs and will propose experiments to measure these important parameters.

Specific Aim 2: Measure hydraulic resistance of healthy and inflamed LNs.

Inflammation results in a gradual reorganization of the LN structure and subsequent increase in the size of the LN after a few days. So, in addition to the healthy control LNs, we will investigate the dynamic changes in LN resistance after 24 hr and 72 hr of inflammation. We will then utilize the model developed in Aim 1 to predict the microstructural or geometrical changes that can result in the measured change in resistance. Additionally, we will examine how the change in resistance affect flow patterns in LN.

Specific Aim 3: Develop a model of chemokine transport and gradient

formation. We will integrate our knowledge of lymph transport (from Aim 1) with associated chemokine ligand-receptor interactions to build a comprehensive model of CCL19 and CCL21 transport and gradient formation in LN. Moreover, parameter sensitivity analysis will be performed to find the important parameters in determining the sign and magnitude of the gradient as well as the total chemokine mass. The

output parameters are chosen based on the ability to compare them with available experimental data. We will test the accepted hypothesis that interfollicular gradient of CCL21 is maintained by chemokine scavenging by LECs on the ceiling of the subcapsular sinus.

Specific Aim 4: Measure intracellular calcium dynamics of LECs under shear stress. We will investigate the dependence of calcium response to the magnitude of shear stress in the range relevant to lymphatic system. Additionally, we aim to find the source of the response by manipulating the extracellular calcium concentration or pharmacological blockade of channels and pump *in vitro*.

1.3. Background

1.3.1. Pathologies Associated with the Lymphatic System

Lymphatic system plays an important role in fluid and protein balance, lipid absorption and transport in intestine, and immune system function. The nature of the transport through this system along with dysfunction of its components is implicated in a plethora of diseases. Lymphoedema, the accumulation of lymph and proteins in the interstitial spaces that leads to swelling, is a debilitating disease directly associated with lymphatic system. There are two types of lymphoedema: 1) primary lymphoedema that is a class of genetic diseases that disrupt the lymphatic system development leading to oedema formation [32], and 2) secondary lymphoedema that is developed as a result of injury to lymphatic system [32, 33]. In the UK, the prevalence of all types of lymphoedema is shown to be 1.53-3.99:1000 and increased

by age (28.57:1000 for >85 year old individuals) [34]. Fluid stasis caused by lymphoedema results in accumulation of inflammatory signals and lowered macrophage infiltration that results in fibrosis and severe tissue remodelling [35, 36]. Impaired lymph transport results in compromised immune response and wound healing, which leads to higher prevalence of secondary bacterial, viral or fungal infections [37, 38].

In addition to lymphoedema, lymphatic system is linked to disease conditions such as obesity, atherosclerosis, inflammatory bowel disease and tumour metastasis. Models of obesity and metabolic syndrome show reduced lymphatic flow by about 50% [39, 40]. Additionally, LNs of obese animals have shown to be smaller with disrupted B cell follicles that may increase their susceptibility to infection [41]. The emergent role of lymphatics in reverse cholesterol transport has opened a new therapeutic target for the treatment of atherosclerosis [42]. Apolipoprotein E(ApoE)-deficient mice that develop hypercholesterolemia exhibit leakier lymphatic vessels as well as impaired lymph flow and DC transport compared to wild type (WT) mice, which is suggested to play a role in atherosclerotic plaque development [43-45]. In Crohn's and inflammatory bowel disease patients, intestinal oedema and dilation of lacteals (initial lymphatics in villi) are linked to impaired collecting lymphatic pumping [46-48]. Finally, lymphatic system, being the main route for macromolecule and cell transport from the tissue, serves as the primary route for tumour metastasis. Interstitial flow is shown to polarize the autologous transcellular CCL21 gradients around cancer cells to encourage migration toward initial lymphatics and metastasis to LNs [49]. In most lymphatic related diseases, impaired lymph flow and chronic inflammation results in abolished adaptive immune response or tissue specific tolerance that is orchestrated in the draining LN.

In addition to the chronic diseases discussed so far, there are several infectious pathogens that directly target LN. Many viruses (e.g. Ebola, Lassa and Marburg) disrupt cellular architecture of the LN by interfering with the network of fibroblastic reticular cells (FRCs, a key LN stromal population), which leads to destruction of the conduit system and elimination of distinct zones of B cell follicles and T cells cortex [50-52]. Moreover, experiments on human immunodeficiency virus (HIV)-1 infected rhesus macaques revealed regulatory T cell upregulation of TGF β 1 that induces collagen synthesis by FRCs [53]. LN fibrosis results in the loss of contact between FRCs and T cells, contributing to T cell apoptosis observed in HIV-infected patients [54, 55]. Better understanding of the lymphatic system and lymph flow in LN helps us to develop better therapeutics to treat these diseases.

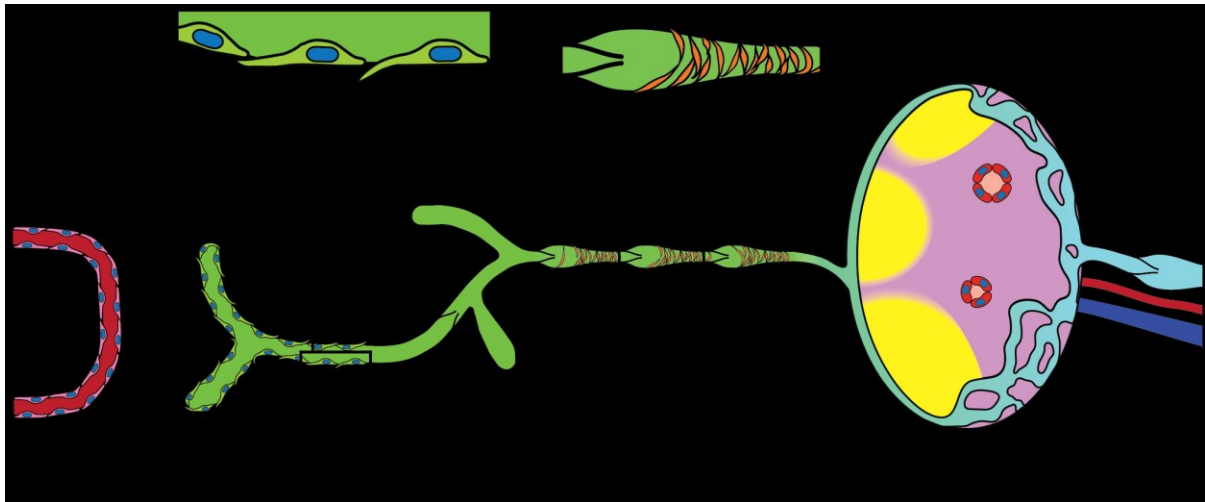


Figure 1.1. Schematic of lymphatic vessels from interstitium to LN. Fluid and proteins filters through capillaries and enters the interstitial space containing collagen and glycosaminoglycans. Mixture of fluid and proteins that enters the initial lymphatics through primary valves is called lymph. From initials, it enters the precollectors (having secondary valves but no muscles) to collecting lymphatic vessels that are covered by layer lymphatic muscle cells outside of the endothelium. The segment between two subsequent secondary bi-leaflet valves is called lymphangion. The propelled lymph then enters the LN where it can exchange fluid with blood vessels before leaving the LN through efferent vessel.

1.3.2. Anatomy of the Lymphatic System

The lymphatic system forms a tree-like network of vessels running parallel to blood circulatory system with the difference that they have a one-way flow from interstitium to subclavian vein near shoulder. Almost all the vascularized organs and tissues in the body include lymphatic drainage. Among the organs, brain was thought to not have lymphatic drainage; however, it was shown recently that there are lymphatic vessels in the dural layer of the brain that drains the injected dye in the cortex [56, 57]. From ~8000 litres of daily cardiac output, ~20 litres of fluid (with proteins) is filtered out through capillary wall, from which only part of it is reabsorbed by capillaries and venules [58]. The remaining 4-8 litres of the fluid is transported via lymphatic system back to the blood circulation [58]. The fluid enters the lymphatics through “initial lymphatic vessels”, which are the blunt-ended vessels made of loosely connected LECs (Figure 1.1). When interstitial fluid enters initial lymphatics it is called lymph. These initial lymphatics coalesce to form larger “collecting lymphatic vessels” (Figure 1.1). In addition to tighter endothelial junction, these vessels are covered with lymphatic muscle cells and contain intraluminal bi-leaflet valves to ensure unidirectional flow from interstitium to venous return. The collecting lymphatic vessels merge into larger pre-nodal collecting vessels before entering the lymph nodes. LNs serve as outposts of immune system that filters the lymph for the examination and surveillance of its content. LNs are vascularized tissues and based on the hydrostatic and oncotic pressure differences, lymph can exchange fluid with blood vessels. The remaining lymph exits the LN into post-nodal collecting lymphatic vessels that subsequently coalesce until they reach thoracic duct. This large vessel joins the subclavian vein to empty the lymph content back into the blood circulatory

system. In the next few sections, we explain in more detail the organization and role of each of these components of the lymphatic system in fluid and mass transport.

1.3.2.1. Initial Lymphatics

Initial lymphatic vessels are the most distal, blunt-ended vessels of lymphatic network that serve as ports of entry for interstitial fluid to enter the lymphatics. These vessels are also called “terminal lymphatics” or “lymphatic capillaries”. Initial lymphatics are made up of a single layer of LECs with disrupted basement membrane. The organization of these vessels change based on specific organs; for instance, they form an interconnected hexagonal meshwork in rat tail, while the initials in the intestine are single blunt-ended vessels in each villi [59]. The diameter of initial lymphatics also varies with tissue and species. In rat intestinal villi, the diameter of initial lymphatic is shown by intravital microscopy to be 15-30 μm [60, 61]. Initial lymphatics are measured to be larger in diameter in skin of rat (25-50 μm) and human (35-70 μm) [62-64].

LECs of initials form button-like junctions that result in overlapping leaflets on the bordering cell [65]. Alternating arrangement of PECAM-1 and VE-cadherin in the cell-cell junction makes these special leaflets that are proposed to serve as the valves for unidirectional fluid and protein movement from interstitium into the vessels [65] (Figure 1.1). Furthermore, initial LECs are shown to express aquaporin-1 water channels that could contribute to the transport of water for lymph formation [66]. Additionally, LECs of initials are shown to be attached to the surrounding extracellular matrix via anchoring filaments. This helps to keep the vessel open

during adverse transmural pressure while staying functional, which is essential for lymph formation [67, 68].

1.3.2.2. Pre-collectors and Collecting Lymphatic Vessels

Initial lymphatics conjoin to form larger collecting lymphatic vessels that have two main characteristics: 1) they are covered with a layer of lymphatic muscle cell on the outside of LEC monolayer, and 2) they include intraluminal bi-leaflet valves called secondary lymphatic valves (in contrast to the primary valves on the initial lymphatic walls) [59, 69]. In some tissues such as skin draining lymphatics, lymph first enters pre-collector that have the secondary valves but lack lymphatic muscle layer [59] (Figure 1.1). The muscle cells on collecting vessels are essential for controlling the vessel tone and active contraction for lymphatic pumping [70]. The space between two consecutive secondary valves is called lymphangion, which serves as a contractile unit to drive lymph flow. Unlike blood circulatory system that contains a central pump (heart), lymphatic system utilizes the active pumping of its individual components. There are two main mechanisms for flow propulsion in lymphatics: 1) Intrinsic pumping that is the spontaneous phasic contraction of lymphangions, and 2) extrinsic pumping which happens when collecting vessels are squeezed by surrounding tissue/organ such as skeletal muscles [70, 71]. In both mechanisms, secondary valves are essential to prevent backflow, especially because for humans the system needs to pump the fluid against gravity to the venous return in shoulder [59, 71].

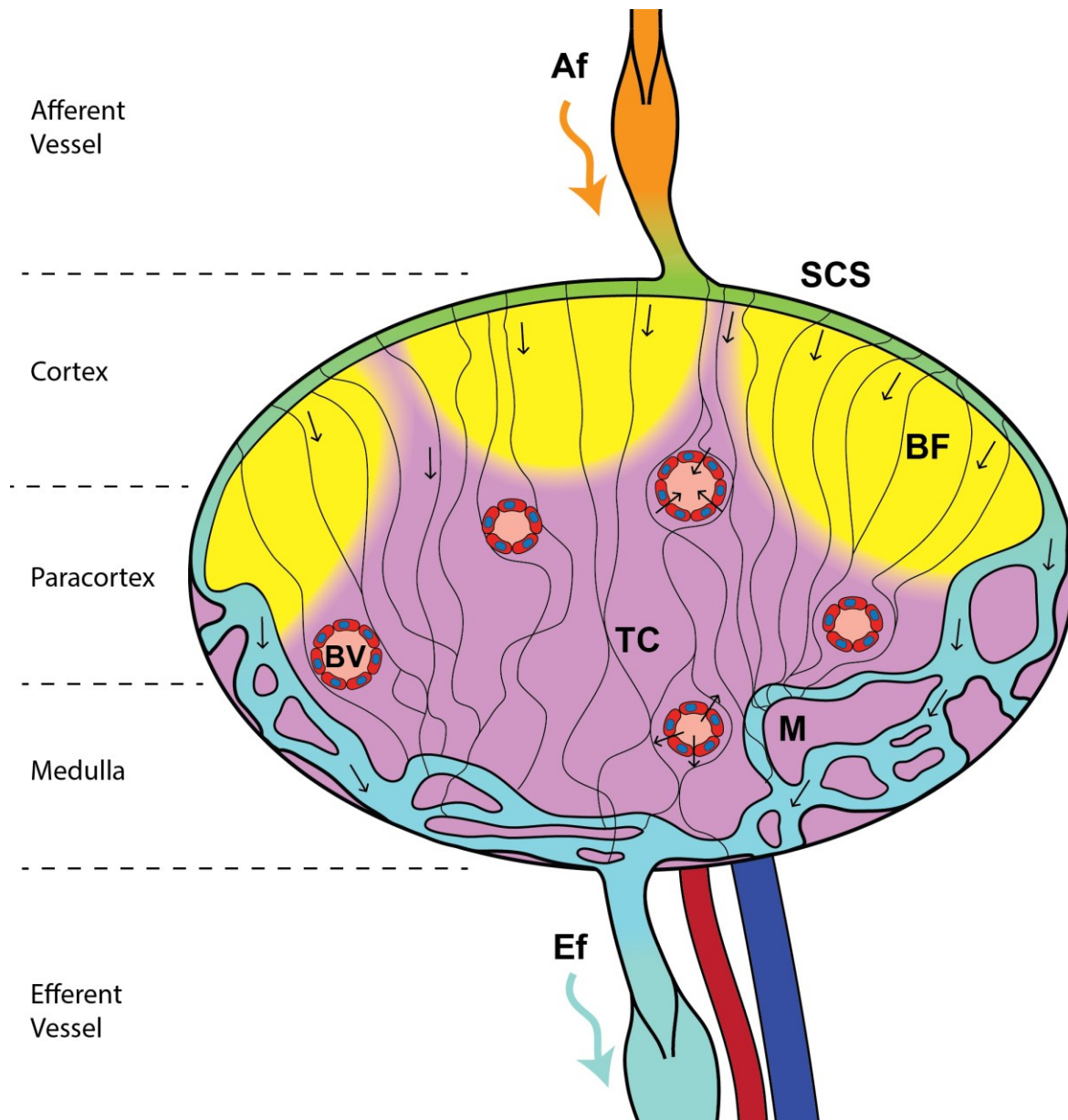


Figure 1.2. Schematic of LN structure with lymph flow paths. LN has several distinct geometrical regions, mainly afferent vessel (Af), subcapsular sinus (SCS), B cell follicles (BF), T cell cortex (TC), medulla (M), blood vessels (BV), and efferent vessel (Ef). The place that B cell follicles are located is called cortex, the central zone where T cells are is paracortex and the area near the efferent vessel that has the labyrinth-like sinuses is called medulla. Specific cell types are located in each of these regions. Fluid can enter the LN through afferent vessel and continue its journey either through subcapsular sinus to medullary sinuses, or percolate through the central regions of the node either between the cells or through the conduit system (network of thin curves) and exchange fluid with blood vessels.

1.3.2.3. Lymph Nodes

The lymph pumped by collecting lymphatics enters one or several LNs before returning to blood circulation. There are around 600 LNs in human body and most of them are located in the softer regions of the body (neck, armpit, abdominal cavity, groin, and behind the knee), and are often surrounded by fat tissue. LNs are focal points that lymphatic system and blood circulation intersect and closely interact. A LN comprises of several distinct cellular regions contained in a fibrous capsule where afferent and efferent collecting lymphatic vessels serve as the inlets and outlets for lymph transport. There are four main hematopoietic cell (i.e. B cell, T cell, DCs, and macrophages) and three key stromal cell (i.e. FRCs, LECs and BECs) populations in the LN many of which show vast heterogeneity with specific subsets. Primarily, LN is home to the two main lymphocyte populations, B cells and T cells, which are vital for adaptive immune response. B cells localize in the cortex and form many follicles of ~150 μm in diameter close to the afferent entry (Figure 1.2) [72, 73]. The formation of follicles is mediated by a specialized LN stromal cell subset called follicular dendritic cells (FDCs) that are located in the core of the follicle and attracts B cells upon entry via a chemotactic signalling mechanism. T cells predominantly localize in the LN paracortex and are retained by another chemotactic signalling axis mainly from FRCs [74].

There are sinuses in the LN that are lined with LEC and can be thought of as the extensions of afferent and efferent lymphatic vessels into the LN [13]. The sinus on the afferent side is called subcapsular sinus (SCS) that is a thin space of ~10-20 μm height with the ceiling LECs being on under the capsule, and the floor LECs covering the B cell follicles [12, 75, 76]. On the efferent side, the sinuses form an interconnected labyrinth-like structure called medullary sinuses or medulla that

wraps around the T cell cortex and reaches the SCS on the periphery of the LN [77]. The fluid in the SCS can also enter an interconnected network of extracellular matrix (containing aligned collagen fibrils and proteoglycans) called conduit system and be transported to cortex and paracortex [78, 79]. Additionally, LN is a vascularized organ and can have one or many arterioles supplying it depending on the species and location in the body [80]. The LN venules are specialized blood vessels that naïve lymphocytes use to enter the paracortex. Due to the high transmigration rate of naïve lymphocytes across these venules, their blood endothelial cells are bulged into the vessel inspiring the name of high-endothelial venule (HEV) [12].

1.3.3. Immune Response In LNs

In the case of a peripheral infectious challenge, pathogens and their products are swept up in the lymph and carried to the “draining LN”, making these sites ideal as centralized points of immune surveillance [81]. As lymphocyte activation is dependent on antigen exposure, lymph flow is required for the delivery of pathogenic material to the draining lymph node where it can stimulate immune responses. In the B cell follicle, lymph transported antigen can be scavenged from the lymph by subcapsular sinus macrophages and handed off to waiting B lymphocytes [6-8], or directly scavenged from the lymph via the dense conduit network [78]. In the case of T lymphocyte activation, activated DCs, from the periphery capture, process and transport antigen along a carefully groomed CCL19/21 gradient to the lymphatics [14-16]. Additionally we have shown that there is a population of antigen-presenting cells within the walls of the muscularized prenodal lymphatics that can also capture, process and transport antigen but do it very quickly [17]. When in the collecting

lymphatic vessels, DCs can detach from the lymphatic endothelial cells and join others suspended in the lymph to be carried by the flow to the draining LN where they facilitate T cell response [18, 19]. Additionally, cytokines and chemokines released at the site of infection can also be carried via the lymph to the draining lymph node, and have been shown to contribute to the quality and quantity of immune response [9, 10]. In all three of these systems - passive antigen drainage, active antigen transport via cells, and cytokine 'remote signalling' - the dynamics of lymph flow within the LN have significant impact on the ability of the immune system to appropriately and rapidly respond to peripheral challenge. In the absence of lymph flow, antigen, cytokine and chemokine transport would have been limited to effective diffusion length scales of a few hundred microns [82]. Moreover, DCs are bound with the crawling speed of $\sim 6.4 \mu\text{m}/\text{min}$ in the initial lymphatics, whereas when they are transported via lymph flow in the collecting vessels, they have velocities around $1200 \mu\text{m}/\text{min}$ (~ 200 -fold faster) [18]. Despite the essential role of lymph flow in modulation of adaptive immune response and immunological tolerance, the patterns of flow and molecule transport in the LN is barely studied to date.

1.3.4. LN Chemokines and Their Receptors

Leukocytes, being the first responders and immune surveillance agents of the immune system, need directional migration to be able to respond to injury and pathogens [83, 84]. Additionally, the close interaction of immune cells is necessary for antigen presentation and lymphocyte activation that results in adaptive immune response. A class of small cytokines (8-12 kDa) with structural similarities called

chemotactic cytokines (in short “chemokines”), bind to their G protein coupled receptor (GPCR) on leukocytes and induce directed migration [85, 86]. There are more than fifty chemokines and about twenty receptors that orchestrate a wide variety of complex leukocyte migration and interaction in the body [74]. Among the receptors, CC chemokine receptor 7(CCR7) and its exclusive ligands, CCL19 and CCL21, are of great importance in lymphatic system and adaptive immune response. Activated DCs utilize this chemokine axis to migrate out of interstitial space to the lymphatic vessels and are transported via lymphatics to the LNs [87]. The same axis is utilized by naïve B cells and T cells to transmigrate across HEVs and home in LN. In addition to the chemokine receptors that activate downstream cell migration pathways, there are a group of atypical chemokine receptors (ACKRs) that bind the ligand, internalize and scavenge it, but do not activate any cell migration signalling pathway [88]. Among ACKRs, ACKR4 binds both CCL19 and CCL21 scavenges them, which is shown to be crucial for dendritic cell migration from LN sinuses to cortex [19]. Additionally, CXC chemokine ligands 12 and 13 (CXCL12 and CXCL13) are other important for B cell follicle formation and germinal centre reaction [89]. Herein, we review the CCL19-CCL21-CCR7-ACKR4 axis and explain the recent advancements on the role of ACKR4 in chemokine gradient regulation.

1.3.4.1. Ligands

CCL19 (8.8 kDa) and CCL21 (12.2 kDa) are both CC-chemokines with two consecutive cysteine residues near the N-terminus that form disulphide bridges in the tertiary structure of the protein. Compared to CCL19, CCL21 have an extended

32-residue long C-terminus that can bind extracellular or transmembrane matrices such as heparan sulphates (HS) on glycosaminoglycans (GAG) [90]. Indeed, Hirose et al. [91] showed that a truncated version of CCL21 without the last 32 residues failed to bind to GAGs. CCL21 exhibits strong binding to GAGs (such as chondroitin sulphate, heparin and heparan sulphate) [90, 92, 93], and Collagen IV [94], whereas CCL19 does not bind to any measurable degree to the matrix [90, 92-94]. Furthermore, recent studies showed that CCL19 and CCL21 both promote directed migration in activated DCs while only bound CCL21 could induce β 2 integrin-mediated adhesion [95]. Although CCL19 and CCL21 both bind to CCR7 and ACKR4 with similar binding rates, they have different molecular structures and distinctive expression patterns, which mean they are not functionally redundant in the body [74]. Medullary thymic epithelial cells and FRCs in LN express both CCL19 and CCL21, but LEC and blood endothelium mainly express CCL21 and not CCL19. A major functional difference between CCL19 and CCL21 is the degree by which they internalize CCR7 after ligation. CCL19 binding phosphorylates the receptor and recruits β -arrestin that leads to receptor internalization and desensitization, thereby resulting in CCL19 degradation and receptor resurfacing. In contrast, CCL21 binding to CCR7 does not lead to receptor desensitization and internalization.

1.3.4.2. Receptors

CCR7. CCR7 is expressed on naïve B cells and T cells [85, 96], regulatory T cells [97], central memory T cells [85], and semi-mature and mature DCs [98] in the LN [99, 100]. Furthermore, CCR7⁺ cancer cells have shown enhanced metastasis to lymphatic vessels through autologous chemotaxis [49]. CCR7, similar to all

chemokine receptors, is a GPCR with seven transmembrane alpha helices. All the functional chemokine receptors have an intracellular sequence motif that couples to G proteins and activate the downstream signalling that includes phosphatidylinositol-3-kinase (PI3K), tyrosine kinases, and phospholipases A and D, which then results in cell adhesion, calcium mobilization, and assembly of protein machinery needed for cell migration [99]. CCR7 is essential for homing of T cell and B cells to LN and thymus through the blood vessels of these organs. Additionally, CCR7 is shown to be the key receptor that is upregulated on the activated DCs in the interstitial spaces and mediates the migration of DCs towards the lymphatic vessels where they are transported to the LN [87]. In the LN, DCs utilize CCR7 to migrate in the interfollicular regions toward the paracortex.

ACKR4. There are four atypical chemokine receptors, all belonging to GPCR family, that fail to initiate the downstream signalling pathway [88]. ACKR4 binds to CCL19, CCL21 and CCL25 and scavenges them locally. ACKR4 is expressed by LECs under the capsule of the LN, 75% of skin keratinocytes and 15-20% of LECs in the skin. Dissociation constant (K_D) for ACKR4 binding to CCL19 is 4.5 nM, i.e. very similar to that of CCR7 (~5 nM) [101]. ACKR4 is rapidly internalized upon CCL19 binding and could scavenge six to seven CCL19 molecules per hour per starting ACKR4 surface molecule [101]. In inflamed skin, ACKR4 is shown to be essential for CCL19 and CCL21 scavenging to facilitate APC egress to lymphatic vessels [102]. In ACKR4 KO mice, DCs injected in the afferent vessel exhibited reduced migration to the paracortex that was linked to the abolished CCL21 gradients in the interfollicular regions [19]. Overall, further investigation of the chemokine transport in

LN and interstitium is necessary to understand chemokine gradient formation in healthy and pathologic conditions.

1.3.5. Computational Modelling in the Lymphatic System

Mathematical and computational modelling has been widely used to improve our understanding of the physiology and immunology of biological tissues [103-106]. These methods can be utilized to identify key parameters of a system, suggest new hypotheses and estimate parameters that cannot be measured [104, 107]. The design of the model should take into account the important characteristics of the system being modelled as well as the nature of the questions to be answered [105]. Our research group have been interested in the physiology and function of the lymphatic system as a whole. Other members of the lab have modelled different sub-sections of the system address questions related to a specific location, time, and spatial scale in the LN. We have previously built a lumped parameter model of collecting vessel pumping to investigate overall pumping characteristic of these vessels in series [108] or in branching networks [109]. Other lab members have built a computational fluid dynamic model of the lymphatic valve to better understand the flow patterns around its leaflets [110, 111]. Here in this thesis we will address how fluid and proteins are transported in the LN as one of the components of the lymphatic system, and will explore how this fluid and mass transport can affect the immune response. A few models of LNs have been built before that we will review here. Bocharov et al. used reaction-diffusion models to simulate the distribution of interferon- α in the 3D geometry of the node, but lacked advective transport in the LN [112]. The closest work to that is presented in Chapter 2 is the work by Cooper et al. [113], which was published after acceptance our publication in Lymphatic Research

and Biology [114]. Cooper and colleagues modelled the LN vasculature based on 3D images acquired by light sheet microscopy of optically cleared LNs. However, their model did not include the important sinus structures of the LN (subcapsular sinus and medulla), which resulted in the flow to move directly from afferent vessel to efferent vessel in the porous material [113]. This completely disregards the experimental data that shows the presence of these sinuses [12, 75, 76, 115], and tracer studies that demonstrate higher flow of fluid in subcapsular sinuses in the periphery of the LN [78]. Additionally, their image-based data only took into consideration the larger blood vessels that were possible for segmentation using the conventional threshold techniques, and did not include the capillaries that provide a large portion of the surface area for fluid exchange [113]. Several other models of LNs have been developed using agent-based modelling, and cellular Potts model techniques, and have been able to simulate cellular motions, cell-cell interactions, and cell influx and efflux [116-118]. Except Cooper et al. study that was concurrent with our work, all the other techniques described so far are useful in studying molecular diffusion and cellular interactions, but they fail to address the questions about fluid transport in the LN and advective transport of molecules by lymph. A computational fluid dynamics model based on the experimental data can investigate the lymph flow in the mouse LNs, and further expand our knowledge of antigen and chemokine transport in the node.

CHAPTER 2

MODELLING LYMPH FLOW AND FLUID EXCHANGE WITH BLOOD VESSELS IN LYMPH NODES

2.1. Introduction

Structurally, the lymph node (LN) is comprised of several distinct lymphatic compartments, each of which provides different resistance to lymph flow. When lymph enters the node through afferent vessels, it arrives first in the subcapsular sinus (SCS) lumen [119, 120]. This sinusoidal space, often characterized by the presence of SCS macrophages, overlays the LN cortical regions (B cell follicles) in a ~10-20 μm sheet spanned by periodic collagen spacers which connect the outer LN capsule with the SCS floor [75]. As lymph flows through the SCS lumen, it can be laterally diverted into the conduit system – a network of fine reticular collagen fibrils, which penetrate the B cell follicle and reach deep into the paracortex. The conduit network has been shown to be important in the delivery of soluble antigen to B cell follicles resulting in deposition on the resident follicular dendritic cells [121]. Interestingly, this system has been shown to exhibit a molecular weight cut-off at roughly 70kD, with larger antigens being excluded [79], and therefore retained in the SCS. Lymph and soluble molecules not directed into the conduit system are presumably transported into the LN medulla via lymph paths that are not well described and characterized prior to collection and egress in the efferent lymphatics [120, 122, 123]. The medulla is comprised of a complex network of lymphatic vasculature densely packed by medullary macrophages as well as trafficking leukocytes [75]. While each of these structures has been individually evaluated in contribution to potential immune response, their individual impact on fluid flow, and thus chemokine and antigen distribution throughout the LN, has not been evaluated.

To characterize the structure of the LNs, Woodruff et al. developed whole organ imaging of cleared nodes as well as 3D reconstruction of serially sectioned nodes [77]. Although the whole organ imaging technique provides valuable insight

into the location and size of the each of the nodal compartments and cellular interactions, it provides no information on physical properties such as hydraulic conductivity and permeability that govern lymph and antigen transport in the node. Although most of the current immunology and drug discovery experiments are carried out on mice, no experimental data are available on the fluid exchange in the LNs of mice, presumably because of the scale of the mice nodes as well as the complexity of the numerous inlets and outlets for lymph and blood in the nodes. Others have taken the approach of analysing LNs in larger animals such as dog and sheep. Adair and Guyton cannulated afferent and efferent vessels of canine popliteal LN and left the blood vessels intact while measuring pressure in a downstream venule [124, 125]. By perfusing the node with a constant flow rate, they were able to show that about 10% of the afferent lymph is absorbed by blood vessels under physiologic pressures, whereas during imposed venous hypertension the direction of the lympho-venous fluid flow can reverse [124]. They also showed elevation in efferent lymph pressure will increase the amount of fluid transported to blood vessels [125]. Thus the balance of fluid flows and pressures across the nodal vasculature plays a critical role in determining the movement of lymph fluid through different parts of the node and thus overall immune function.

Despite the critical role of lymph as the carrier for molecules and cells to the LNs, little is known about its transport patterns and modification while passing through the node. This work aims to construct the first ever three-dimensional computational model of the lymph flow in the LNs and to use parameter sensitivity analysis techniques to determine the important parameters in the lymph transport and exchange in the node.

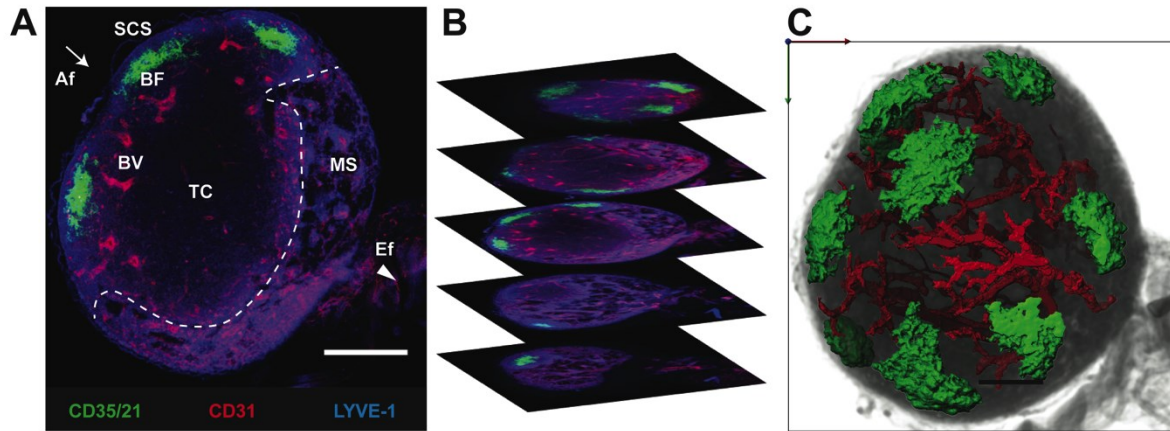


Figure 2.1. Lymph node imaging and blood vessel reconstruction. **A.** A cleared popliteal lymph node was stained for B cells (CD35/21, green), blood endothelial cells (CD31, red), and lymphatic endothelial cells (LYVE-1, blue) and was imaged using confocal microscopy. Lymph enters the node (arrow) through afferent lymphatic vessel(s) (Af). It then moves to subcapsular sinus (SCS), which can then go to either B cell follicles (BF) and T cell cortex (TC) through central path, or directly to medullary sinuses (MS) through peripheral path. Lymph, will leave the node (arrow head) through efferent vessel(s) (Ef) though some lymph fluid will be absorbed by blood vessels (BV). Scale bar is 200 μm . **B.** Z-stack confocal images were acquired for blood vessel geometry reconstruction. **C.** Blood vessels (CD31⁺ cells) of the node are segmented using a threshold/paint technique. The surface area and the total volume of the node are extracted from the images and are used to calculate surface area density of the blood vessels. The B cell follicles are segmented to demonstrate the relative location of the major blood vessels to them. Scale bar is 200 μm .

2.2. Methods

2.2.1. Geometry Model

An idealized geometry of the lymph node was constructed in Solidworks 2012 (SP4.0, Dassault Systèmes, France), which is qualitatively based on the images captured in this study as well as available images in the literature (Figure 2.1A-B). The node shape was based on an oblate ellipsoid of the size of a typical mouse popliteal node (large diameter of 1 mm and small diameter of 0.7 mm). The final geometry was comprised of a combination of fluidic and porous regions. The height

of the SCS was shown to range from 10-20 μm , and here it is assumed to be 10 μm [12, 19, 75, 76]. The geometry shown in Figure 2.2B is fed by only one afferent vessel at the centre (which more closely corresponds to the situation of a mouse popliteal node). The diameters of the afferent vessel and efferent vessel are 70 μm and 100 μm , respectively. The afferent vessel, efferent vessel and subcapsular sinus are modelled as fluidic regions (bounded spaces of only fluid), while the B cell follicles, T cell cortex and medulla are modelled as porous regions (Figure 2.2B). The seven B cell follicles are 180 μm in radius and are symmetrically distributed 400 μm apart. The maximum thickness of the medulla is assumed to be 150 μm . Flow through the subcapsular sinus, the space between the outer capsule of the node and the inner cellular regions, reportedly is not significantly restricted by the collagen spacers, justifying its approximation as a fluidic region [126].

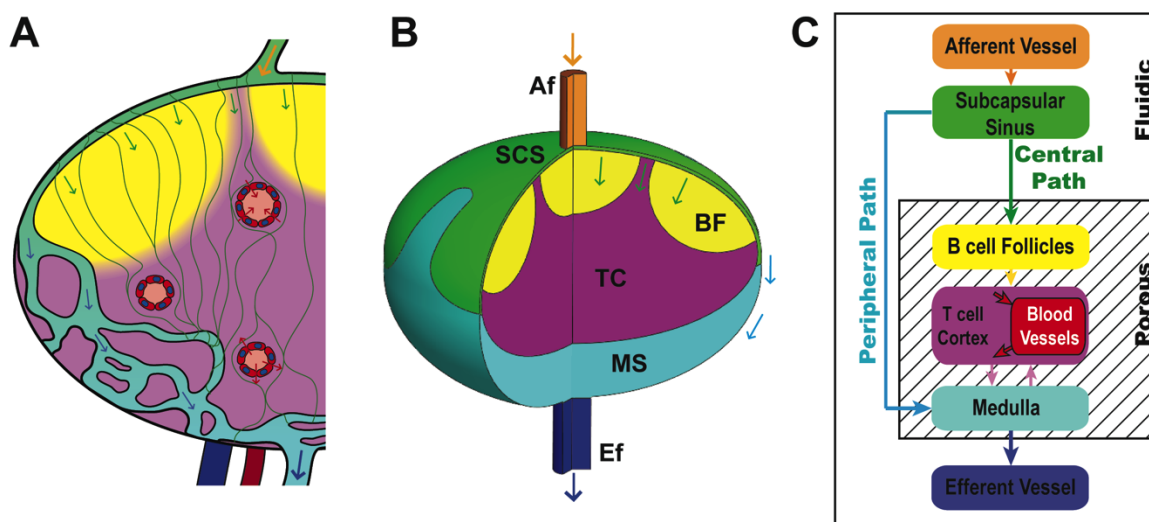


Figure 2.2. Idealized geometry and the flow paths in the lymph node. **A.** Schematic of LN shows how the lymph can pass through the node from the afferent to the efferent lymphatics as well as exchange fluid with the blood vessels in the LN. **B.** An idealized geometry made for modelling purposes. Although a single afferent vessel is pictured here, there are many LNs in mice and most LNs in larger animals that have several afferent vessels. **C.** A flowchart of the lymph movement through regions of the node shows the central path (flow from SCS to BF and TC) and peripheral path (flow from SCS to MS) for the lymph movement through the node.

2.2.2. Computational Fluid Dynamics

Star-CCM+ (CD-adapco, London), a commercially available finite volume based solver, was used to model fluid flow inside the LNs. The idealized geometry was imported to Star-CCM+ and meshed using polyhedral elements with prism layer in the wall or porous boundaries of the fluidic regions. Computational Fluid Dynamics (CFD) can be a highly accurate means of simulating a variety of flow situations, and works on the principle of solving algebraic representations of the governing fluid flow equations (conservation of mass and momentum) across the small elements that make up the overall geometry [127]. The lymph is modelled as an incompressible (constant density), Newtonian (constant viscosity), homogenous and single component fluid. The bulk properties of lymph such as density and dynamic viscosity are estimated from the literature, which includes the effect of protein concentration. Note that direct representation of proteins is not necessary because of the continuum assumption inherent to the model and the length scales of the flow phenomena of interest here (microns and upward). For the porous regions of B cell follicles, T cell cortex and medulla, the conservation of mass equation and Darcy's law with Brinkman's term in the form of

$$\frac{1}{K} \mathbf{u} = -\nabla p + \mu \nabla^2 \mathbf{u} \quad (2.1)$$

(where K is the hydraulic conductivity matrix, \mathbf{u} is the fluid velocity vector, p is pressure and μ is the dynamic viscosity of lymph) were solved. A heterogeneous mesh was constructed with prism layers near the walls in AF, Ef and SCS to ensure appropriate spatial resolution for accurate velocity gradient calculations. The prism layer was defined to have at least ten computational elements between SCS floor and ceiling. A grid independency study showed that the results with ~420,000

elements had 2.6% normalized root mean squared error for wall shear stress along the SCS, compared to the finer mesh with ~680,000 elements. Other parameters of the study had less than 0.5% error between the two mesh sizes. The mesh with ~420,000 elements was used for the remainder of the study.

To model the exchange of fluid between lymphatic system and blood vessels in the lymph node, we used a source/sink term in the conservation of mass equation

$$\nabla \cdot \mathbf{u} = q_{BV}(p(\mathbf{x})) \quad (2.2)$$

$$q_{BV}(\mathbf{x}) = LA \left[(p(\mathbf{x}) - P_{BV}) + \sigma (\pi_{BV} - \pi_{lymph}) \right] \quad (2.3)$$

where q_{BV} follows Starling's equation (Equation 2.3), L is the average hydraulic conductivity of the blood vessels in the node, A is the surface area density of the blood vessels available for exchange of fluid, P_{BV} is the average blood vessel pressure, σ is reflection coefficient of the blood vessels, π_{BV} is the average oncotic pressure of the blood vessels, and π_{lymph} is the average oncotic pressure of the lymphatic channels of the lymph node. In this model, we assumed that the majority of the blood vessels are located in the T cell cortex, and thus the sink term (Equation 2.2) is applied only in this region and homogenously distributed.

The flow of lymph through SCS results in a frictional wall shear stress on both the "ceiling" of the SCS (capsule of the node) as well as the "floor" (bordering the B cell follicles and T cell cortex). Following calculation of the velocity vector field, shear stress is calculated using

$$\mathbf{T} = \mu \left[\nabla \mathbf{u} + \nabla \mathbf{u}^T - \frac{2}{3} (\nabla \cdot \mathbf{u}) \mathbf{I} \right] \quad (2.4)$$

$$\boldsymbol{\tau} = \mathbf{T} \cdot \mathbf{n} - ((\mathbf{T} \cdot \mathbf{n}) \cdot \mathbf{n}) \mathbf{n} \quad (2.5)$$

where \mathbf{T} is the fluid stress tensor, the superscript T means transpose of the matrix, \mathbf{I} is the identity matrix, \mathbf{n} is face normal vector, and τ is wall shear stress. The model was solved with the boundary conditions of uniform afferent velocity and constant efferent pressure. The uniform velocity at the inlet of the afferent vessel was 0.58 mm/s, and was calculated to result in shear stress of 1 dyn/cm² in the afferent vessels at steady state. This is close to the average shear stress measured in rat mesenteric lymphatic vessels [30]. Reynolds number, the ratio of the inertial forces to viscous forces at the afferent vessels was 0.027 (Reynolds number < 1), which means that the flow regime was viscous flow and the length required for the flow to fully develop was less than a micron. Efferent pressure is assumed to be 3 mmHg for the baseline case, which is in the physiologic pressure range of lymphatic system [63, 128], although parameter sensitivity analysis was performed to investigate the effect of changes in efferent pressure.

2.2.3. Animals

In order to provide more quantitative information on blood vessel structure of mouse popliteal LNs, C57BL/6 mice were used in this study. Mice were housed and bred in standard conditions and used between 6 and 8 weeks of age. Experimental protocols were approved through Harvard University's Institutional Animal Care and Use Committee and conducted in accordance with the National Institutes of Health's Guide for the Care and Use of Laboratory Animals.

2.2.4. In vivo Labelling

In vivo labelling of the popliteal LN was achieved through pre-harvest injection of monoclonal antibodies targeting antibody targeting LN stromal populations. Anti-CD35/21 (Alexa 488), and anti-CD31 (Alexa 568) were injected i.v. 24, and 1 hr prior to LN harvest respectively. Anti-Lyve1 (Pac Blue) was injected subcutaneously in the footpad 4 h prior to harvest (Figure 2.1A).

2.2.5. LN Clearing and Whole Organ Imaging

LNs were dissected and fixed overnight in 4% paraformaldehyde at 4°C. The sample was then incubated in Scale-A2 buffer as previously described [129] for at least 3 weeks at room temperature. Following clearing, intact LNs were imaged by standard confocal microscopy (Figure 2.1B). Images were representative of at least 2 independent trials.

2.2.6. Blood Vessel Segmentation

Red channel of the acquired popliteal LN z-stack was imported to ScanIP, Simpleware Ltd., UK. After smoothing the data with a Gaussian filter, a combination of threshold and paint was used to carefully segment out all bigger vessels that could be recognized by the user (Figure 2.1C). It was not possible with the available technique to segment any smaller blood vessels and capillaries that were shrunk as a result of depressurization and fixation. The blood vessels were then reconstructed from the produced mask and the surface area of the blood vessels were calculated

to be 1.5 mm^2 . Because the capillaries and small vessels that can exchange fluid are not segmented in this image-processing algorithm, we have doubled the surface area estimate to 3.0 mm^2 for baseline conditions (and varied this further as part of the parameter sensitivity study, below). Using all three channels, the volume of the whole node was reconstructed and calculated to be 0.18 mm^3 , which results in the blood vessel area density (A) to be 16.6 mm^{-1} .

2.2.7. Parameter Estimation

The density and viscosity of the lymph flowing in the node were assumed to be 1000 kg/m^3 and $0.0015 \text{ Pa}\cdot\text{s}$ respectively [130]. The hydraulic conductivity for the B-cell follicles and T-cell cortex was assumed to be isotropic, at a value of $2.5\text{e-}7 \text{ cm}^2/\text{s}\cdot\text{mmHg}$, similar to those measured in LS174T tumours [131, 132]. Because of the structural complexity and lack of information on the hydraulic conductivity of medullary sinus (MS), its baseline value was assumed to be three orders of magnitude higher than the other porous regions. Parameter sensitivity analysis was done to better investigate the effect of this parameter. For the blood vessel walls in the node, $7.3\text{e-}8 \text{ cm/s}\cdot\text{mmHg}$ was assumed as the average hydraulic conductivity, in part based on the measured hydraulic conductivity of rat mesenteric venular microvessels *in situ* of $7.3\text{e-}8 \text{ cm/s}\cdot\text{mmHg}$ [133]. Cultured endothelial cell monolayers are shown to have higher hydraulic conductivity in the range of $1.2\text{-}3.6\text{e-}7 \text{ cm/s}\cdot\text{mmHg}$, which increased 2.16-fold when shear stress of 10 dyn/cm^2 was applied for the duration of 1 hr [134]. It is noteworthy that the hydraulic conductivity of the medulla is the conductivity of the 3D porous tissue whereas the hydraulic conductivity of the blood vessels is the conductivity of the vessels wall as a

membrane. Oncotic pressures in the blood (11.5 mmHg) and lymph (3.8 mmHg) were based on the assumption that the protein content of lymph is 40% of that of the plasma [130, 135] and the previously measured mouse plasma protein content of 4 g/dL [136]. σ was measured to be 0.88 by Adair et al. for canine popliteal LNs and is assumed to be the same for the mouse popliteal LNs [137]. Baseline average blood vessel pressure (P_{BV}) is taken to be 5 mmHg in the baseline case that is similar to the values used by Adair et al. in the experiments on canine LNs [124].

2.2.8. Parameter Sensitivity Analysis

A high-throughput parameter sensitivity analysis was done with the Optimate+ plugin in the STAR-CCM+. Four parameters were varied over a range of values to investigate the effect of each parameter on the outputs of the system. Because blood vessel wall hydraulic conductivity and surface area of the blood vessels always appear together in the Starling's equation (Equation 2.3), the parameter sensitivity analysis was done for the product LA . Hydraulic conductivity of medulla was varied over four orders of magnitude because of its complex structure and lack of experimental characterization. The effects of pressure boundary conditions at the efferent vessel (P_{Ef}) and the blood vessels (P_{BV}) were studied in the range of 0-30 mmHg and 0-20 mmHg respectively.

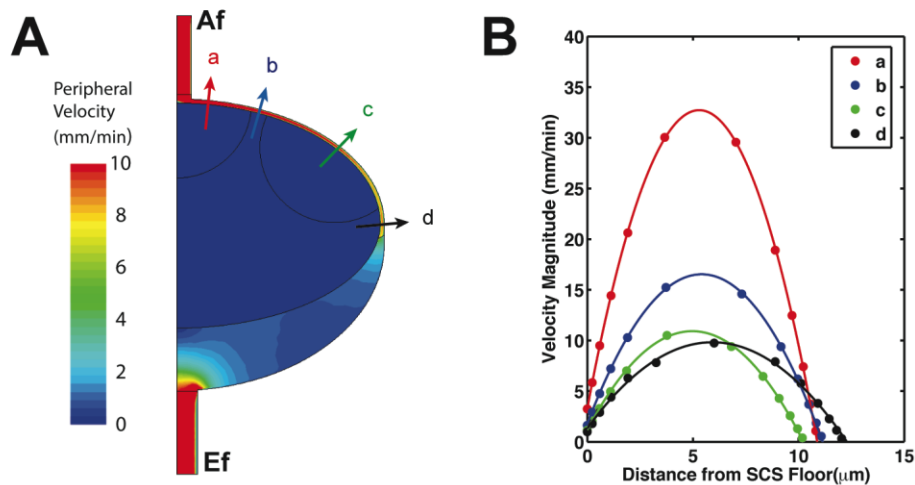


Figure 2.3. Peripheral velocity contours and velocity profiles along the SCS. **A.** Velocity contour of peripheral path shows that lymph flows from SCS directly to the medulla with velocities that are approximately three orders of magnitude higher than the velocities in the central path. The afferent vessel is located at the top and the efferent vessel at the bottom. Vectors a, b, c, and d show locations along SCS that the lymph velocity profile in the SCS is plotted. **B.** Velocity profiles along the SCS demonstrate that the peak velocity of the lymph in the SCS decreases as lymph travels further from the afferent vessels. This is mainly a result of the surface area in front of the flow increasing with distance along the approximately spherical surface. The velocity profiles correspond to the locations in panel **A** and are plotted from the SCS floor to the SCS ceiling.

2.3. Results

2.3.1. Flow Patterns under Baseline Conditions

Pressures and velocities. Most (93%) of the 133 nL/min of afferent flow moved peripherally (Figure 2.2C) around the SCS to the MS, because this pathway presents less resistance to the incoming flow (Figure 2.3A). There was a total of 9.7 nL/min (7% of afferent flow) that moved centrally (Figure 2.2C) into the paracortex and eventually exited through the blood vessels. The direction of fluid movement is dictated not only by the resistance to flow (porosity, in the case of the B cell follicles and T cell zone), but also the pressure distribution. The pressure near the centre of the paracortex was 2.9 mmHg, compared to 3.9 mmHg in the afferent vessels and

3.0 mmHg in the efferent (Figure 2.4). The efferent pressure is imposed as a boundary condition, while the afferent pressure is determined by the driving pressure necessary for the specified inlet flow rate at the afferent vessel. Of the 9.7 nL/min absorbed by blood vessels, 4.0 nL/min flowed to the parenchyma directly from the SCS, and the rest was supplied by peripheral flow entering from the T cell cortex/medulla interface. While velocity vectors in the central regions (B cell follicles and T cell zone) of the LN illustrates that the lymph moves towards the low pressure region at the centre (Figure 2.4), the velocity magnitudes are approximately three orders of magnitude lower than those in the peripheral regions (SCS and MS, Figure 2.3).

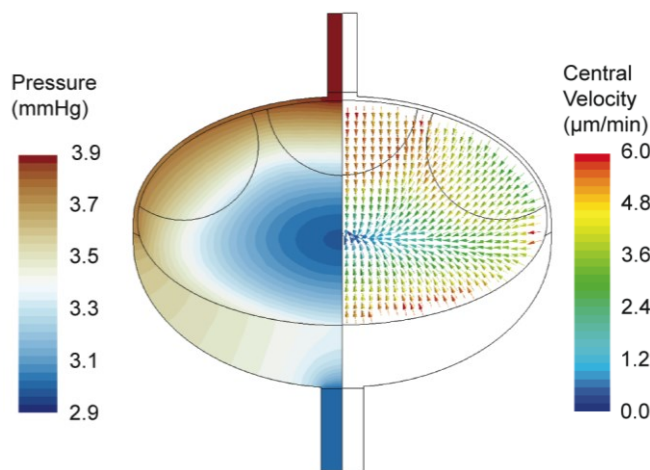


Figure 2.4. Pressure contours and lymph velocities. The left half of the lymph node is colour coded for lymph pressure. The right half shows the velocity vectors in the central region that are colour coded with the magnitude of the velocity. Fluid moves towards the low pressure region at the centre with velocities that are three orders of magnitude smaller than the peripheral region.

Shear stress in SCS. Velocity profiles across the SCS showed higher maximum velocities near the afferent vessel, where lymph enters the node, but although the profile stayed parabolic (expected in low Reynolds number regime), the maximum velocity decreased as the distance from the afferent vessel increased. The no-slip boundary condition imposes zero velocity on the impermeable ceiling of the SCS,

but the boundary between the SCS and porous central zone results in non-zero velocities. The wall shear stress contours demonstrate that the shear stress at the subcapsular sinus ceiling decreases with distance from the afferent vessel (Figure 2.5A). In the baseline case, the shear stress gradually decreases from $\sim 6 \text{ dyn/cm}^2$ close to the afferent vessel to $\sim 0.5 \text{ dyn/cm}^2$ at the medulla. The shear stress at the ceiling was approximately 10% higher than that on the floor, due to the porous boundary there (Figure 2.5B). Increasing the afferent flow rate resulted in proportionally higher overall shear stresses (Figure 2.5B).

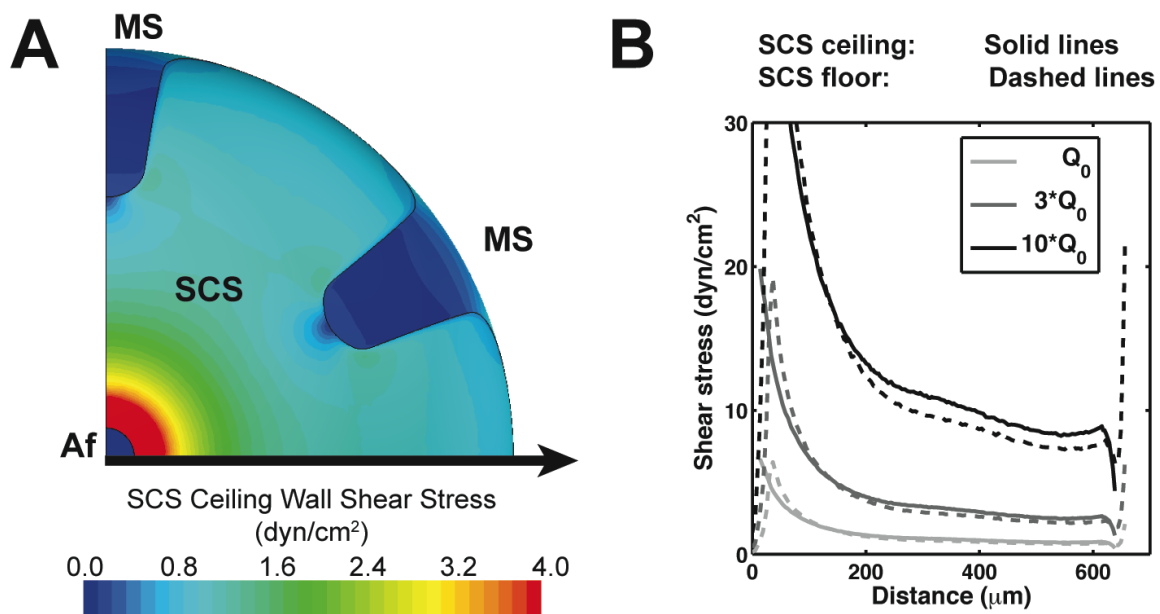


Figure 2.5. Shear stress contours in SCS and differences between shears on the SCS ceiling and floor. **A**. Shear stress contours on the SCS ceiling demonstrate that shear decreases as lymph travels further away from the afferent vessel. The contour is produced by looking down toward the SCS ceiling from afferent vessel (top view of the LN). **B**. Shear stress versus distance from the afferent vessel (along the black arrow in panel **A**) shows the dependency of the shear stress profile on the afferent flow rate. Additionally, shear stress on the SCS ceiling (solid lines), are on average 13% higher than the shear stress on the SCS floor (dashed lines).

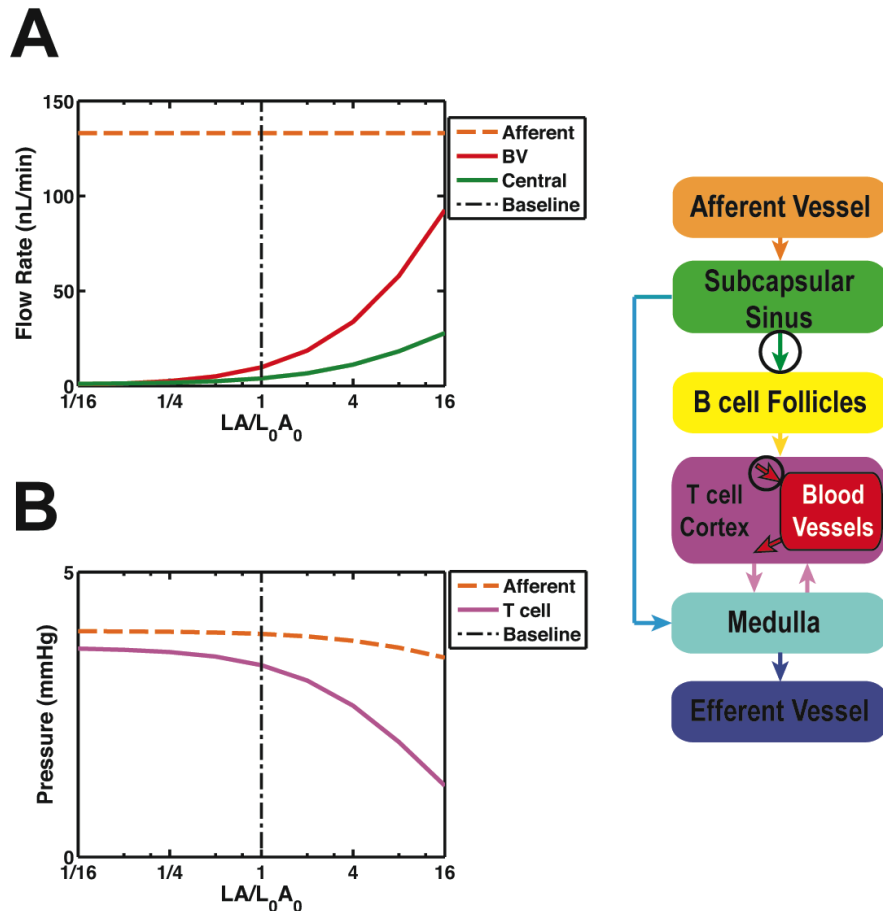


Figure 2.6. Parameter sensitivity analysis for surface area density and hydraulic conductivity of the blood vessels. **A**. Flow rates in the LN as a function of LA . Afferent vessel flow rate (dashed orange line) is kept constant. Increasing LA resulted in the increase in the amount of fluid absorbed by blood vessels (solid red line). Additionally, the flow through central path (solid green line) increased with LA . **B**. Holding efferent pressure constant, increasing LA will reduce the pressure at the Afferent vessel (dashed orange line) and more noticeably in the T cell area (solid pink line).

2.3.2. Parameter Sensitivity Analysis

Surface area and blood vessel wall hydraulic conductivity. The amount of lymph transported from the lymph passages to the blood (Q_{BV}) is very sensitive to LA , and monotonically increases with this parameter (Figure 2.6A). A sixteen-fold increase in LA resulted in elevation of fluid exchange from 7.4% to more than 70% of the afferent flow. In this case, the proportion of the flow coming from the SCS interface

(“central” flow in Figure 2.6A) versus that coming from the MS interface slightly decreased from 40% to 30%. The average pressure in the T cell cortex decreased to 30% of the baseline value when LA increased by sixteen-fold, whereas the afferent pressure showed a subtle decrease with the increase in LA (Figure 2.6B). Decreasing LA below baseline had very little effect on flows and pressures.

Hydraulic conductivity of the medulla. $K_{medulla}$ was a major determinant of the apparent resistance of the whole node (Figure 2.7A). Due to the complex porous structure of the medulla (and lack of experimental data), we investigated the effects of varying $K_{medulla}$ over four orders of magnitude. Lower values of $K_{medulla}$ resulted in much higher apparent node flow resistance, and subsequently much higher inlet pressures were required to drive the specified flow rate. As an example, a decrease in $K_{medulla}$ two orders of magnitude from the baseline value increased the apparent resistance of the node from 6.8 to 285 mmHg/(μ L/min), resulting in a predicted afferent pressure of 41 mmHg to just maintain the baseline lymph flow. At high $K_{medulla}$, most of the lymph passed through the peripheral lymph flow path with little to no dependence on $K_{medulla}$ (Figures 2.7B). The effect changed at lower values of $K_{medulla}$ where the central flow increased (Figure 2.7B); for instance, two orders of magnitude reduction in $K_{medulla}$ increased the central flow from 4 nL/min to more than 50 nL/min. At lower values of $K_{medulla}$, Q_{BV} increased to as high as 44% of the afferent flow rate for $K_{medulla}/K_{T\ cell\ cortex}$ of 0.1 for the baseline LA value (Figure 2.7C). To understand this behaviour better, we plotted the average lymph pressure in the T cell cortex, and showed that overall the pressure increases in the node when $K_{medulla}$ decreases (Figure 2.7D). Changes in central flow and exchange flow were similar at higher LA values but with higher flow rates.

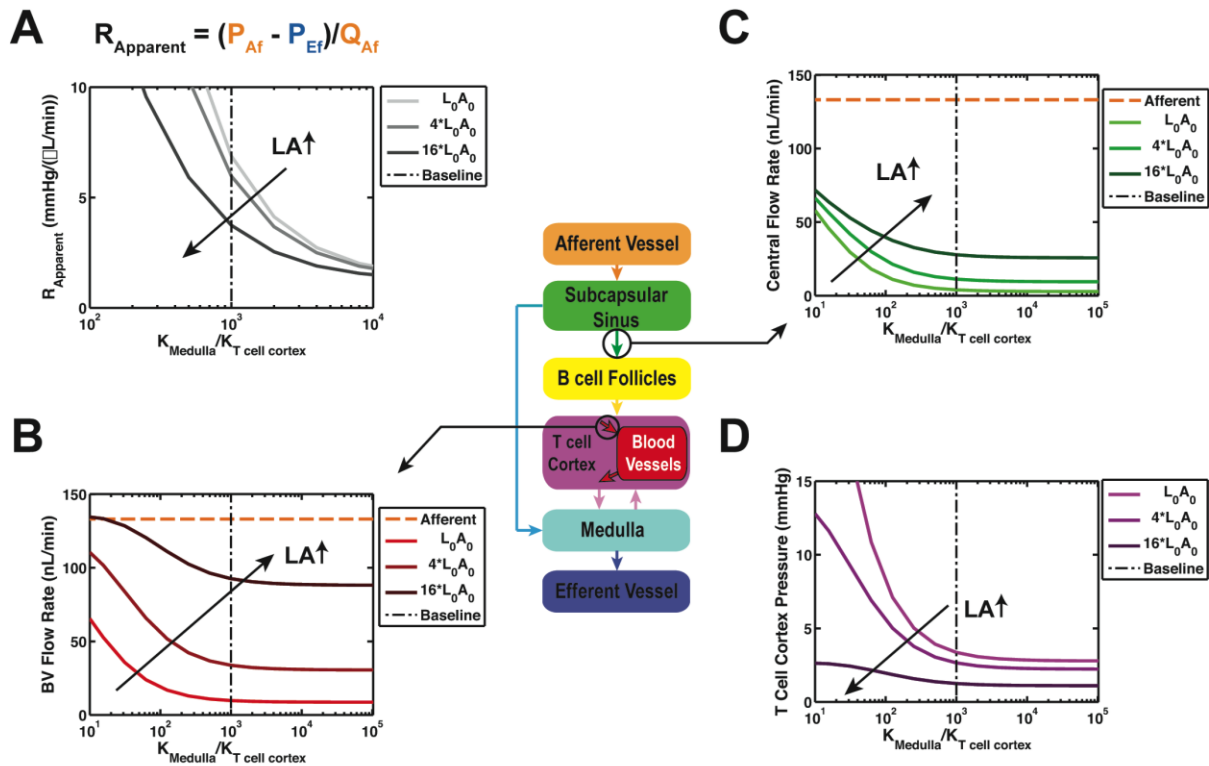


Figure 2.7. Parameter sensitivity analysis for hydraulic conductivity of medulla. **A**. A decrease in the hydraulic conductivity of medulla (K_{medulla}) results in an increase in the apparent resistance of the whole node. This parameter relates the pressure drop across a LN to the flow going through the node. **B**. The central flow increases when hydraulic conductivity of the medulla decreases with respect to hydraulic conductivity of T cell cortex ($K_{\text{medulla}}/K_{\text{T cell cortex}}$). As the K_{medulla} decreases, more of the lymph passes through the central regions of the node. **C**. Under the same condition, fluid transported to blood vessels also increases with the decrease in K_{medulla} . This study suggest structural changes in the medulla can modulate the transport of signalling molecules towards the blood vessels. **D**. The average pressure in the T cell cortex is an output that can be used to determine the physiologic range of K_{medulla} . This suggests that K_{medulla} should be about three orders of magnitude higher than $K_{\text{T cell cortex}}$ to ensure the pressure in the T cell cortex of the node is physiologic.

Blood pressure. The exchange flow between the lymphatic and blood vessels decreased quite linearly with the increase of P_{BV} (Figure 2.8A). At low P_{BV} , Q_{BV} was positive, meaning that fluid was being transported from lymphatic channels to blood vessels. Increasing P_{BV} lowered Q_{BV} , and eventually reversed the flow direction at $P_{\text{BV}} = 10.5$ mmHg. A similar behaviour with higher flows was observed with higher

values for LA , but the pressure that Q_{BV} changed direction remained the same. Average pressure in the T cell cortex increased linearly with P_{BV} ; a pattern that remained the same for higher LA values, but with steeper pressure changes (Figure 2.8B).

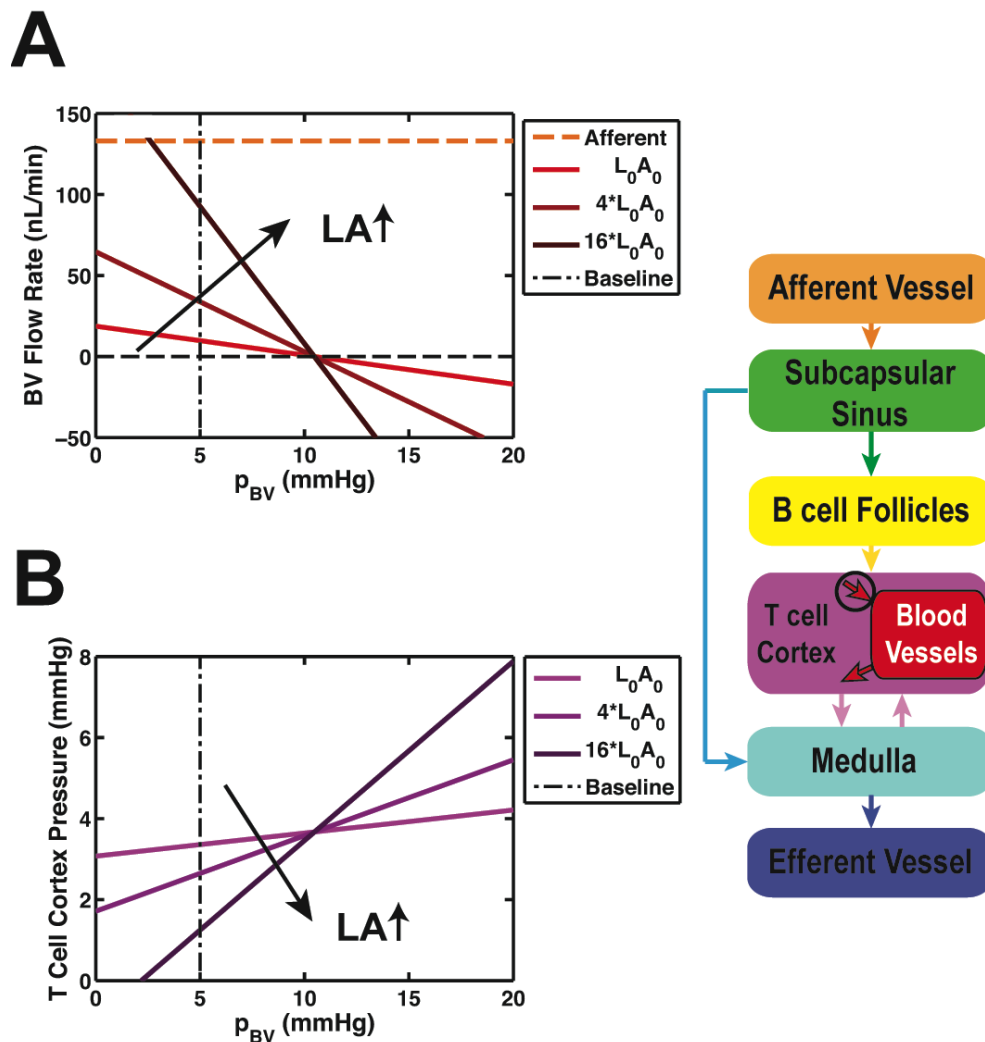


Figure 2.8. Parameter sensitivity analysis for average blood vessel pressure (P_{BV}). **A.** Blood vessel flow shown for different LA values decreases almost linearly with increasing P_{BV} . Additionally at around $P_{BV} = 10.5$ mmHg, the flow that was from lymphatic system to blood vessels changes direction to flow from blood vessels to lymphatics. **B.** The average pressure in the T cell area varies linearly with P_{BV} , with a slope that is dependent on surface area.

Efferent lymph pressure. Q_{BV} also showed a linear dependency on P_{Ef} over a wide range of pressures from 0 to 30 mmHg (Figure 2.9A). Q_{BV} increased with P_{Ef} at a slope that was dependent on LA . For the baseline LA , Q_{BV} increased from 9.7 to 58.1 nL/min as P_{Ef} went from 3 to 30 mmHg. Steeper changes were observed for higher LA values. Moreover, pressure in T cell area increased with P_{Ef} , but higher LA values countered that effect (Figure 2.9B).

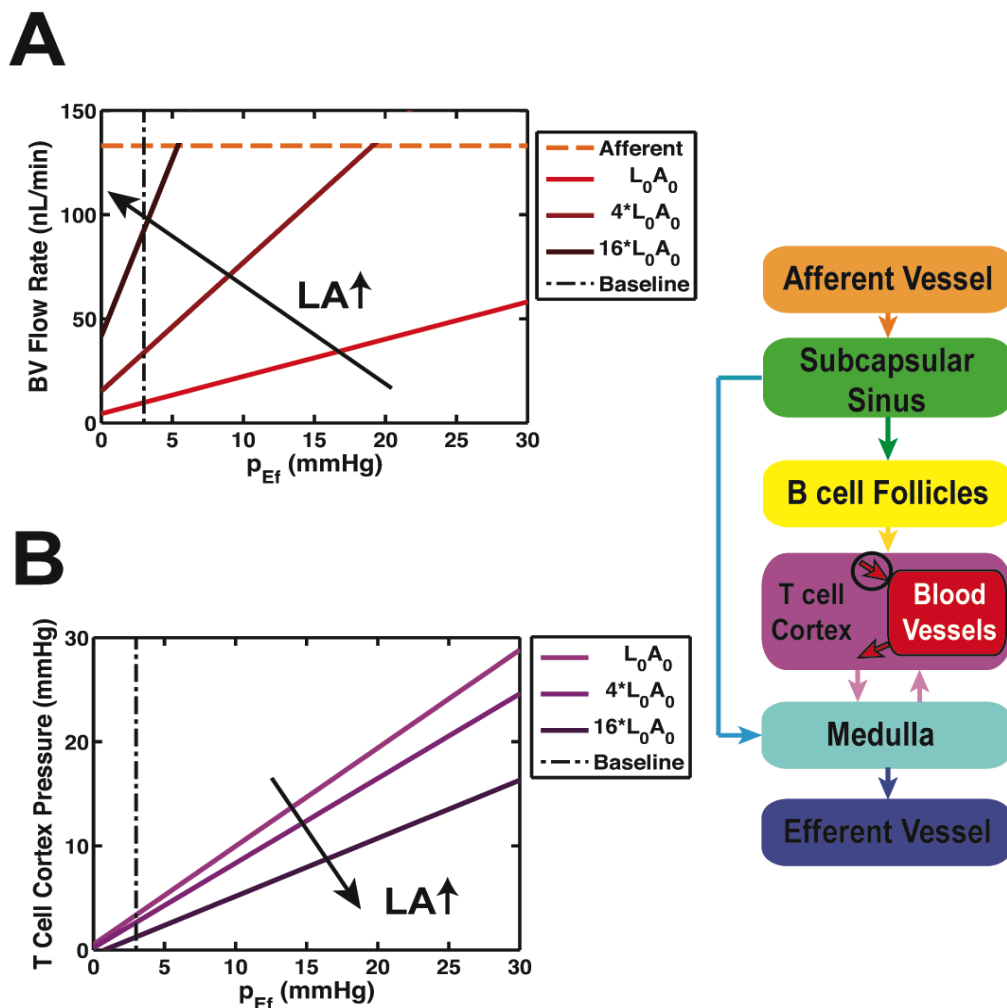


Figure 2.9. Parameter sensitivity analysis for efferent pressure. **A**. The exchange flow to blood vessels increases with the efferent pressure. The higher the LA value, the more fluid is transported to the blood vessels. **B**. The increase in the overall pressure in the lymph node is the main reason for the increase in the flow to blood vessels.

2.4. Discussion

The aim of this study was to provide quantitative insight into lymph flow and pressure distributions in nodes. Because it is practically impossible to measure these quantities in vivo, we have constructed a model based on the available experimental data. Models of this nature provide the advantage of being able to vary parameters over wide ranges to investigate their effects on important physiological outcomes such as fluid exchange with the blood vessels, lymph pressures and the overall resistance of the LNs. This not only helps confirm the realistic nature of the model, but can also provide “brackets” around parameters that defy experimental investigation. Because of the relatively good availability of the morphometric data from our labs and others, we constructed our model with dimensions and main features of a mouse popliteal lymph node. This model is the first of its kind to the knowledge of the authors to investigate fluid transport in a whole lymph node.

A major finding is that typically about 90% of the afferent lymph flow is directed around the periphery through the SCS and MS, because this is the path of least resistance. Flow through the T cell region, therefore, depends on the gradual entry of lymph from both the SCS (either directly or via the B cell follicles) and the MS. In the SCS itself, the reduction in velocity with distance from the afferent vessel was due mostly to the increase in cross-sectional area moving down from the “pole” of the approximately spherical surface, and partly due to the inward fluid percolation through the SCS floor. The velocity profile maintains a parabolic shape along the SCS from the Af toward MS, which is because of the highly viscous nature of the flow (Reynolds number < 1). The wall shear stresses we predict along the walls of the SCS are, interestingly, within an order of magnitude of those in prenatal

collecting lymphatics that lead to the afferent lymphatics of the rat mesenteric node [30], as well as those in larger blood vessels such as the aorta [138].

The predominance of flow around the periphery of the node raises the question of how the system is able to transport lymph-borne immune cells, antigens, etc. into the parenchymal zone where much of the immune processing takes place. While some advective transport is expected because of the relatively small amount of inward fluid movement, it is possible that other mechanisms, such as chemokine concentration gradients in the SCS, help in active migration of incoming cells toward the parenchyma. The wall shear stress on the ceiling of the SCS (which decreases along with velocity moving toward the MS) likely modulates the production of not only chemokines by the LECs that line this surface, but also the expression of atypical chemokine receptors such as ACKR2 and ACKR4 (LECs along the SCS floor do not express ACKR4) [19, 139]. Ulvmar et al. demonstrated that ACKR4 is essential in maintenance of CCL19 and CCL21 gradients in the node, which are shown to be crucial for DC migration to LN parenchyma [19]. The link between shear stress and chemokine release and chemokine receptor expression on LECs in the nodes has not yet been addressed in any experimental work, nor in our model.

Our model demonstrated that under baseline conditions, some of the fluid flows from lymphatic passageways to blood vessels in LNs. Based on Starling's equation (Equation 2.3) and knowing that the protein concentration in the lymph is usually lower than blood [130], oncotic pressures favour the movement of fluid from lymphatic to blood vessels. Experiments by Adair and Guyton on canine popliteal LNs showed that protein concentration of the lymph increases as it passes through LNs, mainly due to fluid transfer to the blood vessels [124]. Knox and Pflug had reported the same phenomena of fluid transport from lymph to blood and reported

up to 50% of afferent fluid being absorbed in canine popliteal LNs, resulting in the protein rich-efferent flow [140]. This transport of fluid from lymph to blood has had little attention, however it is important in directing the fluid to the central regions of the nodes via conduits, and can potentially modulate the way LN respond to inflammation. It is noteworthy that our model showed that blood vessel pressure is the only parameter that can change the direction of the exchange flow, with the other parameters affecting only the amount of flow. This change in the direction of flow with increasing blood pressure has been previously observed experimentally by Adair and Guyton in canine popliteal LNs [124] (Figure 2.10A).

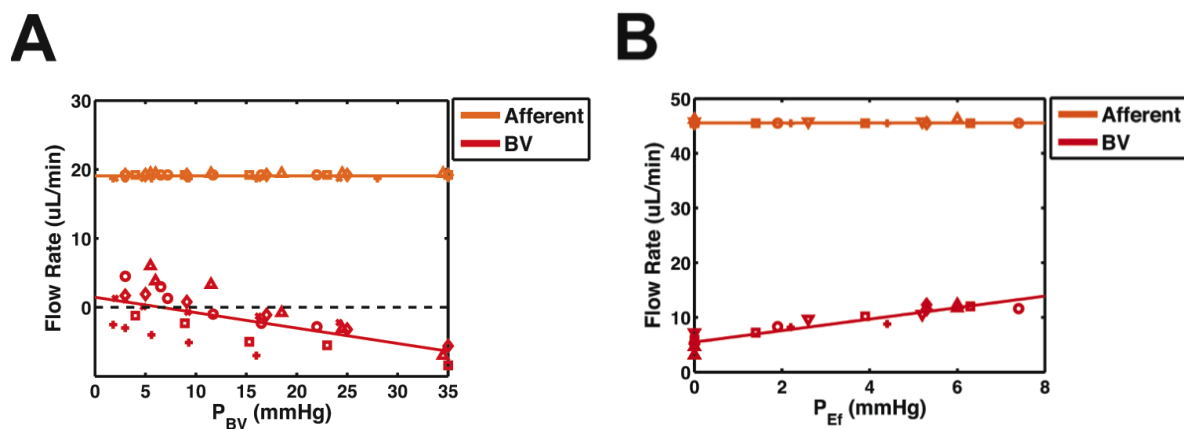


Figure 2.10. Comparison to experimental data from Adair and Guyton [124, 125]. **A.** The data from the cannulation of the popliteal node of six greyhounds perfused with constant afferent flow rate shows that increasing blood pressure decreases fluid flow from lymph to blood, and if high enough, it can change the flow direction. Each symbol shows a single experiment and the colour coded lines are linear fits to the data. The exchange flow to the blood vessels is shown in red while afferent lymph flow rate is plotted in orange. The trend of the change and the linearity of the response supports the results of our model showing the flow to blood vessel for the mouse popliteal LN (Figure 8A). **B.** Using a similar method, Adair and Guyton showed that an increase in the efferent pressure will increase the flow to blood vessels. This also agrees well with the model results in terms of trend and linear dependence of exchange flow on P_{Ef} .

They observed consistently that with the increase in the venous pressure, the efferent lymph protein concentration decreased while the mass flow rate of the

proteins stayed constant [124]. Our model demonstrated that the magnitude of the exchange flow is determined by surface area and hydraulic conductivity of blood vessel wall (LA), and predicted that a moderate level of increase in this combined parameter has a profound effect on fluid balance. Increases in LA could come from an increase in blood vessel wall hydraulic conductivity or increased blood vessel surface area (from either vasodilation or blood vessel network expansion), any of which could occur as part of immune response. In these cases, such actions would increase the amount of fluid bathing the follicles and cortex through the central path to the blood vessels and the HEV. Experiments by Kumar et al. showed that blood vessel surface area increases after immunization and induced viral infection [11, 73]. Furthermore, changes in lymph oncotic pressure or σ would have a similar effect as variations in blood vessel pressure, as the oncotic pressure driving term is linearly added in Starling's equation. In other words, if the protein concentration of the lymph increases during inflammation as it commonly does because of the increase in blood microvessel permeability seen with inflammations (i.e. such as seen with histamine), it would have a similar effect as an increase in blood pressure, and hence will decrease the lymph/blood exchange flow and encourage the change in the direction of this flow (Figure 2.8A).

A limitation to constructing our model was the lack of information on the porosity of the MS. However, we have demonstrated that hydraulic conductivity (inverse of resistance) of the medulla should be at least three orders of magnitude higher than that in the T cell region to avoid unphysiologically high fluid pressures in the node. Decreasing $K_{medulla}$ increases the central flow in the LNs. The effect of local hydraulic conductivity changes on nodal flow distributions has not yet been experimentally estimated, to the knowledge of the authors. Enhanced immune cell

trafficking through the node during inflammation might result in restricted passageways for the lymph flow through the medulla, further modulating the flow distribution. This would favour the fluid movement through central path and would result in higher pressures in the afferent vessel and parenchyma. Based on Starling's equation, higher overall pressures in the node would increase the pressure difference and hence boost fluid exchange to blood vessels. There is experimental evidence that inflammation can increase LN resistance. Nagai et al. measured the resistance of rabbit popliteal LNs to be 0.38 mmHg/(μ L/min) and it was increased to 1.01 mmHg/(μ L/min) after induced acute inflammation by formyl-Met-Leu-Phe-OH known to activate polymorphonuclear leukocytes [141]. Because resistance is dependent on the size of the system and our model is based on mouse popliteal LN, no direct comparisons can be made about the resistances.

Lymph velocities were lower in the central regions of the node compared to the peripheral path. The velocities were in the order of 1-10 μ m/min in the T cell cortex, for the baseline case (Figure 2.3), and scales with the amount of Q_{BV} for different cases of parameter sensitivity analysis. This velocity range is close to the estimated velocities used in the literature; for instance Tomei et al. used similar fluid velocities of 1, 10 and 23 μ m/min in 3D cultures of FRCs to investigate the effect of shear stress on these essential stromal cells of LNs [142]. They have demonstrated that the resulting shear stresses induce upregulation of CCL21 in cultured FRCs in 3D matrix. Furthermore, the velocity vectors in this study revealed that under the assumed baseline condition, fluid should move from the medulla towards T cell cortex (Figure 2.4). This suggests that the direction of lymph flow in the deep blunt-ended cortical sinuses in the node is towards the cortex. S1P1 signalling is shown to regulate T cell egress through cortical sinuses, some of which are blunt-ended [143].

Therefore, the intuitive concept that lymph should always move towards the efferent lymphatic is not necessarily correct everywhere in the node. In the cortical sinuses that connect SCS to MS, the lymph flows from the higher pressure SCS to lower pressure MS. However, for the blunt-ended sinuses, the closed end is connected to lower pressure parenchyma resulted from oncotic pressure differences, which can deliver the fluid towards the T cell cortex and blood vessels in this region.

The lymph pressures in the LN are directly modulated by the afferent and efferent pressures as the boundary conditions. In the basal condition, our model showed the pressure in the node to be in the range of 2.9-3.9 mmHg. Bouta et al. made *in-situ* measurement of pressure in mouse popliteal LNs and found it to be 6.86 ± 0.56 cmH₂O (5.04 ± 0.41 mmHg) for WT mouse [144]. The efferent lymph pressure was not measured in those experiments so direct comparison with this study is not possible. Increasing efferent lymph pressure increased the fluid exchange from lymph to blood vessels due to increased overall pressures in the LN (Figure 2.9B). This behaviour is similar to that observed experimentally by Adair and Guyton in canine popliteal LNs [125] (Figure 2.10B). They observed an increase in the fluid exchange from lymph to blood up to pressures of about 8 mmHg. Further increase in the efferent pressure resulted in the leakage of the dye from the node capsule. Additionally, in serially connected nodes, changes in a downstream node resistance provoked by infection and/or inflammation could result in a dramatic increase in the efferent pressure of the upstream LNs. Basal levels of fluid exchange do seem to be dependent on the anatomical location of the node and its resulting position in the resistance network. Popliteal and renal LNs are shown to have higher fluid exchange rates compared to hepatic LNs in sheep and greyhounds [137, 145].

As discussed earlier in the Introduction Chapter, Cooper et al. [113] published an image based model of flow through mouse popliteal LN. Although some of the general conclusions that explain the experimental data of Adair and Guyton were similar to current work, their model was very different to the one discussed here in many other accounts. In their mouse popliteal LN model, they prescribed a flow boundary condition at afferent vessel of $7.6e-7$ kg/s based on the canine study of Adair and Guyton. This resulted in an average velocity of 96.7 mm/s in an assumed 100 μ m afferent vessel (which is an overestimate of the afferent vessel diameter) leading to average velocities that are more than an order-of-magnitude greater than velocities measured in collecting lymphatic vessels experimentally [30]. Furthermore, due to the lack of incorporation of SCS, their model predicted much higher overall hydraulic conductivity ($3.4e-2$ cm²/s.mmHg compared to $2.5e-7$ cm²/s.mmHg measured in tumours [131, 132]) even in the central regions of the LN.

Due to the complexity of the structure and lack of experimentally measured properties of LNs, computational modelling of the lymph flow is challenging. Parameter sensitivity analysis helps reveal the relative importance of parameters that have yet to be measured accurately, or cannot be measured. Our analysis showed that the surface area of the blood vessels in the node is a crucial parameter determining the amount of fluid exchanged by blood vessels. Although there are quantitative measurements of the total length and average diameter of the HEVs (only a portion of the total surface area available for fluid transport) in the healthy and infected nodes [11], the total surface area of the blood vessels including capillaries has not been measured. After this work was finished and accepted for publication, a recent paper was published that finely segmented and quantified the blood vessel network of the LN [80]. Kelch et al. [80] showed that the surface area

density considering all the capillaries is 16.5 mm^{-1} , which is extremely close to the estimated surface area after correction for capillaries (16.6 mm^{-1}). Although, our model assumes the blood vessels are only in the T cell zone, Kelch et al. [80] showed that the distribution is more complex and perhaps a nonhomogeneous distribution of surface area density is needed for future studies. The present model assumes a uniform pressure in the blood vessels throughout the LN. In fact the blood pressure in the vessels drops by typically $>10 \text{ mmHg}$ moving from the arterioles to the capillaries and then venules. Inclusion of the variable blood pressure distribution requires better characterization of diameter, length, and location of all blood vessels in LNs. Hydraulic conductivity and permeability of the porous regions of the node (e.g. B cell follicles, T cell cortex and medulla) are other parameters of the system that need experimental measurements. Most LNs in the body have multiple afferent vessels. Comparison with models including several afferent vessels (not shown here) confirms that the major flow features are not greatly affected. The main parameter that is affected by the multiple afferent vessels is the local wall shear stress patterns in the SCS. In addition to the limitations discussed so far, the present model assumes that the B cell follicles and T cell cortex are homogenous and isotropic materials meaning there is no directionality in the uniform structures. Addition of the conduit system of the lymph node to the model is crucial as the next step to investigate the antigen and chemokine transport in LNs [78, 79]. Moreover, Ushiki et al. had shown that the conduit structure near the capsule is generally directed towards the centre of the node [146]. In a very recent study by Rantakari et al., the main mechanism for size exclusion in the conduits of the LN was shown to be the formation of a diaphragm on the fenestrae and caveolae of lymphatic endothelial cells by the PLVAP molecule. Addition of the conduit system is essential

for modelling of the antigen and protein transport in the LN [115]. However quantitative experimental data are necessary to be able to include the anisotropic and heterogeneous effects of conduit system of the node. Overall, this work aims to establish a model of fluid flow in healthy LN. Further progression of this model is needed to investigate pathologic conditions such as inflammation and infections in which the size of the LN changes dramatically [11]. In addition to the size change, Tan et al. demonstrated that initially subcapsular sinuses and later medullary sinuses expand as a result of prolonged inflammation by VEGF-A mediated lymphangiogenesis [13]. Based on the results on this study, any change in the hydraulic conductivity of the sinuses (which can be caused by lymphangiogenesis) could modulate the amount of lymph going through central versus peripheral paths in the LN. Furthermore, comprehensive experimental data on the structure of human LNs would be essential to translate the results of this study to human nodes.

In summary, we have constructed the first computational fluid dynamics model of lymph flow in lymph nodes, using a geometry based on mouse popliteal LNs. Our model showed that most of the afferent lymph flows through peripheral paths of the LNs in high velocities (mm/min), while smaller portion of the fluid slowly ($\mu\text{m}/\text{min}$) percolates through follicles and cortex. We performed parameter sensitivity analysis and identified that surface area of the blood vessels in the node is an important parameter of the system that needs to be accurately measured. Our model supports the concept that the direction of the exchange flow with blood vessels can be changed depending on the hydrodynamic conditions in the node, notably blood pressure and oncotic pressures, which can play a role in the function of the LNs during infection and chronic inflammation. Furthermore, changes in the resistance of MS can result in the diversion of the lymph to cortical regions of the node. It is

crucial to know how immune response, vaccination and remodelling of the lymph node will change the lymph flow and hence antigen, cytokine, chemokine and immune cell transport to different parts of the LNs.

CHAPTER 3

EXPERIMENTAL MEASUREMENT OF THE HYDRAULIC RESISTANCE OF MOUSE POPLITEAL LYMPH NODE

3.1. Introduction

Lymph nodes (LNs) located downstream of the peripheral tissues are essential in immune surveillance. Lymph containing fluid, proteins (including cytokines and chemokines) and cells such as antigen presenting cells (APCs, most importantly dendritic cells (DCs)) enter the initial lymphatics and are propelled by active contraction of collecting lymphatic vessels to LNs [71, 147]. Lymph enters the LN via afferent vessel(s) and is sampled and filtered as it passes through each zone of the LN [81, 119, 148]. Upon entry, lymph flows into the subcapsular sinus where it can either filter through a conduit system to enter the paracortex for subsequent exchange with blood vessels [81, 115], or it can take the longer (but less resistive) path along the capsule to medulla where it can continue its journey to enter the efferent vessel(s) and exit the LN [119, 148]. The active transport of tissue antigen and APCs to the draining LN is essential for adaptive immune response and immunological tolerance [149-151].

While LN contraction has been observed, its contribution to lymph propulsion is still in doubt [128, 152-154]. In the absence of a significant pumping contribution, LN present a passive resistance to afferent vessel pumping [128]. This view is supported by observations that afferent pressures are generally higher than the efferent pressures *in vivo* [63, 128, 155]. Zweifach and Prather [63] measured progressively increasing pressures of 12-18 cmH₂O upstream of rat mesenteric LN. On the other hand, downstream pressures to rat mesenteric LN are measured to be 1.1-3.4 cmH₂O in a study by Lee [155], suggesting that LNs act more as the resistive elements rather than pumps. In the simplest sense, a pressure difference across the LN (Δp) results in a volumetric flow rate through the node (Q) that increases with pressure difference. In the case of a linear relationship, the constant of

proportionality is defined as resistance ($R = \Delta p/Q$), which depends on the microstructure of the LN as well as the viscosity of the fluid passing through.

Many pathologic conditions can markedly change the LN structure, however, their effect on LN flow, and its redistribution to functionally-specific cellular compartments has not been adequately studied. Numerous viruses (e.g. Ebola, Lassa and Marburg) disrupt cellular architecture of the LN by interfering with the network of FRCs, which leads to destruction of the conduit system and elimination of distinct zones of B cell follicles and T cell cortex [50-52]. Moreover, experiments on human immunodeficiency virus (HIV)-1 infected rhesus macaques revealed regulatory T cell upregulation of TGF β 1 that induces collagen synthesis by FRCs [53]. LN fibrosis results in the loss of contact between FRCs and T cells, contributing to T cell apoptosis observed in HIV-infected patients [54, 55]. Additionally, cancer metastasis to downstream LN is shown to transform the architecture and organization of the node [156].

In addition to the direct effect of cancer cells and infectious viruses on LN compartments, inflammation causes LN swelling that is used to diagnose the stage of adaptive immune response. LN enlargement can be due to a combination of increase in cell numbers and fluid accumulation. Increase in the fluid volume of the LN requires expansion of the sinuses, which could result in the lowered LN resistance. Increase in the cell number can be separated into two phases: 1) enhanced retention of the immune cells, and 2) immune and stromal cell proliferation. Migration of activated DCs to LN as well as chemokine and cytokine signalling, enhances T cell and B cell entry through high endothelial venules (HEVs), and reduces the lymphocyte egress through downregulation of sphingosine-1 phosphate receptor (S1PR)1 on the cells [89, 143, 157]. Furthermore, the retained

and activated T and B cells proliferate to expand antigen-specific colonies, which boosts LN enlargement [158, 159]. Simultaneously, inflammation reorganizes and expands the main stromal cell populations, i.e. blood endothelium [160, 161], lymphatic endothelium [13, 162], and fibroblastic reticular cells (FRCs) [163, 164]. For instance, Tan and colleagues demonstrated that prolonged subcutaneous treatment of mice with lipopolysaccharides (LPS) resulted in lymphangiogenesis in subcapsular sinus after 4 days and then in cortical and medullary sinuses after 14 day [13]. The effect of cell number increase on LN resistance greatly depends on how the LN reorganization affects the fluid passageways, and cannot be confidently predicted without measurement. Accurate measurement of LN resistance in mouse, which is widely used for *in vivo* immunology experiments, would help us better understand how lymph flow is modulated by LN.

Physiological interest in lymphatic system has motivated several measurements of hydraulic resistance of LN in dogs and rabbits (Table 3.1) [125, 141, 165, 166]. Nagai et al. [141] measured LN resistance to be 0.38 mmHg/(μ l/min) (when increasing afferent pressure) or 0.44 mmHg/(μ l/min) (when decreasing efferent pressure) in rabbit popliteal LN. Paucity of fat tissue around lymphatic vessels and LNs in greyhound dogs has made them a good model for studying LN cannulation. Several studies have measured canine LN resistance to range from 0.028 to 0.152 mmHg/(μ l/min) [125, 165, 166]. There is an inverse correlation between the animal body mass and the resistance of the LN meaning larger animals have LNs with lower resistances (Table 3.1). Recent developments in mouse genetics have made mice the primary model to study molecular mechanisms of immune response against infection and inflammation. However, due in part to the

small size of the connecting vessels, no attempt has been made to characterize the fluid transport properties of mouse LNs.

Table 3.1. Comparison of measured LN resistance across species.

Study	Species	Body mass (kg)	LN Location	LN Resistance (mmHg/(μ l/min))	Reference
Ohhashi et al. (2008)	Japan White Rabbits	1.5 – 3.0	Popliteal	0.38 and 0.44* (mean)	[141]
Papp et al. (1970)	Dogs	14 – 20	Submandibular	0.051 \pm 0.008 (mean \pm SEM)	[166]
			Mediastinal	0.152 \pm 0.114 (mean \pm SEM)	
			Periportal	0.113 \pm 0.030 (mean \pm SEM)	
			Popliteal	0.035 \pm 0.006 (mean \pm SEM)	
Browse et al. (1984)	Greyhound Dogs	20-30	Iliac	0.068 \pm 0.015 (mean \pm SEM)	[165]
Adair and Guyton (1987)	Greyhound Dogs	30-40	Popliteal	0.028 \pm 0.010 (mean \pm STD)	[125]

* They used two different methods of increasing afferent pressure or decreasing efferent pressure for measuring LN resistance

While measurement of LN resistance provides valuable information about organ-wide modulation of flow properties, a computational model with similar geometry can complement the experiments by providing insight into the effect of individual compartments of LN. Comparing the computed resistance from computational model with measured resistance from experimental measurements allowed us to predict what structural change by inflammation could change LN resistance. Furthermore, it is important to understand if inflammation-mediated change in resistance can redirect the flow to specific regions of the LN for

modulation of antigen exposure that have immunological importance. A computational model of fluid transport provides us the tools to investigate the flow redistribution in the LN. This study aims to provide the first measurement of mouse popliteal LN resistance and to investigate how inflammation of the upstream tissue can affect the resistance of the LN. Furthermore, we complemented the experimental measurements with a computational model of fluid flow to investigate the kinds of structural and microstructural alterations that can result in those changes in the LN resistance with the aim to delineate the patterns of flow redistribution in response to inflammation.

3.2. Methods

3.2.1. Mouse Popliteal LN Isolation and Cannulation

Animal protocols were approved by the Institutional Animal Care and Use Committee (IACUC) at the University of Missouri-Columbia and conducted in accordance with the National Institutes of Health's *Guide for the Care and Use of Laboratory Animals*. C57BL/6 mice were anesthetized and an incision was made in the posterior of the hind leg to expose the popliteal LN. The mouse was injected with small amounts of stock Trypan blue (~50 μ l) subcutaneously in the footpad to enhance the contrast between the lymphatic vessels and surrounding tissues. Krebs buffer (contained (in mM) NaCl, 146.9; KCl, 4.7; CaCl₂·2H₂O, 2; MgSO₄, 1.2; NaH₂PO₄·H₂O, 1.2; NaHCO₃, 3; sodium-HEPES, 1.5; d-glucose, 5 and pH adjusted to 7.4 at 37°C) [167] was used during the dissection and handling to keep the tissue wet. Popliteal LN were meticulously separated from the surrounding tissue along with afferent and efferent lymphatic vessels (Figure 1A). One afferent and one efferent vessel were cannulated on glass pipettes of sizes 50-70 μ m in diameter

(Figure 1B). Additional afferent or efferent vessels and branches were closed off by sutures.

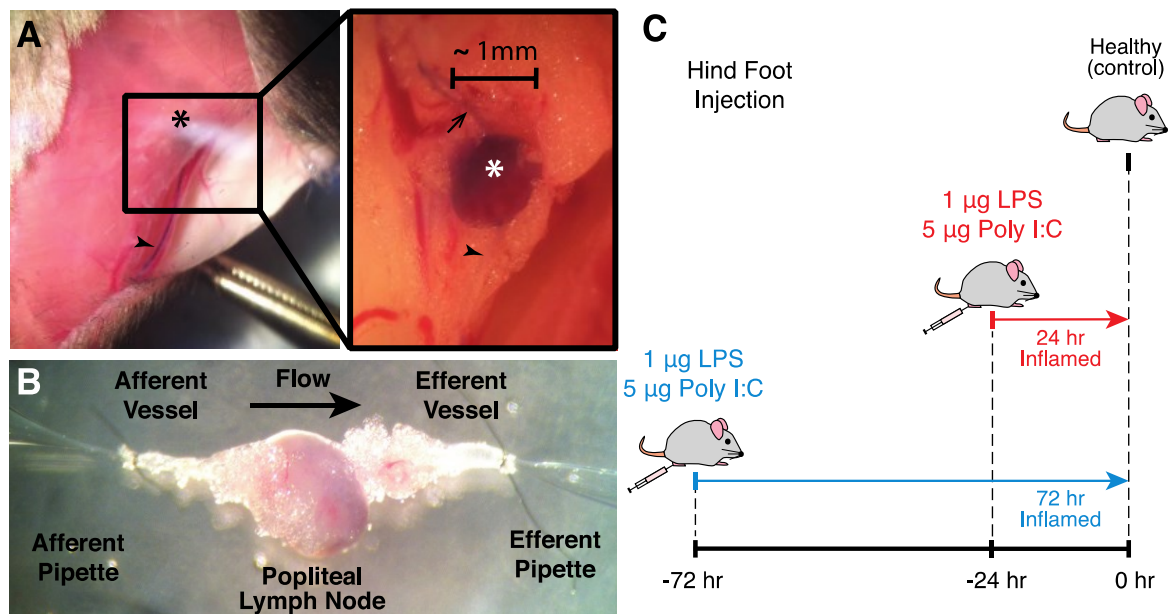


Figure 3.1. Mouse LN isolation and cannulation, and adjuvant treatment. **A**. An incision in the posterior of the hind limb exposed the afferent lymphatic vessel (arrowhead) leading to the LN (asterisk). The efferent lymphatic vessel (arrow) is also visible in the right panel. **B**. The node isolated node was cleaned and then cannulated on the class micropipettes of 50-70 μm . **C**. Experiments were done on healthy control animals (black, $n=6$), 24 hr inflamed with 1 μg LPS and 5 μg Poly I:C (red, $n=5$), and 72hr inflamed with 1 μg LPS and 5 μg Poly I:C (blue, $n=3$).

3.2.2. Footpad Injection of TLR Agonists

Animals were injected a single 20 μl shot of sterile physiological saline containing 1 μg of lipopolysaccharides (LPS, InvivoGen), and 5 μg of polyinosinic:polycytidylic acid (Poly I:C , InvivoGen), in each footpad either 24 hr or 72 hr before the experiments to induce regional inflammation in the popliteal LN (Figure 1C) [168-171].

3.2.3. LN Resistance Measurement Apparatus

The *iPerfusion* resistance measurement system developed at Imperial College was used to measure pressures and flows across cannulated lymph nodes (Figure 2A) [172]. Briefly, the system uses a linear actuator to position the upstream reservoir at a higher pressure compared to the downstream reservoir (fixed at 2.2 mmHg higher than tissue chamber). This pressure difference maintains a flow through a thermal flow meter (Sensirion, Switzerland) placed upstream of the cannulated LN. Due to the considerable pressure drop across the flow meter, the pressure drop across the sample was measured using a wet-wet differential pressure transducer (Omegadyne, USA). In all the cases a total 36 mmHg pressure was applied across the system, however the LN-associated share of the pressure drop was dependent on the resistance of the LN. The ratio of the resistance of LN to that of flow meter ($R_{\text{flowmeter}} = 8.74 \pm 0.24 \text{ mmHg}/(\mu\text{l}/\text{min})$) determined the percentage of the total pressure difference (Δp_T in Figure 3.2A) that dropped across the LN (Δp in Figure 3.2A). To measure the resistance, upstream reservoir was raised in nine steps of 4 mmHg (5 min each) while measuring flow and LN-specific pressure drop (Figure 2B-C). Krebs buffer with 0.5% albumin was used as the fluid of the system throughout the experiments. Additionally, the resistances of the afferent and efferent glass pipettes were measured before the experiments (Figure 2D). Mean and standard deviation (STD) of pressures and flows were calculated for the last 60 s of each inlet pressure step. Linear weighted regression was used to fit a line to Δp versus Q data points, with weights based on $1/\text{STD}^2$ for both pressure difference and flow [172]. Finally, the LN resistance was calculated by subtracting the resistance of pipettes from the total resistance (Figure 2E). Furthermore, diameters were measured from

the images of the afferent and efferent vessels using previously developed algorithm based on the contrast of the vessel wall with the background [173].

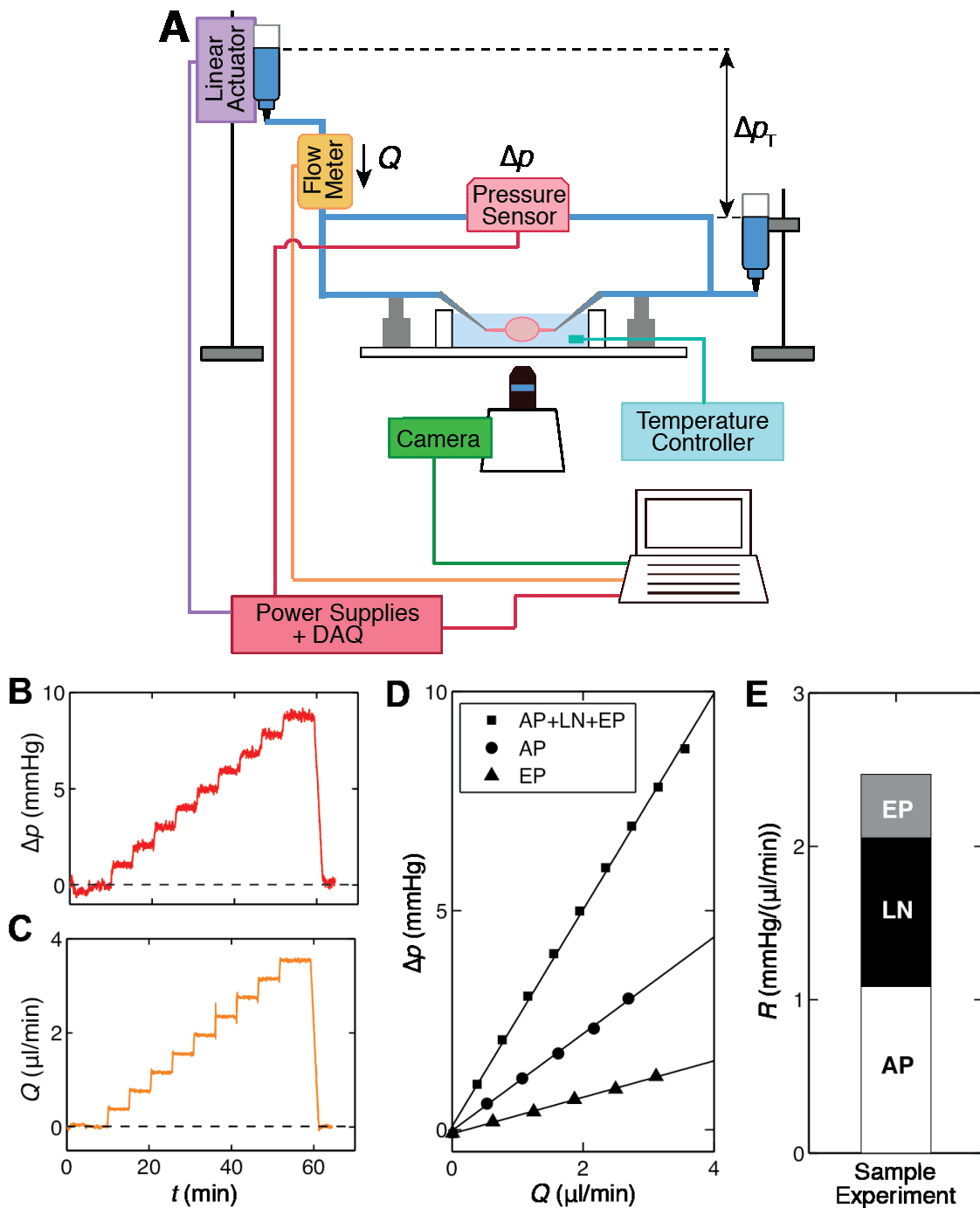


Figure 3.2. Measurement setup and sample pressure and flow traces for resistance calculation. **A**. The schematic of the setup is shown with all the components. The cannulated LN was connected to the actuator controlled upstream reservoir (on the left) and a stationary downstream reservoir (on the right). During the nine steps equivalent to 4 mmHg pressure increases, differential pressure across **(B)** and flow through **(C)** the sample was measured. The resistance was calculated by linear curve fit to the pressure-flow data **(D)**. Subtraction of calibrated afferent pipette (AP) and efferent pipette (EP) from the total resistance results in the LN resistance **(E)**.

3.2.4. LN Flow Model

The LN flow model was based on our previously published work [114]. Briefly, the continuity and Navier-Stokes equations were applied to the SCS, and Darcy's law with Brinkman's term was applied to the porous regions. An idealized LN geometry was developed, and a 3D computational mesh was generated using Solidworks 2012 SP4.0 (Dassault Systèmes, France) (Figure 4A). The governing equations were solved using ANSYS (Pennsylvania, United States). The fluid viscosity was set to 0.00089 Pa.s to match that of the 0.5% albumin/Krebs buffer solution that was used in the experiments [174]. We calculated the resistance of the LN while varying the hydraulic conductivity of medulla with respect to the hydraulic conductivity of T cell cortex ($K_{\text{medulla}}/K_{\text{T cell cortex}}$) over four orders-of-magnitude (range: 10^1 - 10^5). Moreover, the height of the subcapsular sinus was 20 μm in the baseline case but cases with 10 and 30 μm heights were studied to investigate the effect of subcapsular sinus height on overall flow resistance. The computational model was used to interpret the experimental data for better estimation of the hydraulic conductivity of medulla. We called the portion of the flow that goes from subcapsular sinus to B cell follicles and T cell cortex "central flow", and the flow that goes directly from subcapsular sinus to medulla "peripheral flow" (Figure 4A).

3.2.5. Statistical Analysis

Data are generally reported as the mean \pm STD. ANOVA was used to compare the results from diameters and resistances in the healthy control case with 24 hr and 72 hr of inflammation. Bonferroni correction was used to ensure statistical significance between group means. All the statistical analyses were done in MATLAB R2013a with a critical p -value of 0.05.

3.3. Results

3.3.1. Measurement of the Resistance of Mouse Popliteal LN

Pressure difference across LN versus flow data was best approximated by linear regression indicating that resistance appeared to be constant to the degree of accuracy of the measurement techniques over the ranges tested for control mice (Figure 3.3A, top panel). The LN resistance of healthy control animals ranged from 0.36 to 1.69 mmHg/(μ l/min) with an average of 0.81 ± 0.48 (mean \pm STD) mmHg/(μ l/min) (Figure 3.3C). Furthermore, we measured the diameter of afferent and efferent vessels and showed that afferent vessel was significantly smaller than efferent vessel (Figure 3.2B). The mean diameter of the afferent vessels was 85 ± 13 (mean \pm STD) μ m, whereas it was 153 ± 27 μ m for efferent vessels.

LPS and PolyI:C–induced inflammation caused an increase in the LN resistance at 24 hr and a subsequent decrease at 72 hr to levels near healthy control resistance. In 24 hr, the resistance ranged from 1.51 to 9.46 mmHg/(μ l/min) with an average of 5.05 ± 1.55 (mean \pm STD) mmHg/(μ l/min), an increase of 6.2X over healthy controls ($p < 0.05$, Figure 3.3C). Due to the higher resistances at 24 hr time point, the LNs experienced higher pressure drops and exhibited nonlinear effects in pressures higher than about 6 mmHg (Figure 3.3B, middle panel). For better comparison between the cases, we only took the data points with pressures less than 6 mmHg to fit the line for resistance calculations. At 72 hr post inflammation, the resistance ranged from 0.59 to 0.86 mmHg/(μ l/min) with an average of 0.76 ± 0.15 (mean \pm STD) mmHg/(μ l/min), which was significantly lower than 24 hr resistances but not significantly different from healthy controls (Figure 3.3C).

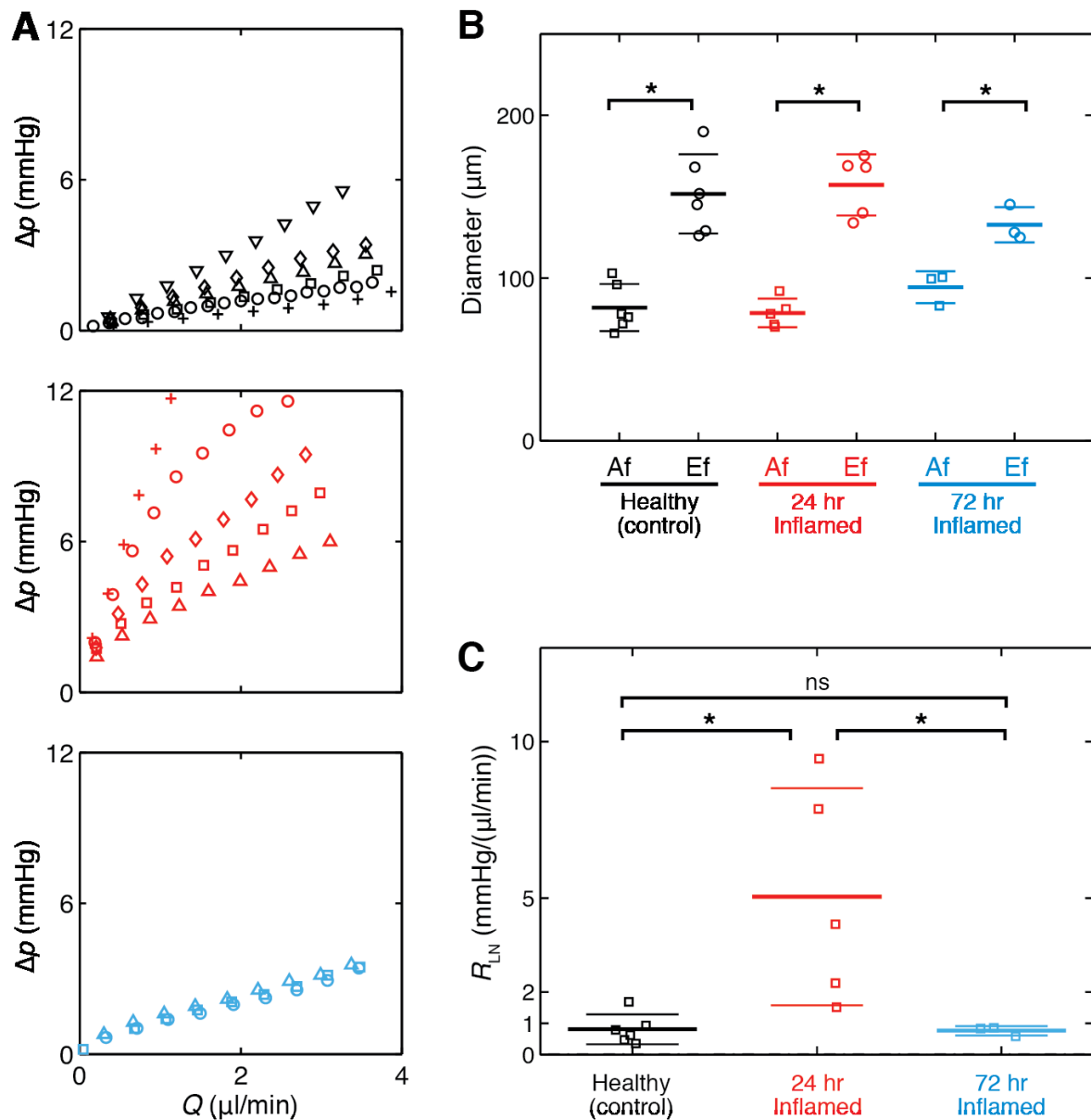


Figure 3.3. LN resistance changes with inflammation at 24 hr and 72 hr. **A**. Raw pressure versus flow data are shown for healthy WT (top panel and in black), after 24 hr inflammation (middle panel and in red) and after 72 hr inflammation (bottom panel and in blue). Each symbol shows the data from a single LN. **B**. Efferent vessel diameters were always larger than afferent diameters (statistically significant), however inflammation did not significantly change afferent or efferent diameter at 24 hr or 72 hr compared to control. **C**. The resistance of the LN significantly increased in 24 hr compared to control and then decreased to level not significantly different from control but significantly smaller than 24 hr. Data are presented as mean \pm STD. *: $p < 0.05$ and ns: $p > 0.05$.

Similar to healthy control, the efferent diameters were significantly larger than afferent diameters after 24 hr ($D_{Af} = 79 \pm 9 \mu\text{m}$ and $D_{Ef} = 157 \pm 19 \mu\text{m}$) and 72 hr ($D_{Af} = 94 \pm 10 \mu\text{m}$ and $D_{Ef} = 151 \pm 11 \mu\text{m}$) of inflammation (Figure 3.3B). Furthermore, when we compared afferent diameters of control and inflamed cases, the difference was not statistically significant. Similarly, the efferent vessels were not significantly different between control and inflamed cases. Although we did not quantify the number of cells leaving the cannulated LNs through efferent vessel, we consistently observed more cells being flushed out of the nodes with 72 hr of inflammation compared to the control and 24 hr post inflammation.

3.3.2. Hydraulic Conductivity of Medulla Determines LN Resistance

The results from computational fluid dynamics model provided the fluid pressure and velocity distributions in our idealized geometry of LN, which we used to calculate the LN resistance. Due to peripheral path being the path of least resistance (our published model suggests that approximately 90% of the fluid goes through peripheral path [114]), we assumed hydraulic conductivity of T cell cortex and B cell follicles would not have a considerable effect on the LN resistance. Therefore, we investigated the role of hydraulic conductivity of medulla and height of the subcapsular sinus. Combining the healthy control experimental measurements with the baseline computational model ($h_{SCS} = 20 \mu\text{m}$) allowed us to estimate the hydraulic conductivity of medulla. We used the intersection of baseline model case (Figure 3.4B, solid dark-grey curve) with experimental measurement (Figure 3.4B, dashed black horizontal line) to determine the best estimate of hydraulic conductivity of medulla to be $K_{\text{medulla}}/K_{\text{T cell cortex}} = 3.5 \times 10^3$. We further looked at the effect of the subcapsular sinus height. By keeping the baseline hydraulic conductivity of medulla

constant ($K_{\text{medulla}}/K_{\text{T cell cortex}} = 3.5 \times 10^3$), decreasing h_{SCS} to 10 μm only doubled the resistance (Figure 3.4B, moving vertically from dark grey curve to black curve at $K_{\text{medulla}}/K_{\text{T cell cortex}} = 3.5 \times 10^3$), which was not enough to capture experimentally observed sixfold increase after 24 hr of inflammation (Figure 3.4B). However, decreasing the hydraulic conductivity of medulla less than an order-of-magnitude ($K_{\text{medulla}}/K_{\text{T cell cortex}} = 4.0 \times 10^2$) could capture the sixfold increase in resistance. Hydraulic conductivity of medulla appears to be the key factor in modulating the LN resistance.

3.3.3. Higher LN Resistance Results in Greater Central Flow

Reduced hydraulic conductivity of medulla due to inflammation indeed altered the flow distribution in LN. In the baseline control, 2.9 nL/min of the fluid moved centrally (from subcapsular sinus to B cell follicles and T cell cortex) and is transported to the blood vessels distributed in the T cell cortex. Increased hydraulic conductivity of medulla after 24 hr inflammation increased the central flow to 4.5 nL/min (about 50% increase compared to the healthy control). Higher hydraulic conductivity of medulla increases the resistance of the peripheral path leading to enhanced central flow and antigen exposure to the B cell and T cell zones. In this study, we assumed the size of the LN stays constant during the first 24 hr.

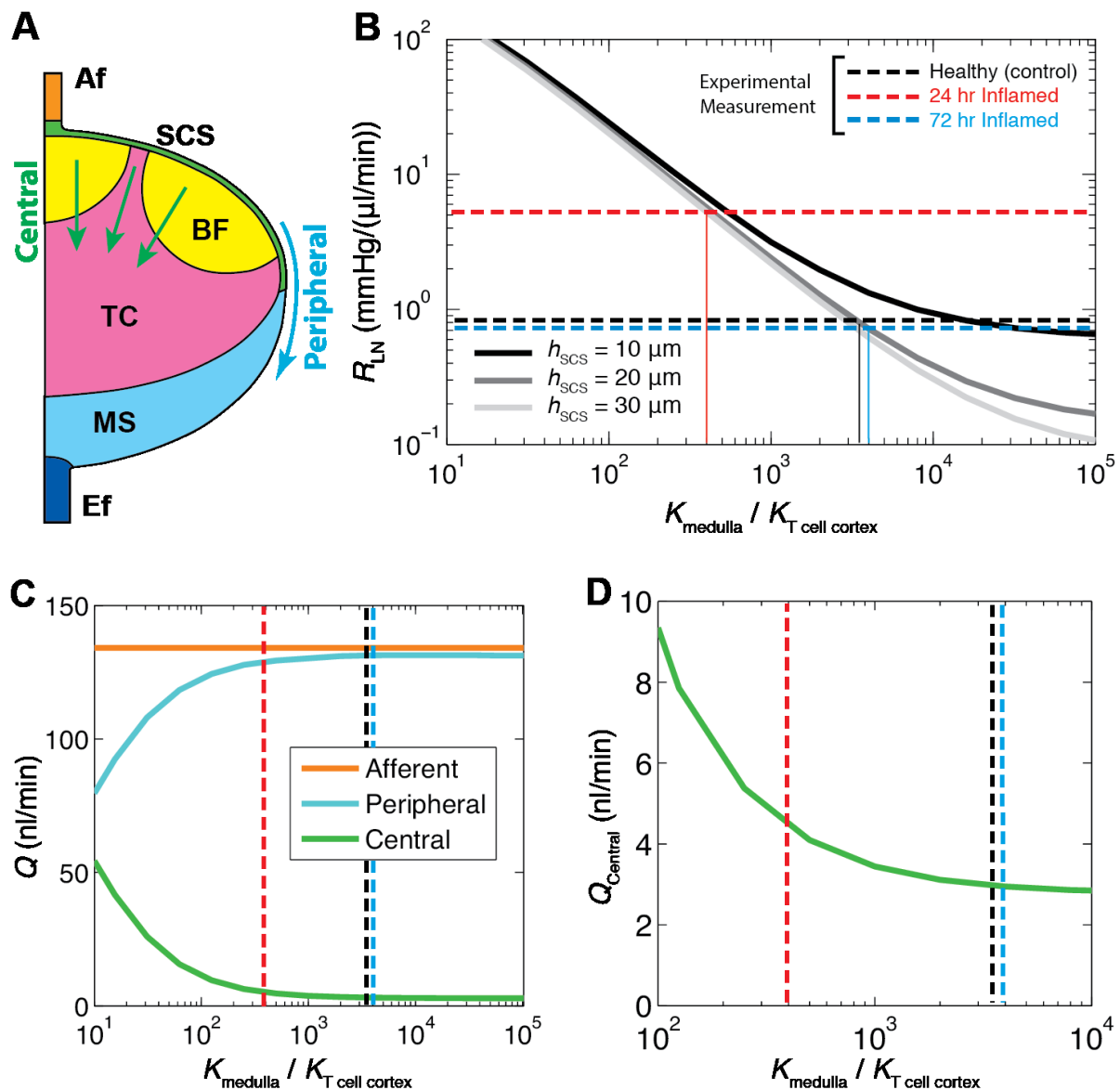


Figure 3.4. Computational model prediction of possible mechanism of resistance increase and resulting flow redistribution. **A**. The idealized geometry of the lymph node shows afferent vessel (Af), subcapsular sinus (SCS), B cell follicles (BF), T cell cortex (TC), medullary sinuses (MS) and efferent vessel (Ef). Central flow is the flow that goes through floor of subcapsular sinus to B cell follicle and T cell cortex. The rest that goes directly from subcapsular sinus to medulla is called peripheral flow. **B**. Overlay of computational model (solid thick lines) with experimentally measured resistance (horizontal dashed lines) for different heights of subcapsular sinus (10 to 30 μm). The solid vertical lines show the intersection of baseline model (20 μm height) with experimental lines. **C**. An order-of-magnitude decrease in hydraulic conductivity of medulla resulted in 50% increase in central flow. **D**. A zoomed-in view of the Panel **C** better illustrates the 50% increase in central flow.

3.4. Discussion

The aim of this study was to measure the resistance of mouse popliteal LNs to understand antigen transport, immune cell trafficking and subsequent development of adaptive immunity [6, 19, 78, 175]. We developed a technique to isolate and cannulate mouse popliteal LN on glass micropipettes and utilized a custom-built pressure and flow measurement apparatus to measure the hydraulic resistance of the LN. Measuring mouse popliteal LN resistance for the first time allowed us to provide insight into how inflammation affects the fluid transport in the LN. The supplementation of experimental measurements with computational model determined the best estimate for hydraulic conductivity of medulla that is on its own impossible to measure experimentally in mouse popliteal LNs due to the small size (popliteal LN is ~1 mm in diameter). The model additionally predicted that hydraulic conductivity of the medulla is the main determinant of LN resistance, and pointed it as the leading candidate for the LN resistance increase after 24 hr of inflammation.

The experimental measurement of popliteal LN resistance in this study is the first of its kind in mice. Due to the small diameter, cannulation of the mouse lymphatic vessels has been challenging. The LN resistance have been measured previously in rabbits (popliteal LN [141]) and dogs (popliteal [166], iliac [165], submandibular [166], mediastinal [166] and periportal [166] LN). Larger size of the afferent and efferent lymphatic vessels has helped with the success of those attempts on larger animals. However, with the advancement of genetic manipulation experiments in mice models for investigating immune response under infection and inflammation, the need for better understanding of the fluid flow properties of mouse LN has increased. The resistance of an organ to fluid flow is a property that depends

on the size of the organ; thereby the resistances from different animal models are not readily comparable (Table 3.1). We have plotted the resistance of the LN versus the body mass of the animal to inspect the scaling of this property (Figure 3.5). Although the power law scaling ($R = a \times M^b$ where R is resistance, $a = 0.264$ mmHg.kg/(μ l/min) and $b = -0.30$ are constants and M is body mass) with body mass did not correlate well ($R^2 = 0.82$ and RMSE = 0.12 mmHg.kg/(μ l/min)) with the LN resistance, addition of a shift in the body mass ($R = a \times (M+c)^b$ where $a = 2.36$ mmHg.kg/(μ l/min), $b = -1.11$ and $c = 2.58$ kg) could capture the trend very well ($R^2 = 0.98$ and RMSE = 0.04 mmHg.kg/(μ l/min)). We think the reason the scaling law is not capturing the behaviour over the full range is the way LN size versus number of LNs scales with animal body mass. The size of the LN scales with increase in body mass but also the total number of the LNs, and more information about the scaling of the total number of the LNs as well as data from more species is needed to better explain LN resistance scaling. Although the LNs of larger species are located in the same general anatomical locations in the body (i.e. softer regions such as armpit and groin), they cluster into chains of LNs in those spots. LNs of larger animals appear to have increased number of afferent and efferent vessels instead of just larger vessels. Additionally, the size of the follicles is conserved (few hundreds of microns) that is most likely limited by the diffusion distance, but there are a greater number of follicles in the LNs of larger animals. We speculate the shear stress and ratio of the efferent protein concentration to afferent concentration to stay the same across the species, because these values can mediate cell signalling pathways independent of animal size.

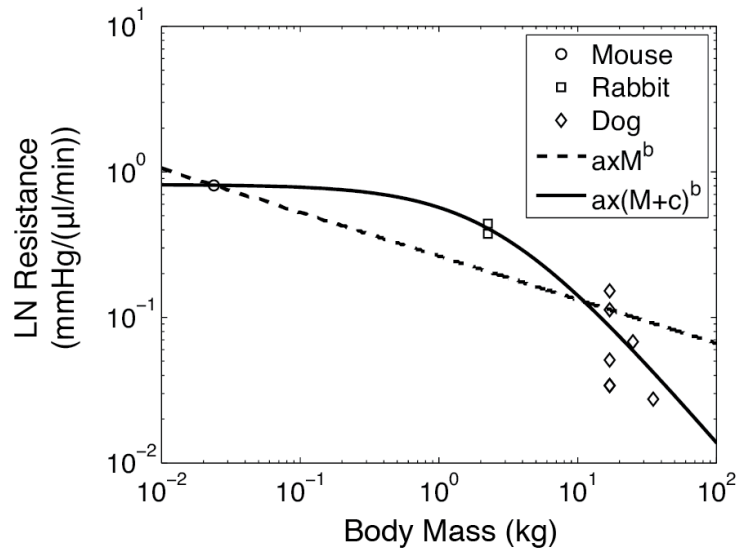


Figure 3.5. Scaling of LN resistance with animal body mass. Measured LN resistances in mouse (circle, this study), rabbit (square), and dogs (diamond) are plotted against the average animal body mass used in the studies (Table 3.1). The power law (dashed line) and shifted power law (solid line) demonstrate how LN resistance correlates with body mass.

The experimental measurements showed an increase in LN resistance at 24 hr, which computational model predicted to be a result of reduced hydraulic conductivity of medulla. Förster and colleagues measured the height of the SCS, and showed it decreases from 14 μm to 11 μm after inflammation (unpublished data), which supports our choices of SCS height for normal and inflamed LN geometries. The model suggests that even greater change in h_{SCS} (20 μm to 10 μm) is not able to increase the resistance sixfold. Furthermore, The prediction of the model regarding decreased hydraulic conductivity of medulla is plausible based on our understanding of the initial steps in immune response. Upon inflammation, the cytokine signals as well as activated DC migration to the draining LN leads to naïve T cell activation. The activated T cells subsequently internalize S1PR1 that is critical for lymphocyte egress [143]. This process is shown to be mediated by CD69 on T cell surface and is thought to be one of the main regulators of LN size and cellularity [12]. Moreover, activated T cells start dividing, which intensifies the increased overall

number of T cells in the LN [158]. We hypothesize that increased number of T cells in the LN pushes the paracortex into the medullary sinuses and partially blocks the path of least resistance leading to the reduced hydraulic conductivity of medulla. However, due to the small height of the SCS and the assumption that it has weaker structure compared to the medulla, swelling of the cortex and paracortex could lead to collapsing of the SCS resulting in increased overall LN resistance. This contradicts experimental measurements of SCS height in WT (14 μm) and inflamed (11 μm) LNs by in the unpublished work of Förster and colleagues. Our model demonstrated that this local increase in the resistance of the medulla enhanced the fluid flow to the cortex of the LN, which carries soluble antigen, chemokine and cytokine signal entered the LN through afferent vessel. The lowered resistance after 72 hr of inflammation could be resulted from a combination of two factors: 1) increase in the hydraulic conductivity of medulla, and 2) increase in the size of the LN, but the change in the size of the LN is not studied here.

LN resistance after 24 hr of inflammation exhibited a nonlinear response in pressure differences higher than approximately 6 mmHg, which results in an afferent transmural pressure of ~ 8.2 mmHg (pressure difference + efferent reservoir pressure). The resistance appeared to decrease in higher pressures compared to the lower ones. We speculate that higher pressures could significantly deform the LN capsule and sinuses resulting in the larger pore sizes and as a result a lower resistance. Due to the dependency of LN-specific pressure difference on the resistance of the sample, only the 24 hr inflamed LNs were subjected to the pressure differences higher than 6 mmHg. We expect to observe similar behaviour in the control and 72 hr inflamed samples, if the total pressures were to increase sufficiently high. Additionally, The variance in the measured LN resistance was

greater in the healthy control and 24 hr inflammation compared to the 72 hr inflamed case. This can be caused by the variations in the basal levels of inflammation in the healthy animals due to cleanness of cages and natural events in the animal housing. That means the healthy control animals might have had low levels of inflammation and the cases of 24 hr each were already at different stages of inflammation at the time of injection leading to wide variations at 24 hr time point. For the 72 hr inflammation cases, they were all inflamed for at least 72 hr, making them a more uniform sample population.

Measurement of whole LN resistance provides us with an estimate of medulla hydraulic conductivity that is impossible to measure due to size restrictions. This technique was superior to our previous estimations based on physiologic range of pressures in the LN [114]. Our estimation though has a limitation based on our assumption that the popliteal LN is well represented by the idealized geometry constructed for this study. An image-based geometry instead of the idealized geometry can certainly increase our confidence in the results of this estimation. Additionally, we used the same idealized geometry to compare the resistance of the healthy control with 24 hr post inflammation. It is shown that the size of the LN increases after inflammation [11, 73], however the accurate regional changes (e.g. T cell cortex versus medulla) after 24 hr of combination treatment with LPS and Poly I:C is not measured to the best of our knowledge. Quantification of size and regional LN swelling by two-photon microscopy of optically cleared LNs can provide valuable information on the details of inflammation-induced LN remodelling. Another limitation of the model is the paucity of the information on the afferent flow boundary condition after inflammation. Inflammation is shown to dilate lymphatic vessels through iNOS-mediated pathways [176, 177], and impair contractile function of collecting lymphatic

vessels [178, 179]. These two consequences have opposite effects on the afferent lymph flow: dilated vessels lead to increased cross-sectional area and higher flow, but impaired contractile function reduces the afferent flow. It is still unclear how the lymph flow to the LN changes during the time course of inflammation.

In summary, this study aims to combine experimental measurement of mouse popliteal LN resistance with the computational model of fluid flow in the LN to examine the main parameters involved in modulating LN resistance especially during inflammation. First our experiments showed that the LN resistance dynamically increases in 24 hr before reducing back down in 72 hr. Subsequently the model indicated that this increase in resistance is mainly due to the reduced hydraulic conductivity in medulla, which resulted in enhanced antigen exposure to the LN paracortex.

CHAPTER 4

DEVELOPMENT OF A COMPUTATIONAL MODEL FOR TRANSPORT OF CHEMOKINES AND FORMATION OF GRADIENTS IN LYMPH NODE

4.1. Introduction

Lymph nodes (LNs) are essential secondary lymphoid organs for immune surveillance of peripheral tissue. Antigen presenting cells (APC) such as dendritic cells (DCs) and soluble antigen are transported via lymph through initial lymphatics and contracting collecting lymphatic vessels from tissues to the draining LNs [65, 71, 147]. The interactions of APCs with lymphocytes in the LN depend on their coordinated migration that controls the quality and quantity of the immune response [14-16]. Chemokines are recognised as the main regulator of immune cell migration [180]. Inflammatory chemokines recruit the leukocytes to the site of inflammation, whereas homeostatic chemokines are indispensable for haematopoiesis and immune cell trafficking in lymphoid organs such as LNs [83, 84]. CCR7 and its exclusive ligands, CCL19 and CCL21 have been established as the key homeostatic chemokine axis for T cell and DC homing to the LN [14, 16, 99, 180].

CCR7 is a G protein coupled receptor (GPCR) that is expressed on naïve B cells and T cells [85, 96], regulatory T cells [97], central memory T cells [85], and semi-mature and mature DCs [98] in the lymph node [99, 100]. Furthermore, CCR7⁺ cancer cells have shown enhanced metastasis to lymphatic vessels through autologous chemotaxis [49]. In contrast to CCL21, CCL19 binding to CCR7 induces receptor phosphorylation and β -arrestin recruitment leading to desensitization and internalization of the receptor-ligand complex [181, 182]. Furthermore, CCR7⁺ cells exhibit directed migration up the gradient of CCL19 and CCL21 concentrations *in vitro* [95, 183].

Immobilized CCL21 induces adhesion of DCs through activation of β 2 integrin [95] and facilitates lymphocyte and DC homing to LN [184]. Although CCL19 and

CCL21 have similarities in their CCR7 binding domain [86, 185, 186], CCL21 has an extended 34-residue C-terminus that binds glycosaminoglycans (GAG) [90]. Indeed, Hirose et al. [91] showed that a truncated version of CCL21 without the last 32 residues failed to bind to GAGs. CCL21 exhibits strong binding to GAGs (such as chondroitin sulphate, heparin and heparan sulphate) [90, 92, 93], and Collagen IV [94], whereas CCL19 does not bind to any measureable degree to extracellular matrix (ECM) [90, 92-94]. Imaging the gradients of CCL19 and CCL21 facilitates the understanding of the gradient-directed migration of immune cells. However, immunostaining for CCL21 and CCL19 in the fixed and permeabilized tissue mostly stains the intracellular chemokine molecules in the Golgi, but not the chemokines in the extracellular space [87]. Imaging the extracellular chemokine concentration fields that are responsible for APC migration is challenging, both because of the low concentrations and also because wash out during the staining process often removes the unbound chemokines. Weber et al. [87] were able to exclusively visualize the extracellular CCL21 by staining the unfixed nonpermeabilized sections of mice ear [87]. The relatively low equilibrium dissociation constant of CCL21 binding to ECM (often reported to be less than 5 nM) allows for higher CCL21 concentrations to bind to tissues [49, 90, 94] and provides the opportunity to visualize the chemokine gradient in tissue with higher concentration of CCL21 binding sites.

Ulvmar et al. [19] used the same technique to investigate the CCL21 gradients in mice popliteal LNs [19]. Their study revealed a CCL21 gradient in the interfollicular region of the LN and demonstrated that this gradient was abrogated in atypical chemokine receptor (ACKR)4-deficient mice [19]. Staining indicated that ACKR4 is expressed by lymphatic endothelial cells (LECs) on the ceiling of the

subcapsular sinus and not the ones on the floor [19]. Moreover, DCs injected in the upstream afferent vessel showed diminished entry to the LN paracortex through the interfollicular region in the ACKR4 knock out (KO) mice compared to the WT [19], which was in accordance with previous reports [187]. Therefore, it was hypothesized that the ACKR4 on the ceiling of the subcapsular sinus locally scavenges CCL19 and CCL21 to stabilize the gradient. ACKR4 is also a G protein coupled receptor that binds to CCL19, CCL21 and CCL25. But it fails to initiate the downstream signalling pathway [88]. K_D for ACKR4 binding to CCL19 is 4.5 nM, i.e. very similar to that of CCR7 (~5 nM) [101]. ACKR4 is rapidly internalized upon CCL19 binding and the scavenging rate of six to seven CCL19 molecules per hour per starting ACKR4 surface molecule [101]. In inflamed skin, ACKR4 is shown to be essential for CCL19 and CCL21 scavenging to facilitate APC egress [102].

Presumably, LECs in the collecting lymphatic vessels express ACKR4, and we assume for the moment that these would also be knocked out in the above experiments (although this was not measured). It is unclear whether it is the LN ACKR4 or the afferent vessel ACKR4 that are crucial for the CCL21 gradient formation in the interfollicular zone. The experiments are limited in what they can reveal, and the conclusions about gradients were made without direct proof because of the presence of other confounding factors such as flow and potential differences in incoming concentrations. The need for more control over the systematic manipulation of the CCL19/CCL21 axis motivated us to build a computational model to identify the important parameters in maintenance of these gradients in the LN.

The few mathematical models that have been developed to study chemokine dynamics range from receptor-ligand models to describe the individual interactions of ligand receptors, to continuum reaction-diffusion models to describe molecular

transport. Lin and Butcher developed a one-dimensional model of ligand receptor accounting for receptor desensitization and internalization and showed that desensitization is essential for cellular navigation in competing chemokine gradients [188]. To study the gradients of CCL19 and CCL21 in three-dimensional collagen gels surrounding a 20 μm alginate spheroid loaded with the chemokines, Wang and Irvine utilized reaction-diffusion equations to build a computational model [189]. The combination of model with experiments revealed that there exists a threshold of ~ 10 receptor occupancy difference between the leading and trailing edge of the cells to exhibit directed migration [189]. Additionally, Bocharov et al. [112] utilized a similar reaction-diffusion model to determine the distribution of interferon- α in the LN [112].

This study aims to provide further insight into LN chemokine transport, and in particular the role of ACKR4 in establishing the interfollicular chemokine gradient. A full understanding of this complex system is difficult to attain via the experimental methods described above because of many inherent confounding factors that exist *in vivo*. We have therefore built a three-dimensional computational model of CCL19 and CCL21 transport in LN that allows control of the various factors in an *in silico* setting. The model includes advection, diffusion, binding to the ECM, receptor binding to CCR7, ACKR4 scavenging on the capsule ceiling and transport to the blood vessels with the aim of identifying the physical and biochemical parameters that most strongly determine the shape of the gradient.

4.2. Methods

4.2.1. Modelling LN Fluid Transport

The flow of lymph through the LN is modelled based on our previously published work [114] and was explained in extent in Chapter II. Briefly, we constructed an idealized 3D geometry of a LN based on the general features of a mouse popliteal LN, including an afferent vessel, subcapsular sinus, B cell follicles, T cell cortex, medulla and an efferent vessel. Computer-aided engineering software ANSYS, Inc. (Pennsylvania, United States) was used to generate a computational mesh and solve the equations of fluid flow. Wall shear stress along the subcapsular sinus was used as the criterion for mesh refinement (normalized root mean squared error less than 2.6% for a grid with 420,000 elements compared to the one with 680,000 elements). The coarser mesh was used for the rest of the study. The Navier-Stokes equations were used to describe flow in the fluidic regions (afferent vessel, subcapsular sinus and efferent vessel), and Darcy's law with Brinkman's term was used in the porous regions (B cell follicles, T cell cortex, and medulla). The fluid exchange between blood vessels and lymphatic compartments was modelled using Starling's equation [114]. All the fluid flow parameters are the same as our previously published work [114].

4.2.2. Chemokine Transport

Diffusion, advection and reaction of unbound CCL21 (CCL21u) and CCL19 are governed by the following equations:

$$\frac{\partial c_i}{\partial t} = \nabla \cdot (D_{i,\text{eff}} \nabla c_i) - (\mathbf{u} \cdot \nabla) c_i - J_{i,\text{BV}} + \Pi_i + R_{i,\text{CCR7}} + R_{i,\text{ECM}} \quad (4.1)$$

where c_i denotes CCL21u or CCL19 concentration (assumed to be both space and time dependent), t is time, $D_{i,\text{eff}}$ is effective diffusion coefficient of respective chemokine in each region, \mathbf{u} is fluid velocity vector, $J_{i,\text{BV}}$ is exchange of chemokine with blood vessels in the LN, Π_i is chemokine production, $R_{i,\text{CCR7}}$ represents CCR7 binding dynamics and $R_{i,\text{ECM}}$ represents ECM binding (Figure 4.1). An additional reaction equation assumed to govern the bound CCL21 (CCL21b) dynamics in the B cell follicle, T cell cortex, medulla and subcapsular sinus.

$$\frac{\partial c_{\text{CCL21b}}}{\partial t} = R_{\text{CCL21b,CCR7}} - R_{\text{CCL21b,ECM}} \quad (4.2)$$

Overall in addition to the equations of fluid flow, the general form of chemokine dynamics consisted of two partial differential equations (PDEs) and six ordinary differential equations (ODEs) in the three-dimensional domains. On the capsule, four additional ODEs were solved to calculate a variable flux for CCL19 and CCL21u based on the ACKR4 dynamics explained in detail in section 4.2.5. Equations were solved in the steady state form (without the transient term on the left hand side) and the solution was initialized with zero concentrations for all the variables. Chemokine concentration assumed to be constant and equal to zero for all the variables (unless indicated) at the inlet of the afferent vessel and the outlet of the efferent vessel.

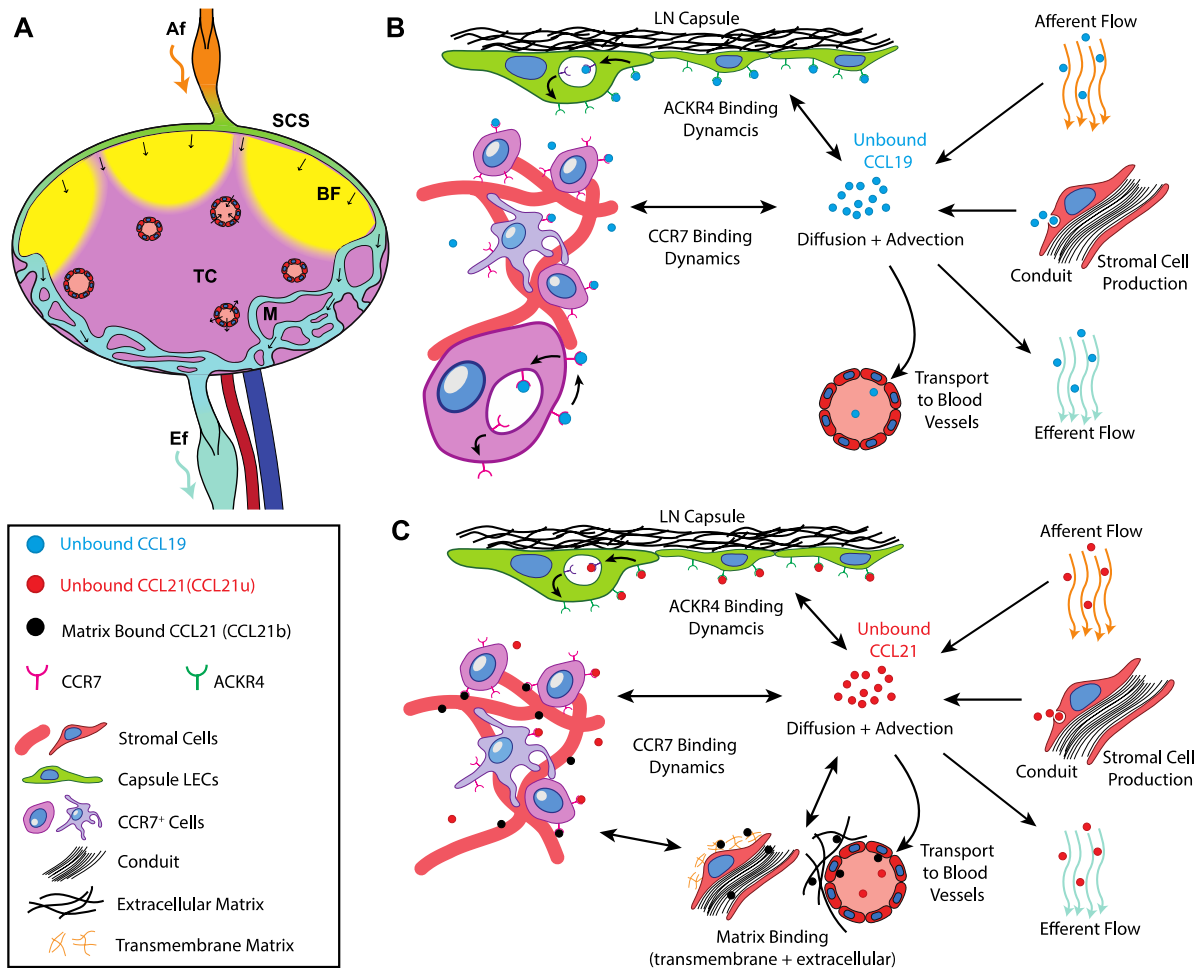


Figure 4.1. Schematic of the LN with details of CCL19 and CCL21 interactions. **A.** Schematic showing fluid entry into the LN subcapsular sinus (SCS) through afferent vessel (Af). Lymph can then percolate into the LN paracortex to B cell follicles (BF) and T cell cortex (TC) where it can be exchanged by blood vessels; otherwise it flows to medulla and is transported out of the LN via efferent vessel (Ef). To facilitate the understanding of the model components, the specific interactions for CCL19 (**B**) and CCL21 (**C**) are illustrated here. Each arrow shows a reaction or transport term in the model.

4.2.3. CCL21 Binding to Matrix

The process of CCL21 binding to and unbinding from ECM was modelled with the following first order reaction kinetics:

$$R_{\text{CCL21u,ECM}} = -k_1(E - c_{\text{CCL21b}})c_{\text{CCL21u}} + k_2c_{\text{CCL21b}} \quad (4.3)$$

$$R_{CCL21b,ECM} = +k_1(E - c_{CCL21b})c_{CCL21u} - k_2c_{CCL21b} \quad (4.4)$$

where the binding rate constants k_1 and k_2 were measured by Shields et al. [49] for CCL21 binding to perlecan and found to be $0.000093 \text{ nM}^{-1}\text{s}^{-1}$ and 0.00012 s^{-1} , respectively [49]. The maximum number of binding sites associated with each cell was assumed to be 1,000,000, which is similar to matrigel containing 1% perlecan [49]. The average matrix binding site concentration (E) in each region of the LN was calculated by solving Equation 4.20 as explained in detail in Parameter Estimation (Section 4.2.7).

4.2.4. CCR7 Binding Dynamics

CCR7 binding to its ligands (CCL19 and CCL21) induces activation of G protein and calcium mobilization leading to survival signal and cell motility [99, 182, 190, 191]. CCL19 is shown to desensitize and internalize the receptor considerably more than CCL21 [181, 192-194]. We have employed a simplified version of the Butcher and Lin model developed for CCL19 and CCR7 binding dynamics [188] as given below:

$$\frac{dc_{CCR7}}{dt} = R_{CCL21u,CCR7} + R_{CCL21b,CCR7} + R_{CCL19,CCR7} + \lambda_{up}c_{CCL19-CCR7_{int}} \quad (4.5)$$

$$\frac{dc_{CCL19-CCR7}}{dt} = -R_{CCL19,CCR7} - \lambda_{des}c_{CCL19-CCR7} \quad (4.6)$$

$$\frac{dc_{CCL19-CCR7_{des}}}{dt} = \lambda_{des}c_{CCL19-CCR7} - \lambda_{int}c_{CCL19-CCR7_{des}} \quad (4.7)$$

where

$$R_{CCL19,CCR7} = -\lambda_{on}c_{CCL19}c_{CCR7} + \lambda_{off}c_{CCL19-CCR7} \quad (4.8)$$

$$R_{\text{CCL21u,CCR7}} = -\lambda_{\text{on}}c_{\text{CCL21u}}c_{\text{CCR7}} + \lambda_{\text{off}}c_{\text{CCL21u-CCR7}} \quad (4.9)$$

$$R_{\text{CCL21b,CCR7}} = -\lambda_{\text{on}}c_{\text{CCL21b}}c_{\text{CCR7}} + \lambda_{\text{off}}c_{\text{CCL21b-CCR7}} \quad (4.10)$$

Furthermore, we have assumed CCL21u or CCL21b can bind to CCR7 to start the downstream signalling but it does not desensitize and internalize the receptor (Figure 4.2A) and thus are modelled by the following equations:

$$\frac{d}{dt}c_{\text{CCL21u-CCR7}} = -R_{\text{CCL21u,CCR7}} \quad (4.11)$$

$$\frac{d}{dt}c_{\text{CCL21b-CCR7}} = -R_{\text{CCL21b-CCR7}} \quad (4.12)$$

Additionally, the total number of CCR7 (in all its different states) per cell was assumed to be constant so that at any point in time

$$C_{\text{CCR7,tot}} = c_{\text{CCR7}} + c_{\text{CCL21u-CCR7}} + c_{\text{CCL21b-CCR7}} + c_{\text{CCL19-CCR7}} + c_{\text{CCL19-CCR7}_{\text{des}}} + c_{\text{CCL19-CCR7}_{\text{int}}} \quad (4.13)$$

The total number of receptors in each computational element is calculated based on the continuum assumption explained in detail in Parameter Estimation (Section 4.2.7) section and CCR7 expression values obtained from ImmGen database (Table 4.2) [100, 195]. CCR7 is discretely located on the cell membrane, however we have made the simplifying assumption that CCR7 in each computational element is uniformly distributed and we can think of it as concentration. The model assumes that forward ($\lambda_{\text{on}} = 0.001 \text{ nM}^{-1}\text{s}^{-1}$) and backwards ($\lambda_{\text{off}} = 0.005 \text{ s}^{-1}$) binding rates are similar for CCL21 and CCL19 and are calculated based on the experimental data reporting the dissociation constant of these interactions [86, 101, 188-190]. The rate constants for desensitization ($\lambda_{\text{des}} = 0.003 \text{ s}^{-1}$), internalization ($\lambda_{\text{int}} = 0.0005 \text{ s}^{-1}$) and up-regulation ($\lambda_{\text{up}} = 0.000375 \text{ s}^{-1}$) of CCL19-CCR7 were calculated from curve-fits of

experimental data by Wang et al. [188, 189]. The maximum number of CCR7 molecules per cell is estimated to be 30,000 in the baseline case [101].

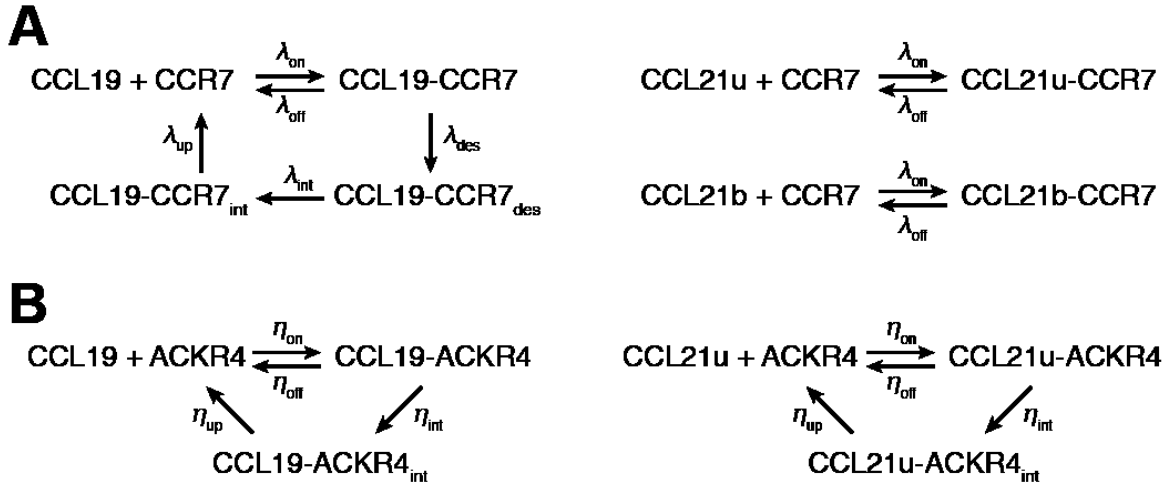


Figure 4.2. Reaction equations for CCR7 and ACKR4 dynamics. **A**. After CCR7 binding to CCL19, it is assumed that CCR7 is desensitized and internalized before resurfacing. CCL19 is assumed to degrade during this process (**A**, left side reaction). CCL21 interactions with CCR7 are modelled using receptor-ligand models without downstream signalling (**A**, right side reactions). **B**. When CCL19 and CCL21u reach the ceiling of the capsule where the ACKR4⁺ LECs are located, they bind the receptor and internalize it. When the receptor resurfaces, the ligand degrades.

4.2.5. ACKR4-mediated Chemokine Degradation

LECs on the LN capsule are shown to express ACKR4 [19]. From the number of LECs we estimated in SCS, half of them are assumed to be on the ceiling, which leads to an average cell diameter of ~25 μm . The same LEC density was used in the medulla on the capsule. A receptor internalization model was adopted to describe the ACKR4 dynamics and scavenging of CCL19 and CCL21u (Figure 4.2B) as given below:

$$\frac{d c_{\text{CCL19-ACKR4}}}{dt} = \eta_{\text{on}} c_{\text{CCL19}} c_{\text{ACKR4}} - \eta_{\text{off}} c_{\text{CCL19-ACKR4}} - \eta_{\text{int}} c_{\text{CCL19-ACKR4}} \quad (4.14)$$

$$\frac{\square c_{\text{CCL19-ACKR4}_{\text{int}}}}{\square t} = \eta_{\text{int}} c_{\text{CCL19-ACKR4}} - \eta_{\text{up}} c_{\text{CCL19-ACKR4}_{\text{int}}} \quad (4.15)$$

$$\frac{\square c_{\text{CCL21u-ACKR4}}}{\square t} = \eta_{\text{on}} c_{\text{CCL21u}} c_{\text{ACKR4}} - \eta_{\text{off}} c_{\text{CCL21u-ACKR4}} - \eta_{\text{int}} c_{\text{CCL21u-ACKR4}} \quad (4.16)$$

$$\frac{\square c_{\text{CCL21u-ACKR4}_{\text{int}}}}{\square t} = \eta_{\text{int}} c_{\text{CCL21u-ACKR4}} - \eta_{\text{up}} c_{\text{CCL21u-ACKR4}_{\text{int}}} \quad (4.17)$$

Moreover, the total number of ACKR4 molecules (in all its different states) per LEC was assumed to be constant so that at any point in time

$$C_{\text{ACKR4,tot}} = c_{\text{ACKR4}} + c_{\text{CCL19-ACKR4}} + c_{\text{CCL19-ACKR4}_{\text{int}}} + c_{\text{CCL21u-ACKR4}} + c_{\text{CCL21u-ACKR4}_{\text{int}}}, \quad (4.18)$$

which was estimated to be 30,000 in baseline case [101]. These equations were solved at the capsule boundary to calculate the scavenging flux for CCL19 and CCL21u. All the other molecules were assumed to have zero flux through the capsule. Our previous work demonstrated that HEK293 cells that express ACKR4 internalize radiolabeled CCL19 after binding and these cells scavenged ~65% of total CCL19 during a 12 hr incubation (1:100 receptor to ligand ratio) [101]. Based on our observations of rapid internalization of ACKR4 receptors after binding to CCL19, we assumed that resurfacing of the receptor is the limiting factor and then set the rest of the reaction parameters of the model to have similar scavenging rates ($\eta_{\text{in}} = 1.0 \text{ s}^{-1}$ and $\eta_{\text{up}} = 0.002 \text{ s}^{-1}$). Additionally we measured the dissociation constant to be 4.5 nM and set the on and off rates accordingly ($\eta_{\text{on}} = 0.5 \text{ nM}^{-1}\text{s}^{-1}$ and $\eta_{\text{off}} = 2.25 \text{ s}^{-1}$).

4.2.6. Chemokine Transport to Blood Vessels

At physiologic conditions, the concentration of CCL19 and CCL21 in plasma is very low [196, 197]. Moreover, *in vivo* studies have demonstrated that subcutaneously injected chemokines appear rapidly in the blood vessels of the LNs [157]. The chemokine transport to blood vessels can happen through two mechanisms: convection from fluid exchange and diffusion due to concentration difference indicated by the first and second terms respectively in the equation below

$$J_{i,BV} = J_v (1 - \sigma_f) \left(\frac{c_i + C_{i,BV}}{2} \right) + P_u A (c_i - C_{i,BV}) \quad , \quad (4.19)$$

where J_v is the flow exchanged by blood vessels as calculated by Starling's equation, c_i denotes CCL21u or CCL19 concentration outside of the blood vessels in LN, σ_f is a filtration reflection coefficient that is close to zero for small molecules [82], $C_{i,BV}$ is CCL19 and CCL21u concentration in blood vessels (that is normally very low; here assumed 0.01 nM [196, 197]), P_u is the average permeability of the chemokine across capillaries and venules, and A is the surface area density of blood vessels in the LN. The fluid is usually transported from the lymphatic compartments to the blood vessels in the LN and the fluid exchange parameters from Starling's equation are the same as in our previous work [114, 124]. Scallan and Huxley measured rat mesenteric venule permeability to albumin to be $5e-7$ cm/s [198]. We have assumed LN blood vessels to have a similar permeability to chemokines.

Table 4.1. Total cell numbers (N_k) and the percentage of cell types ($P_{k,j}$) present in different regions of the LN.

Cell type	percentage of the cells in each region ($P_{k,j}$)				Total cells (N_k)	Reference
	B cell follicle	T cell cortex	SCS	Medulla		
B cell	90	0	0	10	933,000	[19, 151, 199]
T cell	0	90	0	10	1,000,000	[19, 151, 199]
DC	0	100	0	0	68,500	[19, 151, 199]
MΦ	0	0	10	90	120,000	[19]
BEC	0	75	0	25	14,000	[11, 199, 200]
LEC	0	0	10	90	15,000	[200]
FRC	0	100	0	0	28,500	[199, 200]

4.2.7. Parameter Estimation

Because of the complexity that arises from having seven different cells types in multiple regions in the LN, we have made a set of simplifying assumptions that utilizes the gene expression data available from Immunological Genome Project (ImmGen) to greatly reduce the number of free parameters in the model. We have assumed that the cell types are homogenously distributed within each of the regions as shown in Table 4.1 and that the protein levels are proportional to the expression values (EV) obtained from ImmGen [100, 195]. With that we can calculate the parameters of interest using

$$X_i = \sum_k N_k P_{k,j} EV_{X,k} \frac{X^{\max} Vol_i}{N_A Vol_j} \quad (4.20)$$

where N_k is total number of cell type k (B cell, T cell, DC, macrophage, LEC, BEC, FRC) from Table 4.1, index k is summed over cell types for variable X that can be chemokine production (Π_{CCL21} and Π_{CCL19}), CCR7 receptor density ($C_{CCR7,tot}$) and ECM binding site density (E), $P_{k,j}$ is the percentage of the cell type k present in region j (Table 4.1), $EV_{X,k}$ is the value of expression of protein X in cell type k

normalized by maximum EV_X between all the cell types (Table 4.2), X^{\max} is the maximum protein molecules present or produced in the cell type with maximum EV_X , N_A is Avogadro's number, and Vol_i and Vol_j are volumes of computational element i and its corresponding region j .

Table 4.2. Normalized RNA expression of proteins by different cell types of LN from ImmGen database [100, 195].

Cell types	CCL19		CCL21		CCR7		Matrix binding site				Average
	Exp value *	Norm EV †	Exp value	Norm EV	Exp value	Norm EV	‡		§		
							Exp value	Norm EV	Exp value	Norm EV	
B cell	0	0	0	0	1000	0.25	0	0	0	0	0
T cell	0	0	0	0	2000	0.50	0	0	0	0	0
DC	0	0	0	0	4000	1.00	1500	0.35	0	0	0.17
MΦ	0	0	0	0	0	0	0	0	0	0	0
BEC	150	0.02	9200	0.66	0	0	1000	0.23	7000	0.74	0.48
LEC	300	0.03	1500	0.11	0	0	1200	0.27	5400	0.57	0.42
FRC	8800	1.00	14000	1.00	0	0	4300	1.00	9400	1.00	1.00

* Exp value: RNA expression values from ImmGen

† Norm EV: expression value normalized by the maximum

‡ Data from syndecans 1-4 and glypicans 1-6 are summed to calculate the expression value

§ Data from perlecan, agrin, biglycan and collagen IV are summed to calculate the expression value

For example, for the total number of CCR7 molecules in the T cell region, we multiply the total number of T cells (~1,000,000 from Table 4.1) by the percentage of cells in the T cell cortex (0.9 from Table 4.1) to find the total number of T cells in the cortex. We then multiply it with the normalized CCR7 expression value for T cells (0.5 from Table 4.2) and maximum possible CCR7 per cell (30,000 from Section 4.2.4) and divide by Avogadro's number to find the total moles of CCR7 molecules on T cells in T cell cortex. Assuming homogenous distribution, we scale the total moles with the volume of the computational element (Vol_i) with respect to the volume

of the T cell cortex (Vol_j) to find moles of CCR7 in that element. When we sum all the moles of CCR7 from different cell types (B cell, T cell, DC, macrophage, LEC, BEC, FRC) we have an estimate of total moles of CCR7 in that computational element. Using Equation 4.20 and the information in Tables 4.1-3, we estimated the rate of CCL19 production (Figure 4.3B), rate of CCL21 production (Figure 4.3C), CCR7 density (Figure 4.3D) and the ECM binding site density (Figure 4.3E) in each region of the LN.

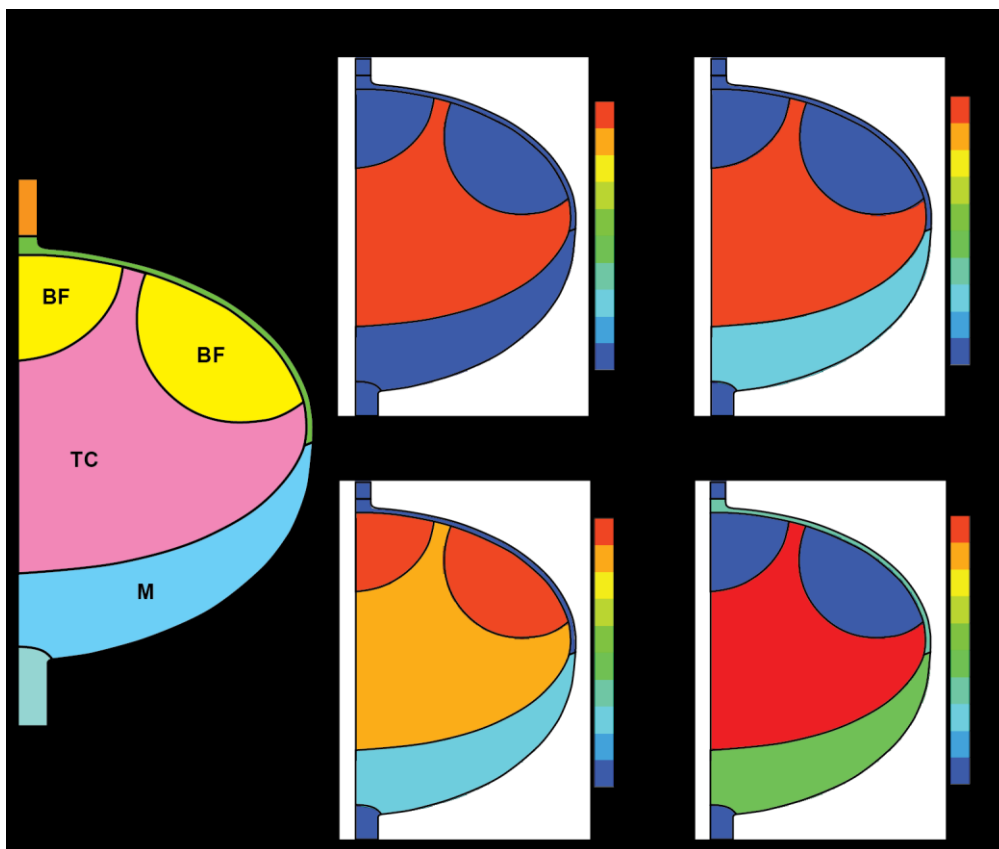


Figure 4.3. LN geometry and distribution of CCL19 and CCL21 productions, as well as CCR7 and matrix binding site densities. **A**. Idealized geometry of the LN for the computational model is marked with the name of the regions. Under the assumption of homogenous distribution of cells in each region, production of CCL19 (**B**), production of CCL21 (**C**), CCR7 concentration (**D**) and matrix binding site concentration (**E**) in LN are calculated by Equations 4.20 and shown here.

4.2.8. Parameter Sensitivity Analysis

Latin hypercube sampling technique was used to investigate the effect of seven parameters that were anticipated to be important for forming the gradients of CCL21 and CCL19. This technique is suitable for producing evenly distributed samples in the parameter range specified and the produced samples better represent the variability in the parameters compared to an ensemble of randomly varied parameters. The input parameters and bounds on their distribution are detailed in Table 4.3. The slope of the gradient was calculated in the T cell zone starting from the floor of the SCS (Figure 4.6A). We quantified the slope of CCL19 (Figure 4.6E) and CCL21b (Figure 4.6G) in the T cell zone, total CCL19 (Figure 4.5F) and CCL21 (Figure 4.6H) in the whole LN, and efferent concentrations of CCL19 and CCL21 from simulations with 100 different input parameter combinations. Volume integral of the concentration over LN volume was used to calculate total CCL19 and CCL21 (= total CCL21u + total CCL21b). Partial rank correlation coefficients (PRCCs) were calculated to identify the positive and negative correlations between the main input parameters and the outputs of the model [201, 202]. A PRCC of +1 represents perfect positive correlation and -1 depicts perfect negative correlation. Student *t*-test was used to determine the significance of the PRCCs. MATLAB R2013a (MathWorks) was used for PRCC calculation and statistical analysis.

Table 4.3. Input parameter range for latin hypercube sampling.

Parameter	Unit	Baseline value	Lower bound	Upper bound
$C_{in,CCL19}$	nM	0	0	5
$C_{in,CCL21u}$	nM	0	0	5
$\Pi_{CCL19,max}$	#/cell-s	4.11	0.8	20.6
$\Pi_{CCL21u,max}$	#/cell-s	6.54	1.3	32.7
$NT_{CCR7,max}$	#/cell	30000	0	60000
$NT_{ACKR4,max}$	#/cell	30000	0	60000
D_{eff}/D_0	-	0.10	0.025	0.4

NT is maximum total number of receptors per cell

4.2.9. Concentration Difference Calculation Across Cells

The concentration difference along the direction of interest in the interfollicular region (Figure 4.4A) was calculated by subtracting the concentration at a location a cell radius closer to the capsule from the concentration at a location a cell radius deeper in the LN for three different cell diameters of 9 μm , 18 μm , and 36 μm . These sizes were chosen to cover the range of cell size from small lymphocytes to larger myeloid cells such as DCs. The baseline gradients (Figure 4.4E-F) were resampled with 4.5 μm steps in the T cell zone, low-pass filtered and the differences were calculated at each step for CCL19, CCL21u and CCL21b.

4.3. Results

4.3.1. Chemokine Gradient Formation under Baseline Conditions

Simulations of the steady state concentration distributions of CCL19 and CCL21 (both in unbound and bound forms) were found to be higher near the centre of the T cell cortex (Figure 4.4B-D). The maximum CCL19 concentration was 0.87 nM. CCL21u exhibited a maximum concentration of 5.2 nM, and CCL21b a maximum of 306 nM. Lower concentrations of CCL21b (0.42 nM) and CCL19 (0.014 nM) were observed in the B cell follicles compared to the T cell cortex. This was in contrast to the CCL21u contours that were much less affected by B cell follicles (Figure 4.4B-D). Gradients in all species were observed in the interfollicular region, with near zero concentrations at the border with the SCS, and higher concentrations deeper in the T cell cortex (Figure 4.4E-F). The gradient of CCL19 and CCL21u concentration profiles were fairly constant (0.003 and 0.018 nM/ μm respectively) in the interfollicular region and both profiles flattened deeper in the cortex (Figure 4.4F).

Furthermore, the CCL21b gradient was greatest at the border with the SCS (3.7 nM/ μ m) and dropped an order-of-magnitude to 0.44 nM/ μ m at a depth of 200 μ m into the cortex (Figure 4.4G). Overall, CCL21b had a steeper interfollicular gradient compared to CCL19 and CCL21u.

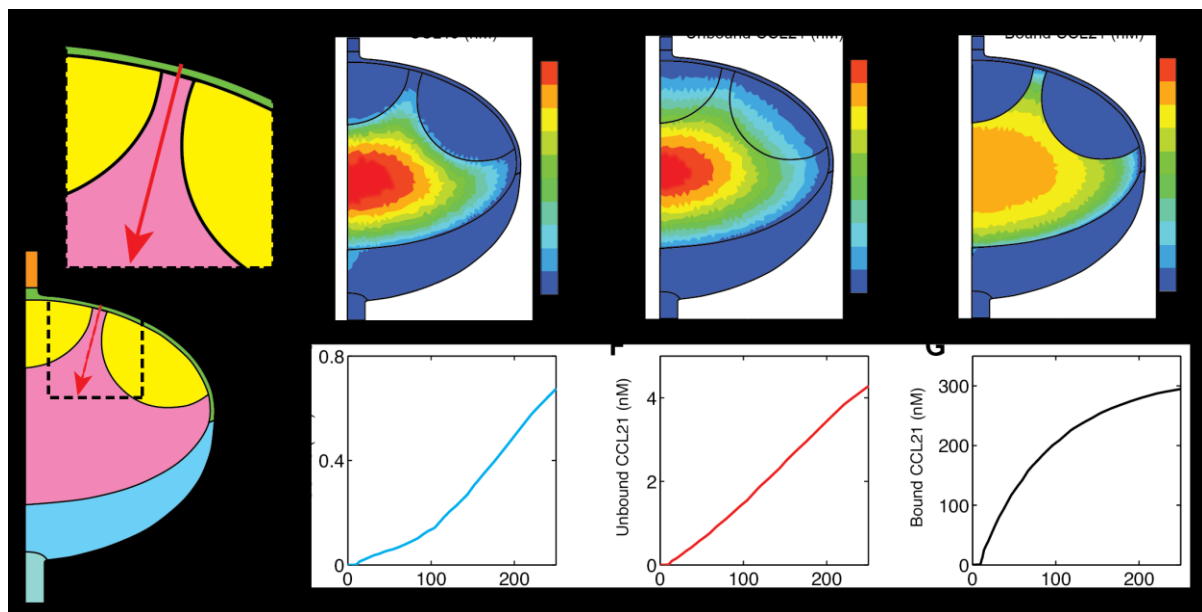


Figure 4.4. CCL19 and CCL21 gradients in the interfollicular regions of the LN. **A**. The LN is modelled with an idealized geometry with one afferent vessel and one efferent vessel. Red arrow shows the line in the interfollicular region along which gradients have been calculated. It starts from the ceiling of the SCS and after passing the sinus (~ 10 μ m height) goes 240 μ m deep into the T cell cortex. Contours of CCL19 (**B**), CCL21u (**C**) and CCL21b (**D**) are shown (all in unites of nM), but note the different scale values. The gradients (**E-G**) are additionally quantified along the red arrow (**A**) for each of the corresponding contours.

Steady state CCR7 density was in the bound form in most parts of the LN except in the B cell follicles where unbound CCR7 appeared to have a gradient towards the SCS (Figure 4.5A). In the T cell cortex, on average 123.8 nM of CCR7 receptors were bound to the CCL21b (94.7% of total CCR7 concentration in T cell cortex) (Figure 4.5C) while an average of 0.7 nM was desensitized with CCL19

(CCL19-CCR7_{des}, Figure 4.5E) and 1.0 nM was internalized (CCL19-CCR7_{int}, Figure 4.5F). The highest concentrations of CC21u-CCR7 (44.2 nM), CCL19-CCR7 (1.4 nM), CCL19-CCR7_{des} (8.4 nM) and CCL19-CCR7_{int} (11.1 nM) were all observed at the B cell-T cell border (Figure 4.5B, D-F).

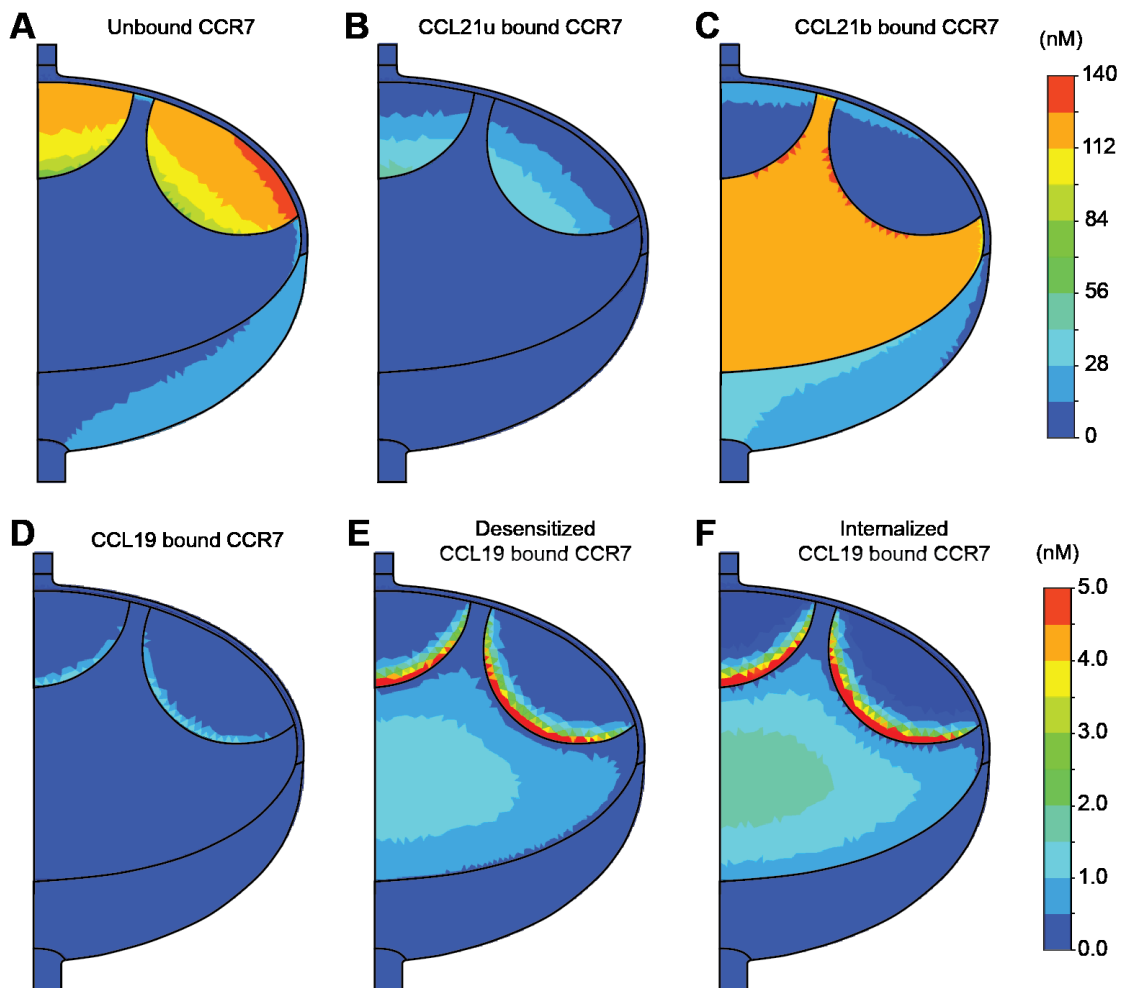


Figure 4.5. Regional variations in the state of CCR7 receptors. The total concentration of CCR7 is assumed to be constant in each region during the simulations, however CCR7 can be in many states depending on the molecule it binds. In addition to the free to bind CCR7 on the cell surface (A), it can be on the cell surface but bound to CCL21u (B), CCL21b (C), or CCL19 (D). CCL19 is shown to desensitize the receptor (E) and subsequently internalize it (F) leading to ligand degradation and receptor resurfacing. Note that for the ease of comparison, all the top row panels have the same colour scale. Similarly the bottom row panels have the same colour scale.

4.3.2. Parameter Sensitivity Analysis

Random variations in the seven parameters (100 different combinations) resulted in a variety of changes in the shapes and sizes of the steady-state chemokine gradients, with some parameters exhibiting dominance over others (Figure 4.6B-D). Although most of the time the gradient of CCL19 was negative, depending on the combinations of the parameters it could change to positive or zero gradient (Figure 4.6B). Often the concentration of CCL19 dropped in the interfollicular region (about first 100 μm) followed by an increase in the concentration afterwards. In contrast, CCL21u gradients were always positive and under the conditions explored here the concentration increased monotonically with depth into the T cell zone (Figure 4.6C). Similarly, CCL21b formed monotonically increasing distributions with positive gradients, although over higher ranges of concentrations compared to CCL21u (Figure 4.6D). In addition to the correlations observable in Figure 4.6E-H, all PRCCs are provided in Table 4.4.

Afferent Concentration (C_{in}). There was a strong correlation between afferent concentration of CCL19 and CCL21 and their corresponding gradients (Figure 4.6E,G). Although CCL19 and CCL21 both correlate negatively with afferent concentration, they had opposite effects on the magnitude of the gradient. Increasing $C_{in,CCL19}$ makes the CCL19 gradient steeper in the negative direction (increasing the magnitude of the slope), whereas increasing $C_{in,CCL21}$ reduces the magnitude of the positive gradient lowering the magnitude of the slope (Figure 4.6E,G). Furthermore, higher afferent concentrations increases the total chemokine mass and efferent concentrations for both CCL19 and CCL21 (Figure 4.6F,H Table 4.4). Importantly, there is a degree of cooperation between the formation of the CCL19 and CCL21 concentration fields. Higher $C_{in,CCL19}$ also increased the total

mass of CCL21 (Table 4.4). The effect is more pronounced when $C_{in,CCL21}$ increases, as it can accumulate in bound form and occupy CCR7 receptors to a greater extent.

Scavenging by ACKR4. The gradients of CCL19 and CCL21b did not correlate with the number of ACKR4 molecules per LEC on the LN capsule LECs. Although not easily distinguishable in the plots (Figure 4.6F,H), correlation analysis showed a negative and weak correlation between ACKR4 receptor numbers and total concentrations of CCL19 and CCL21 (Table 4.4). Moreover, ACKR4 levels negatively correlated with the efferent concentration of CCL19 and CCL21 (Table 4.4).

Scavenging by CCR7. The strong negative correlation of CCL19 slope and total mass is clearly observable in Figure 4.6E-F and is supported by the statistical analysis on the PRCC in Table 4.4. The scavenging of CCL19 by CCR7 also results in the negative correlation between efferent concentration of CCL19 and the CCR7 levels. It is noteworthy that there is no correlation between CCR7 and CCL21-related parameters.

Effective Diffusion Coefficient (D_{eff}). The effective diffusion coefficient plays an important role in reducing the magnitude of the concentration gradients. As a result, increasing D_{eff} makes CCL19 gradient less negative (positive correlation) and also reduces the CCL21 gradient (negative correlation) illustrated in Figure 4.6E,G. At the same time, higher effective diffusivity reduces the total amount of chemokine (Figure 4.6E-F, Table 4.4).

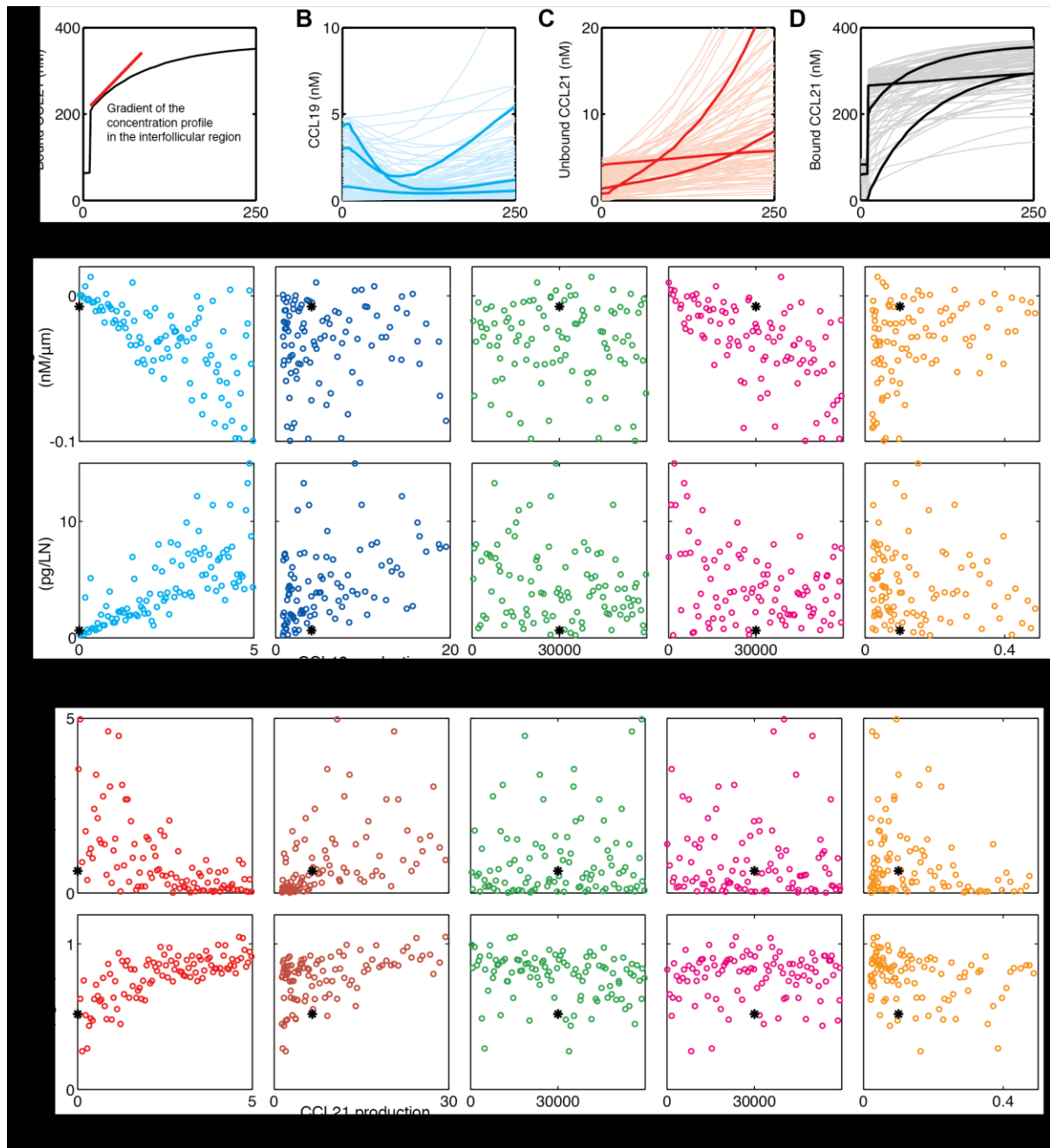


Figure 4.6. Parameter sensitivity analysis. Two main output parameters here are the slope of chemokine gradient in the interfollicular region and the total chemokine mass in a whole LN. **A**. A plot of representative CCL21b concentration profile is overlaid with a red line showing the slope at the entry to the interfollicular region. CCL19 (**B**), CCL21u (**C**) and CCL21b (**D**) concentration profiles are plotted for 100 simulations with more transparent colours. The bolder curves represent sample cases (unrelated to each other) to illustrate the main types of behaviour observed in the simulations. CCL19 gradient (**E**) and total CCL19 mass in LN (**F**) are plotted versus input parameters to visualize the correlations between the inputs and the outputs. Similar data are shown for CCL21b gradient (**G**) and total LN CCL21 mass (CCL21u + CCL21b) (**H**). Asterisk shows the baseline case discussed in more detail in Figures 4.3-4.

Table 4.4. Results of parameter sensitivity analysis are summarized for key model outputs (for CCL19 and CCL21) and significantly correlated input parameters.

PRCC	Output Parameter					
	CCL19 Gradient Slope	CCL21b Gradient Slope	Total CCL19 in LN	Total CCL21 in LN	Efferent CCL19 Concentration	Efferent CCL21 Concentration
$C_{in,CCL19}$	- - -		+ + +	+	+ + +	+ + +
$C_{in,CCL21u}$		- - -	+ + +	+ + +	+ + +	+ + +
$\Pi_{CCL19,max}$	+ + +		+ + +		+ +	+
$\Pi_{CCL21u,max}$		+ + +		+ + +		+ + +
$NT_{CCR7,max}$	- - -		- - -		- - -	
$NT_{ACKR4,max}$			- - -	- - -	- - -	- - -
D_{eff}/D_0	+ +	- - -	- - -	- - -	- - -	

Significant PRCC values are as follows: +/- 0.001<p<0.01, + +/- - 0.0001<p<0.001, + + +/- - - - p<0.0001

NT is maximum total number of receptors per cell

4.3.3. Role of ACKR4 in LN versus Collecting Lymphatic Vessels

Based on the parameter sensitivity analysis on the effect of ACKR4 and C_{in} , we found that the afferent concentration of chemokines is more important than the LN ACKR4 in forming the interfollicular gradients. This can be illustrated by comparison of three different cases: (i) the baseline case (WT) that has ACKR4 scavenging on the capsule ceiling and zero afferent concentrations ($C_{in,CCL19} = C_{in,CCL21} = 0$ nM); (ii) “LN ACKR4 KO” where there is no ACKR4 scavenging and zero afferent concentrations similar to the WT case; (iii) “global ACKR4 KO” case that, in addition to the removal of the ACKR4 scavenging in the LN capsule, has 5 nM afferent concentrations ($C_{in,CCL19} = C_{in,CCL21} = 5$ nM) to simulate the presumed effect of not having the upstream ACKR4 in the collecting vessels and tissues. The respective contours of CCL19, CCL21u and CCL21b for LN ACKR4 KO were very similar to the WT case (Figure 4.4), but they were all very different from the global ACKR4 KO case (Figure 4.7A-C). In the global KO case, the highest concentration of CCL19 was in the SCS and medulla where most of the afferent CCL19 was washing through and the lowest concentrations were in the B cell follicles. This reversed the

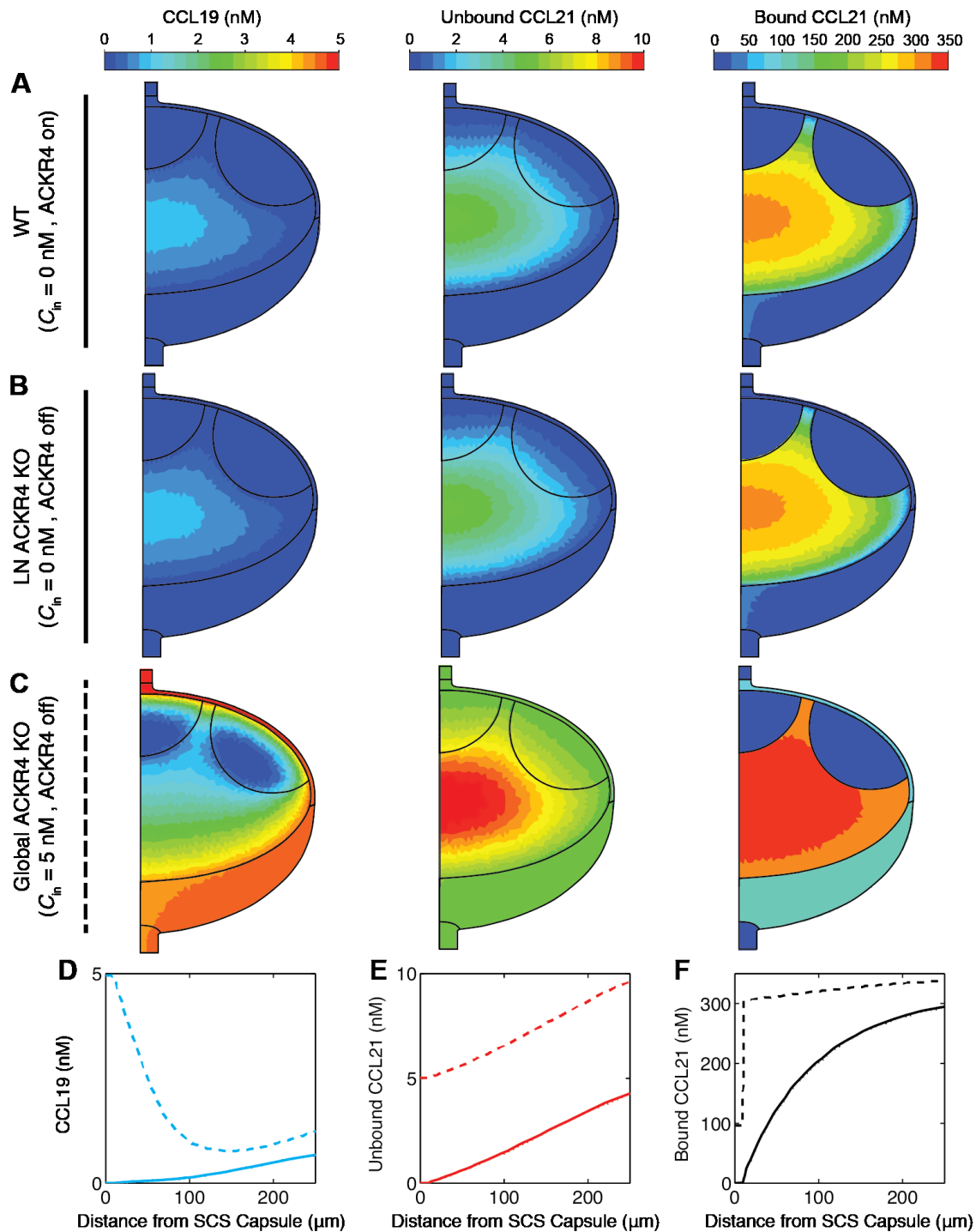


Figure 4.7. LN ACKR4 versus afferent vessel ACKR4 states. Contours and plotted gradients of CCL19 (left column), CCL21u (middle column) and CCL21b (right column) compares WT control (A, solid lines in D-F), LN ACKR4 KO (B, solid lines in D-F) where only ACKR4 is removed from the LN SCS ceiling, and global ACKR4 KO (C, dashed lines in D-F) where in addition to elimination of ACKR4 scavenging boundary condition on the SCS ceiling, the afferent concentration is increased to simulate the production and delivery of chemokines from upstream tissue. Note the WT control and LN ACKR4 lines on top of each other so cannot be distinguished.

direction of the gradient in the interfollicular region from positive to negative (Figure 4.7D). CCL21u maintained a similar concentration profile to WT case; the concentration range, however, was shifted to higher values of concentration (5-10 nM instead of 0-5 nM) compared to the WT case (Figure 4.7E). Furthermore, The CCL21b gradient became almost flat in the interfollicular region (Figure 4.7F).

4.3.4. Bound CCL21 Gradient Requires either LN ACKR4 OR Afferent Flow

To form CCL21b gradients in the interfollicular region of the LN, it is necessary to either have afferent flow with a low incoming concentration of CCL21u or have ACKR4 on the ceiling of the subcapsular sinus. C_{in} was set to 0 nM for all the cases, and for the “no flow” cases, we decreased the afferent flow to 1% of the baseline flow. Comparison of four combinations with flow and ACKR4 being on and off (Figure 4.8) showed that in the presence of flow or LN ACKR4 the gradients were similar to the baseline case. However when both flow and LN ACKR4 were removed (Figure 4.8D), the average CCL21u concentration in the T cell cortex increased about ninefold. Increased CCL21u concentrations to levels much higher than ECM binding K_D (1.3 nM) led to saturation of CCL21b and in turn the elimination of the CCL21b gradient (Figure 4.8G).

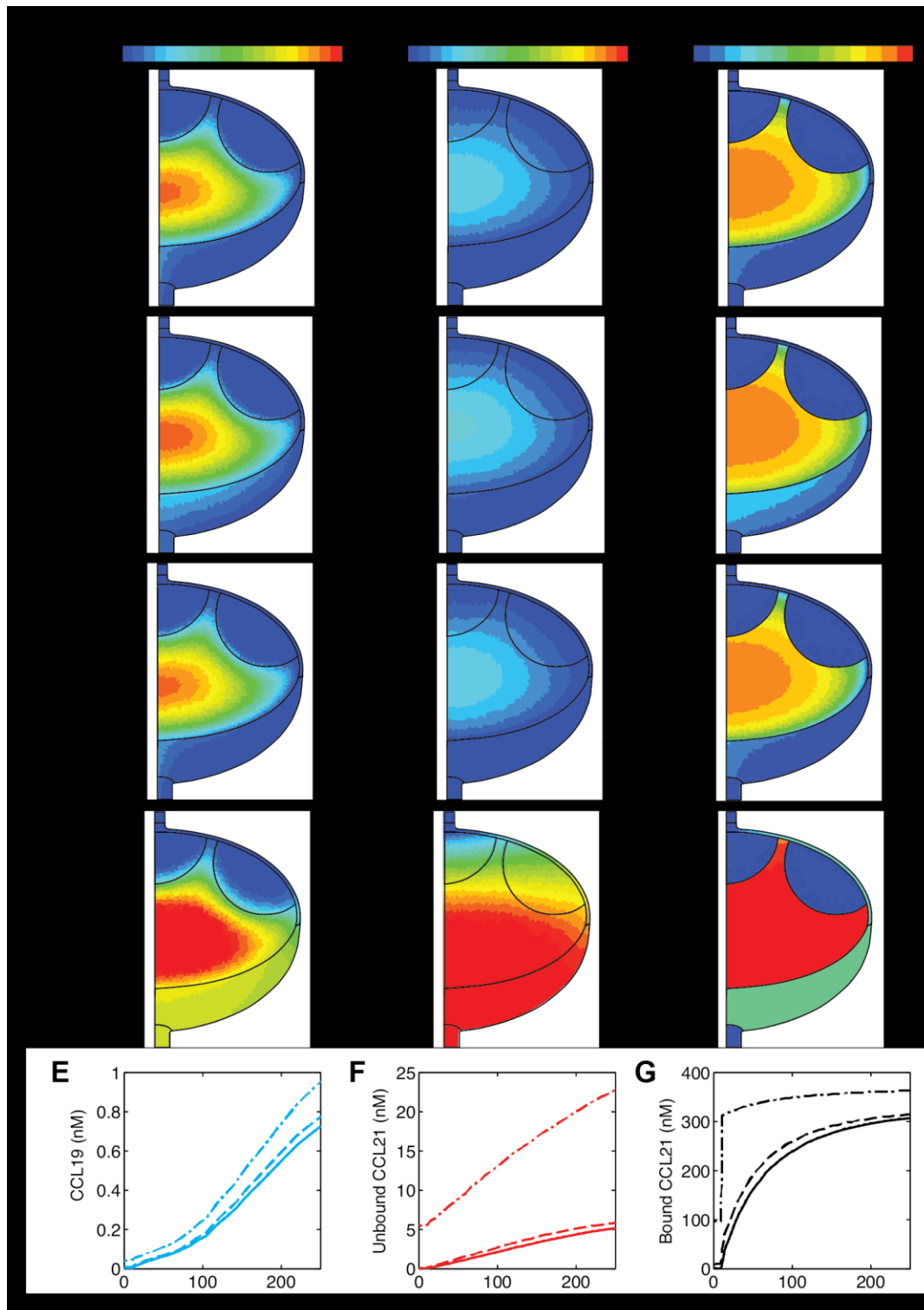


Figure 4.8. LN ACKR4 or afferent flow effect. Contours and plotted gradients of CCL19 (left column), CCL21u (middle column) and CCL21b (right column) compares the case with flow and ACKR4 (**A**, solid lines in **E-G**), to a case without flow but with ACKR4 (**B**, dashed lines in **E-G**), a case with flow but without ACKR4 (**C**, solid lines in **E-G**), and a case without flow or ACKR4 (**D**, dash-dot lines in **E-G**). The first three cases have very similar contours and gradients (**A-C**), however when both flow and ACKR4 are removed the CCL21b gradient is abolished (**D**, **G**). The dotted line is indistinguishable from the solid line in **E-G**.

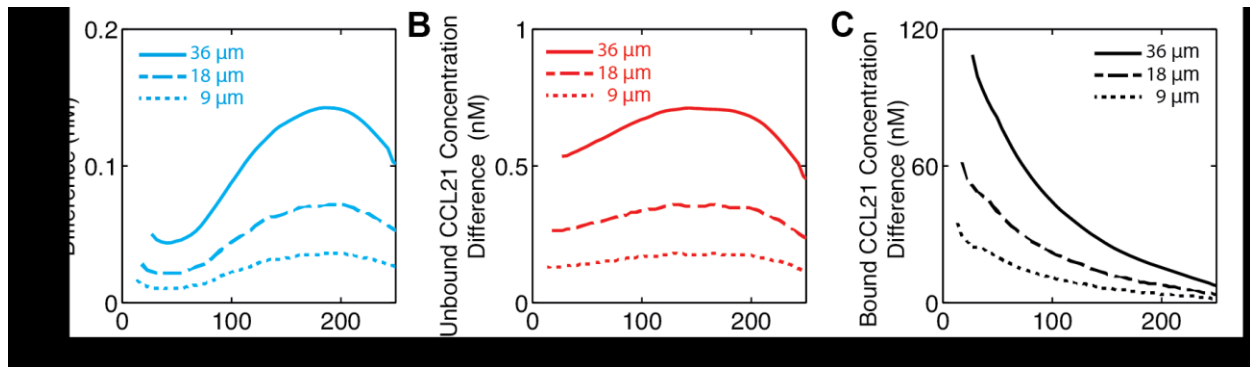


Figure 4.9. Chemokine concentration difference across cells in interfollicular region. For larger cells of 36 μm (solid lines) the observed concentration differences for CCL19 (A) CCL21u (B) and CCL21b (C) between the leading and trailing edges are larger than the smaller cells of 18 μm (dashed lines) and 9 μm (dotted lines). These concentration differences are calculated from the baseline case presented in Figure 4.4.

4.3.5. Cell Size Matters

Cell size is an important determinant of how large a concentration gradient needs to be for a cell to be able to detect a difference between its leading and trailing edges. In the range of the cell sizes explored here (9, 18 and 36 μm), there was a linear relationship between the cell size and the concentration difference (Figure 4.9A-C). This magnifying effect exists for the gradients of CCL19 (Figure 4.9A), CCL21u (Figure 4.9B), and CCL21b (Figure 4.9C). The slope and curvature of the concentration profile determines the shape of the concentration difference curves. For instance in the baseline case, CCL21b concentration gradient start sharply at values higher than 100 nM concentration difference in the interfollicular region and the slope decreases deeper in the cortex (Figure 4.4G), which result in the concentration differences being greater in the interfollicular region than those deeper in the T cell cortex (Figure 4.9C). Due to the higher overall concentrations of CCL21b, the CCL21b concentration differences were two orders-of-magnitude

greater than CCL19 and CCL21u. These concentration differences were always positive for CCL19 and CCL21 meaning that all the gradients, even though some were small, could encourage cells to migrate inward in the cortex.

4.4. Discussion

The aim of this study was to identify the key parameters involved in the formation of LN chemokine gradients that are crucial for immune cell trafficking and subsequent development of adaptive immunity [12, 19, 99]. A mathematical model was constructed that incorporated the physical mechanisms of mass transport (diffusion and advection), as well as the chemical reactions of CCR7, ACKR4 and ECM binding dynamics. Analysing the behaviour of this complex system of equations provided insight into the relative importance of each of the physical and biological phenomena in establishment of the gradients. The general shape of the gradient of bound CCL21 under baseline conditions (monotonic increase in the interfollicular region) was similar to the experimental observations of immunostained extracellular CCL21 from unfixed nonpermeabilized sections of popliteal LNs by Ulvmar et al. for the WT mouse [19]. The model additionally provided the concentration distributions of CCL19 and CCL21u that are currently difficult to visualize experimentally due to low concentrations and the washout effect [87, 95]. The main strength of the model is therefore the ability to use the available experimental data in building confidence in the computational model, to then further utilize it for investigation of impossible or experimentally expensive scenarios. For instance, Schumann et al. demonstrated how immobilized CCL21 activates integrins on DCs whereas soluble CCR7 ligands are required for steering of the DCs, which emphasizes the need to have information

about both forms of the chemokine [95]. The reductionist experimental approaches are well suited for investigation of individual mechanisms that can then be used as principles underlying the model. However, the integration of all the mechanisms, along with sensitivity analysis is required to build a deeper understanding of how the system functions.

A major finding was that the concentration of chemokine entering the LN appears to be more important in formation of the interfollicular CCL21b gradient than the amount of ACKR4 on the ceiling of the capsule. Additionally we found that LN capsule ceiling ACKR4 is not sufficient to stabilize the gradient. While this new insight is at odds with the conclusion commonly associated with the study of Ulvmar et al. [19], it does not contradict with their experimental findings as the KO mice were globally deficient in ACKR4 [19]. Cells in the upstream tissue (e.g. collecting vessel LECs, skin Keratinocytes and initial lymphatic LECs) express ACKR4 that presumably scavenge any CCL21 and CCL19 produced in the upstream tissue before lymph enters the LN [102]. However in the ACKR4-deficient mice, ACKR4 was eliminated in LN capsule ceiling LECs as well as all the upstream tissue cells [19, 187]. Our results suggest that the concentrations of CCL21 and CCL19 produced by the upstream tissue (and not scavenged) were transported via lymph to the LN. Indeed, Russo and colleagues [197] measured concentration of CCL21 and CCL19 from skin-draining afferent lymph of human subjects and demonstrated that the physiologic concentration of CCL21 and CCL19 to be 0.016 nM and 0.011 nM, respectively, which were very low as expected. Unfortunately, measurement of CCL21 and CCL19 concentration from afferent lymph of mice has not been attempted. Development of a mouse popliteal vessel cannulation procedure for sampling the afferent lymph in WT, transgenic, along with computational models can

substantially improve our understanding of the mechanisms chemokine gradient regulation. Application of techniques for local gene deletion could be used to test this hypothesis in animal models.

Elimination of afferent flow demonstrated the conditions under which the LN ACKR4 do play a role in maintaining the gradient in the interfollicular region. As explained above, afferent flow washing the sinuses with low concentration of chemokines appears to be the main mechanism for interfollicular gradient formation. LN ACKR4 only serve to stabilize the gradient when the flow is stopped. CCL21b gradient in the interfollicular region is abolished only when both flow and LN ACKR4 are eliminated. In the absence of flow, ACKR4 can scavenge a portion of the CCL19 and CCL21 produced by stromal cells. The significant negative correlation between ACKR4 in capsule ceiling LECs and efferent concentration of CCL19 and CCL21 supports this idea. This is particularly important in designing new experiments and interpretation of the data from excised tissue, because the termination of flow associated with tissue harvesting has the potential to change the gradients of unbound chemokines. Bound CCL21 should remain stable for a few hours due to its strong binding characteristics. This is supported by demonstrated DC migration on tissue sections [87, 95].

Parameter sensitivity analysis indicated the parameters with dominating correlations such as afferent concentrations of chemokines (discussed earlier), production by stromal cells, CCR7 expression level, and structural changes (that might change effective diffusion coefficient of the chemokines). FRCs are the main source of CCL21 and CCL19 production in the LN, which are mostly located in the T cell cortex [195]. The produced chemokine then diffuses towards the sinuses where it is washed by higher lymph flow. Increased production by stromal cells led to an

increase in paracortex concentrations, resulting in larger gradients for chemokine diffusion towards the sinuses. A similar behaviour is observed when D_{eff} is decreased, which could occur as a result of changes in the cell density or ECM deposition in the node paracortex. Increased matrix density in the LN provides more binding sites for CCL21, which amplifies the concentrations of CCL21b and its gradients (data not shown). Increasing CCR7 appeared to reduce the gradient of CCL19 and not CCL21, mainly due to the internalization of CCL19. Overall, in addition to changes in the expression levels of proteins (CCL19, CCL21, ACKR4 and CCR7), physical parameters such as flow and effective diffusion play an important role in stabilizing the chemokine gradients in the LN.

Occupancy of more than 94.7% of CCR7 molecules by CCL21b in the T cell cortex was due to the two orders-of-magnitude higher concentrations of CCL21b compared to CCL21u and CCL19 in that region. Lower concentration of CCL21b in the follicles was due to lower binding site density, which meant CCR7 molecules stayed mostly in the unbound form providing higher concentration for binding, internalization and scavenging of CCL19. This led to lower concentration of CCL19 in the B cell follicles. In the T cell cortex, most CCR7 receptors were bound to the immobilized CCL21, leading to a much lower scavenging rate of CCL19 there. The localization of highest levels of CCR7 internalization after CCL19 binding was in the B cell-T cell border of the follicles. Follicular helper T cells (T_{FH} cell) are known to express CXCR5 (its ligand is CXCL13) and migrate towards the follicles due to the CXCL13 gradients generated by follicular dendritic cells (FDCs) [203, 204]. The localization of these cells in the follicle border is essential in triggering the formation and maintenance of germinal centres [203]. A future possible application of our

analysis techniques is to investigate if the higher internalization levels of CCL19-CCR7 in this region play any role in the germinal centre reaction.

The shapes of cell span CCL21b concentration difference curves (Figure 4.9C) in the interfollicular region were very similar to those predicted by Weber et al. based on CCL21 concentration fields around mouse ear lymphatic vessels [87]. They reported a functional gradient that extended 100 μm from the closest lymphatic vessel. We intentionally used the same assumed cell sizes to facilitate comparison with their experiments. The cell span concentration difference predicted here was strongest in the first 200 μm . Furthermore, previous studies have shown that dendritic cells respond to CCL19 and CCL21 gradients of 20 nM/mm [190], which translates to 0.18, 0.36 and 0.72 nM concentration difference between the leading and trailing edges of cells of 9, 18 and 36 μm in diameter, respectively. Based on our data, cells in the interfollicular region of the LN can respond to CCL21 (unbound and bound) gradients, but it is questionable if interfollicular gradient of CCL19 is steep enough for induction of directed migration. The experimental studies have not explored the minimum CCL19 gradient that could induce directed migration, and the degree by which the predicted interfollicular gradients can result in cell migration response remains to be elucidated.

The model presented here includes more than fifty parameters many of which are measured experimentally, but one of the limitations of the model is the uncertainty in the parameters that are not attempted to be measured before or are currently impossible to measure. We have explained the uncertainty in each of the parameters in the respective parts in the Methods, and then performed a parameter sensitivity analysis on the parameters that were expected to affect the gradient shape and size. In this parameter sensitivity analysis, we changed those input

parameters (all at the same time) and investigate how the outputs correlate to each of the inputs. This method helps us determine which parameters are crucial regulators of the outcome and are necessary to be measured experimentally. From the parameters we studied here, afferent concentration of chemokines was shown to be more important than numbers of ACKR4 and CCR7, production level of CCL21, and effective diffusion in determining the CCL21b gradient. Another limitation of the model is that it assumes that the production level of chemokines by stromal cells and total receptors available on each cell are constant. In fact, Tomei et al. reported a shear-dependent production of CCL21 by FRCs in 3D collagen cultures [142]. Effective diffusion in different regions of the LN was another parameter that could determine the size of the gradient but has not been measured before for chemokines in LN. Furthermore, our model assumed the blood vessel permeability to chemokines to be close to that measured for albumin. Based on the molecular weight comparison of albumin (68 kDa) versus CCL19 and CCL21 (8.8 – 12.2 kDa), the radius of the chemokines are approximately half that of albumin (1.6-1.9 versus 3.6 nm) [79]. This leads to a chemokine permeability of an order-of-magnitude greater than that of albumin [205]. Although we showed that even an order of magnitude higher permeability does not change the results significantly enough to change any of the conclusions, we recommend the better estimate to be used for the future studies. In addition, our current model is limited to the transport of CCL19 and CCL21 (unbound and bound forms). Indeed we know that CXCL12 and CXCL13 are localized in the B cell follicles and are essential for the recruitment of B cells and formation and function of the follicles [206]. Addition of these two chemokines and their receptors (CXCR4 and CXCR5) are the important next steps for further development of the model. Although CCR7 cell actions with regard to receptor

uptake and corresponding change in concentration are modelled, the effects of resulting cell migration are not included because we assumed that cell population density remains constant in each region and does not get modified by the chemokine gradient. This model can be coupled at the molecular transport level with the agent-based models (ABM) of cell migration in the lymph node to investigate cellular chemotaxis and haptotaxis in the LN [118].

In summary, this model aims to integrate our knowledge of lymph transport in the lymph node with associated chemokine ligand receptor interactions to build a comprehensive model of CCL19 and CCL21 transport and gradient formation in the LN. Our model showed that ACKR4 density in the collecting lymphatic vessels (and not the concentration on the ceiling of the LN capsule) is critical in maintenance of the low afferent concentration of CCL19 and CCL21 to stabilize the gradients in the interfollicular region of the LN. Moreover, we showed that either ACKR4 or afferent flow is necessary for sustained gradients. Finally, using parameter sensitivity analysis, we identified the parameters that can modulate these chemokine gradients.

CHAPTER 5

MEASUREMENT OF SHEAR STRESS- MEDIATED INTRACELLULAR CALCIUM DYNAMICS IN HUMAN DERMAL LYMPHATIC ENDOTHELIAL CELLS

5.1. Introduction

Lymphatic pumping relies on specific mechanical cues (e.g., flow and pressure) to modulate pumping activity [20]. Upon a modest increase in transmural pressure (stretch) in isolated rat mesenteric lymphatic vessels, the vessel tone changes, the phasic contraction strength of the lymph pump increases and the frequency of the pumping is elevated [20, 207]. On the other hand, when a flow (shear) is induced in these vessels, the contraction frequency drops three-fold supporting the importance of mechanotransduction in regulation of pumping activity [20, 21]. Because LEC are subjected to both flow-induced shear stress and stretching as the vessel contracts and relaxes, these cells represent a logical target for investigating important mechanosensitive control mechanisms. Although the importance of mechanical shear stress has been investigated extensively in blood endothelial cells [22-24, 26-29], very few studies have attempted to unveil the effect of mechanical forces on LEC both *ex vivo* and *in vitro* [30, 31].

In vascular ECs, shear stress regulates the production of vasoactive substances such as nitric oxide (NO) [208, 209], endothelin-1 [210-212], and prostacyclin [213] as well as intracellular ions, the most important of them being calcium [24, 27, 214]. Intracellular calcium is a ubiquitous key second messenger that can regulate NO synthesis, cytoskeleton reorganization and endothelial permeability. Rapid increases in intracellular calcium lead to activation by phosphorylation of endothelial nitric oxide synthase (eNOS) resulting in subsequent release of NO, the most important vasodilator in the body [209, 215, 216]. Furthermore, the Ca^{2+} -calmodulin complex activates myosin light chain kinase (MLCK) leading to increased cell contractility/tone and cytoskeletal reorganization

that modulates monolayer permeability [217]. Although the physiological and pathological effects of vasodilation and permeability changes are well documented in blood vessels, there is still a paucity of published works about their role in lymphatic vessels. In particular, permeability changes can potentially increase the exchange of important immunomodulatory signals including antigens and cytokines between the lymphatic vessels and surrounding tissue, thus potentially facilitating the mobilization of dendritic cells [218].

Endothelial cell calcium dynamics can be regulated by agonists (e.g. bradykinin, acetylcholine, etc.), and mechanical forces such as shear stress [24, 214, 219]. Agonists bind to G-protein coupled receptors (GPCR) or receptor tyrosine kinases (RTK), thereby activating phospholipase C (PLC) and cleavage of phosphatidylinositol bisphosphate (PIP₂) resulting in formation of inositol (1,4,5)-triphosphate (IP₃) [220-222]. IP₃ then binds to the IP₃ receptor (IP₃R) on the ER membrane and releases the intracellular calcium stores into the cytosol. Similarly, experiments have also shown a transient upregulation of IP₃ in ECs at the onset of shear stress [223, 224]. This suggests shear stress can utilize parts of the same pathway as receptor-operated mechanisms to mobilize the ER calcium.

Although several mechanosensors of shear stress in endothelial cells have been proposed, such as the glycocalyx [28], plasma membrane channels [23], matrix adhesion proteins [225], primary cilia [226], and membrane receptors (e.g. GPCRs and RTKs) [227], the contributions of each of these mechanosensors in the final signal remain to be elucidated [228]. For shear stress-induced intracellular calcium signalling, ATP-binding purinergic membrane receptors have been demonstrated to play an important role [214, 229, 230]. However, the pathway by

which intracellular calcium is regulated under low concentrations or absence of ATP is incompletely resolved [27, 214].

With the growing understanding of the importance of mechanics and mechanotransduction in the lymphatic system and the acknowledged high sensitivity of lymphatic tissues to pressure and flow, a dynamic measurement of intracellular calcium is crucial for a better understanding of the regulatory mechanisms at the cellular scale, which can then be integrated into models to help explain the responses seen experimentally at the tissue and organ levels. The aims of this study were: 1) to measure intracellular calcium dynamics in lymphatic endothelial cells under different levels of shear stress; and 2) to identify the source of the signal by manipulating both intracellular stores and extracellular calcium concentration.

5.2. Methods

5.2.1. Cell Culture

A commonly used commercial cell-line of juvenile human dermal lymphatic endothelial cells (HDLEC) was obtained from PromoCell, Germany. The exact lymphatic vascular origin of the HDLEC is not precisely known since the dermal lymphatic network contains lymphatic capillaries, precollector and collector lymphatics. HDLEC were cultivated in micro-vascular endothelial growth medium 2 (MV2), PromoCell, Germany. The media of the flasks were changed three times a week, and HDLEC with passages less than 6 were used for all the experiments. Due to the origin of the HDLEC from human foreskin, two batches of these cells were required to perform this study using only low passage cells. Flow chambers were coated with 2% gelatin for 4 hr at 37°C, and then were seeded with the HDLEC at

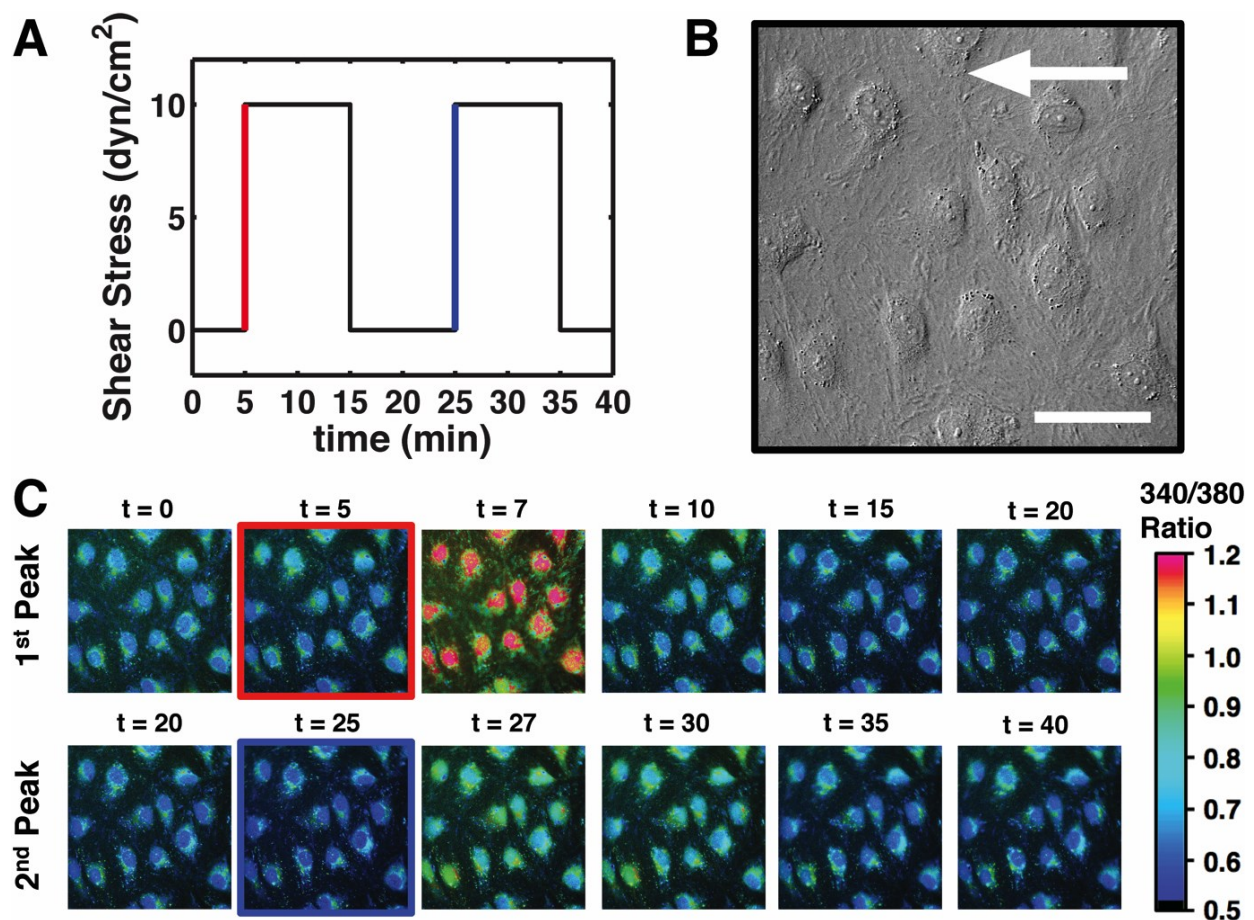


Figure 5.1. $[Ca^{2+}]_i$ increased with step changes in shear stress. **A**. Cells were kept under no-flow condition under the microscope for 5 min before a step change in flow increased shear stress to 1, 3, or 10 dyn/cm² (the red line). The shear stress was kept constant in the elevated level for 10 min after which it was dropped back to zero. 10 min after the shear stress stopped, the same pattern of on-off in shear stress was repeated (starting with the blue line). **B**. DIC images were captured at each time-point to visualize the state of HDLEC in the flow chambers. The white arrow shows the direction of the flow. Scale bar: 50 μ m. **C**. Pseudocolor 340/380 ratio images show a stable $[Ca^{2+}]_i$ before the flow started. After a step increase in shear stress (red-bordered image), the signal peaked in a few minutes (at $\sim t = 7$ min) and then immediately started to decline to reach levels near the baseline. 10 min of no-shear condition resulted in a stable baseline followed by a second increase in shear stress (blue-bordered image). The $[Ca^{2+}]_i$ signal peaked again (at $\sim t = 27$ min), but the $[Ca^{2+}]_i$ levels were not as high as the initial response in this example. This example is for shear steps of 10 dyn/cm² done on the same cells in the DIC image of panel B. Red and blue lines and borders in panels A and C correspond to the same events.

50% confluence. The cells adhered to the gelatin coating on the cover slips at the bottom of the chambers. HDLEC were cultivated under static conditions in the chambers for at least 3 days or when more than 90% confluent (Figure 5.1-B). The culture media was replenished every 24 hr after seeding the cells.

5.2.2. Shear Stress Apparatus

Polydimethylsiloxane (PDMS) single-use microfluidic channels were formed to apply controlled shear stress on endothelial cells. Standard photolithography was used to fabricate the master moulds and the PDMS chambers were replicated from the mould using soft-lithography [231]. Briefly, a 100-120 μm film of SU-8 2050 negative photoresist was coated on 3 inch silicon wafers. After baking steps at 65°C and 95°C, the film was exposed to UV light through a dark-field mask to transfer the design to the film. At the end, the patterns were developed in Microchem SU-8 developer reagent. The replicated PDMS parts were punched, autoclaved, dried, and then bound to glass cover slips (#1) ready for cell culture [231]. A computer-controlled syringe pump was used to apply step changes in shear stress on the cell monolayer in the chambers. The baseline signal was acquired for the first 5 min, then flow was started to obtain a constant shear stress (1 dyn/cm^2 , 3 dyn/cm^2 , or 10 dyn/cm^2) for 10 min. Flow was then paused for 10 min for restabilization before applying a second onset and offset of the shear stress (Figure 5.1-A). Although the physiologic waveform of shear stress on lymphatic vessel wall is more dynamic and complicated, this simplified waveform facilitated investigation of the basic response of HDLEC to constant shear stress levels within the physiological ranges we have previously observed in small collecting lymphatics [30]. Shear stress was determined using the relationship between flow rate and shear stress between the two parallel

plates, namely $\tau_w = 6\mu Q/h^2w$, where τ_w is shear stress, μ is viscosity of media, Q is flow rate, h is the channel height, and w is the channel width.

5.2.3. Calcium Measurement

HDLEC were serum starved in DMEM/F-12 (Gibco) for at least 2 hours before the experiments started. Cells were then incubated with 2 μ g/ml Fura-2 AM in F-12 media containing 0.1% DMSO for 30-45 min. Then cells were washed with F-12 or physiologic saline solution (PSS: NaCl 145mM, KCl 4.7mM, CaCl₂ 2mM, MgSO₄ 1.17 mM, NaH₂PO₄ 1.2mM, Dextrose 5mM, Sodium Pyruvate 2mM, EDTA 20 nM, MOPS 3mM, and 2% HI FBS) and incubated for another 30 min for de-esterification. The Ca²⁺-free PSS was prepared with similar formulation as PSS, but contained 4 mM EDTA instead of CaCl₂. Finally chambers were transferred to the flow setup, and experiments were run using the desired buffer (F-12, PSS, or Ca²⁺-free PSS).

Pairs of fluorescent images were taken by exposure to 340nm and 380nm excitation wavelengths. The image pairs were obtained every 15 seconds using an IX81 microscope (Olympus)-based system as described previously [232]. Differential interference contrast (DIC) images were also captured in each time-point to monitor cell morphology. Multiple regions of interest (~20-40 ROIs), each containing a single endothelial cell, were selected for data analysis in each experiment. At each time point, the background fluorescent signal in each wavelength was measured in a region not containing any cells and was subtracted from all the ROIs for the respective wavelength. Dividing background-subtracted 340nm images by 380nm images resulted in ratio images (Figure 5.1-C). The mean ratio was first calculated in each ROI and then averaged between all ROIs within a single chamber to obtain a

trace for mean changes in ratio for each experiment. Furthermore, the mean data from several experiments (n=4-9) were averaged to calculate the mean ratio for each type of experiment. Additionally, standard error of mean (SEM) was calculated using the mean values from each condition to represent variability between individual experiments and not variability of the response within each experiment.

The ratio of 340nm images over 380nm images (340/380 ratio) can be converted to spatial calcium concentration field using a calibration equation in the form of

$$[Ca^{2+}]_i = K_d \frac{[R - R_{\min}] F_{\max}^{380}}{[R_{\max} - R] F_{\min}^{380}}, \quad (5.1)$$

where $[Ca^{2+}]_i$ is intracellular calcium concentration, K_d is dissociation constant for fura-2-calcium binding, R_{\min} and R_{\max} are minimum and maximum ratios measured under saturating levels and absence of calcium respectively, and F_{\min}^{380} and F_{\max}^{380} are fluorescence intensity with 380nm excitation measured under saturating levels and absence of calcium respectively.

5.2.4. Curve-fits

MATLAB (R2013a) curve-fit toolbox was used to fit a linear function to the upstroke and an exponential function to the downstroke of each calcium signal. For the upstroke, linear least-squares method was used to fit a linear function in the form of $\text{ratio} = a_1 \times t + a_2$ to the data. a_1 represents the slope of the upstroke linear fit. This parameter was calculated for the averaged signal of each type of experiment for the first and second peaks. As for the downstroke, non-linear least-squares method with

Trust-Region algorithm was used to fit an exponential function in the form of $\text{ratio} = b_1 \times \exp((t-t_0)/b_2) + b_3$ to the averaged data for each type of experiment. The minimum of the signal in the interval from the peak to 5 min after the flow stop is used as the b_3 parameter for each type of experiment, while t_0 is the time that the signal started to decrease and b_2 parameter represents the time-constant by which the signal drops.

5.2.5. Statistical Analysis

Data are generally reported as the mean \pm SEM. ANOVA was used to compare the result of each peak with its control and also to compare the two peaks in the same type of experiment. Wherever more than two groups were compared, Bonferroni correction was used to ensure statistical significance between group means. All the statistical analyses were done in MATLAB R2013a with a critical p -value of 0.05.

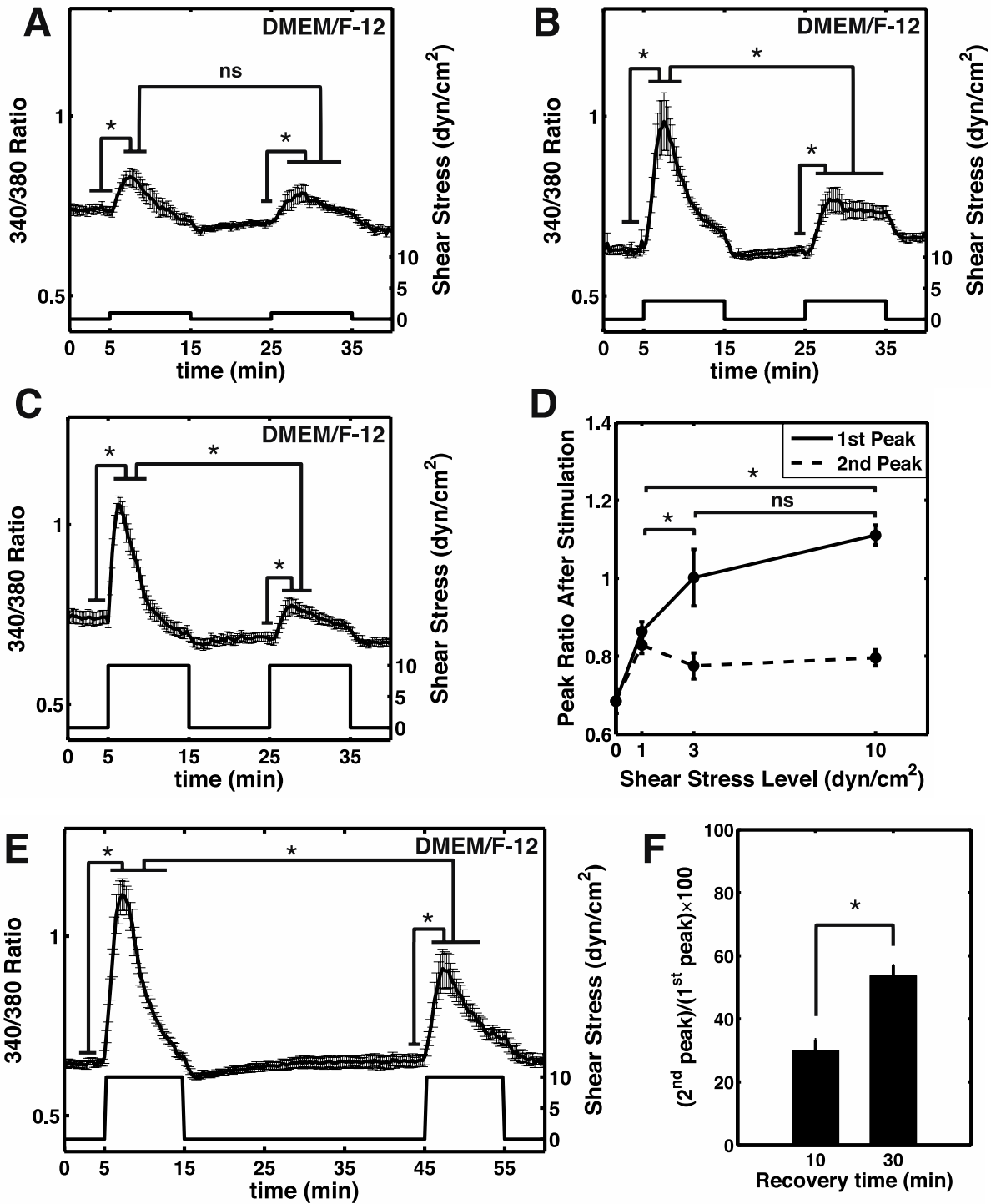
5.3. Results

5.3.1. $[\text{Ca}^{2+}]_i$ Dynamics in HDLEC Is Shear Stress Sensitive

A step change in shear stress (10 minutes long) applied to the HDLEC resulted in an increase in $[\text{Ca}^{2+}]_i$ that peaked and then generally decayed back towards basal levels (Figure 5.2A-C). The magnitudes of the peak rise and the decay were dependent on the shear stress applied. For example, upon initiating a shear stress of 10 dyn/cm², fluorescence ratio (the index of $[\text{Ca}^{2+}]_i$) increased significantly (Figure 5.2C), within 1.75 min (on average for calcium-containing DMEM/F12) from a basal ratio of 0.74 \pm 0.02 to a peak value of 1.11 \pm 0.03. The calcium signal then decreased

exponentially even though shear stress remained elevated (Figure 5.2C). Indeed, at the end of the ten minutes of constant shear (10 dyn/cm^2), calcium had fallen to values below the original baseline. Shear stress was then returned back to zero for 10 min before applying a second step of similar shear stress to evaluate the recovery capability of these cells. During the 10 min “resting” period when shear stress was back to zero, the calcium signal generally recovered back toward the initial baseline, often falling below the initial basal level (Figure 5.2A-C). When a second identical shear stimulus was applied after the resting period (Figure 5.2C), the magnitude of the second peak (0.79 ± 0.02) was significantly lower than the first. Based on the calibration constants, a ratio of 1.11 ± 0.03 for the first peak indicates $126.2 \pm 5.8 \text{ nM}$, and a ratio of 0.79 ± 0.02 for the second peak indicates $57.3 \pm 4.5 \text{ nM}$.

Figure 5.2. $[\text{Ca}^{2+}]_i$ dynamics under different levels of shear stress. **A-C**. Shear stimuli of 1 (**A**), 3 (**B**), or 10 (**C**) dyn/cm^2 showed significant increase in averaged ratio measurements for both shear stimuli compared to respective baselines. However, only for shears higher than 1 dyn/cm^2 was the second peak significantly smaller than the first peak. The ratio signal is the trace with error bars on the primary axis and the shear stress is the square wave shown on the secondary axis. The measurements are reported as mean \pm SEM (A: n = 9, B: n = 4, and C: n = 9). **D**. The average peak response to the first shear stimulus show 3 dyn/cm^2 response is not significantly different from 10 dyn/cm^2 response meaning that $[\text{Ca}^{2+}]_i$ response plateaus at around 3 dyn/cm^2 . The peaks for this panel are calculated in each experiment individually and then are averaged over the number of experiments. **E**. When the no-shear period (recovery time) between the two stimuli was increased from 10 min to 30 min, the second peak significantly increased (mean \pm SEM, n = 6). **F**. With 10 min recovery time, the second peak height was only 30% of the initial peak height, however when this time was increase to 30 min the second peak height significantly increase to 54% of the initial peak height (*: $p < 0.05$, ns: non-significant).



The $[Ca^{2+}]_i$ transients were shear-magnitude dependent for the first peak while the magnitude of the second peak was not significantly dependent on the

magnitude of the applied shear and was significantly lower than the first peak for shears higher than 1 dyn/cm² (Figure 5.2A-D). The initial peaks of [Ca²⁺]_i measured under shear stresses of 1 dyn/cm², 3 dyn/cm² and 10 dyn/cm², elicited peak ratios of 0.86±0.03, 1.00±0.07, and 1.11±0.03, respectively (Figure 5.2A-D) while the time to reach the peak was 3.3±0.1 min, 3.0±0.2 min and 1.8±0.1 min respectively. For the second stimulus of the same shear stress magnitudes, the peak calcium ratios were 0.82±0.02, 0.77±0.03, and 0.79±0.02 with peak times of 4.7±0.3 min, 3.6±0.1 min and 3.1±0.1 min respectively (Figure 5.2A-D).

5.3.2. Contribution of Intracellular Calcium Release versus Extracellular Calcium Entry

We hypothesized that a longer resting time between two stimuli would increase the restoration of the ER calcium stores, thereby resulting in greater recovery of the second peak. With application of 10 dyn/cm² shear, a 10 min no-shear period resulted in a second peak approximately 30% of the height of the first peak, whereas when this recovery time was increased to 30 min, the second peak height increased to about 54% of the first peak height (Figure 5.2E-F). In both cases, the second peak was significantly smaller than the first peak and the 30 min recovery peak was significantly higher than the 10 min recovery peak (Figure 5.2F). This change in the size of the second peak did not affect the time at which the signal reached the peak value (3.1±0.2 min). To investigate the effects of extracellular calcium concentration on shear-induced [Ca²⁺]_i signal, the cells were sheared using PSS solutions with

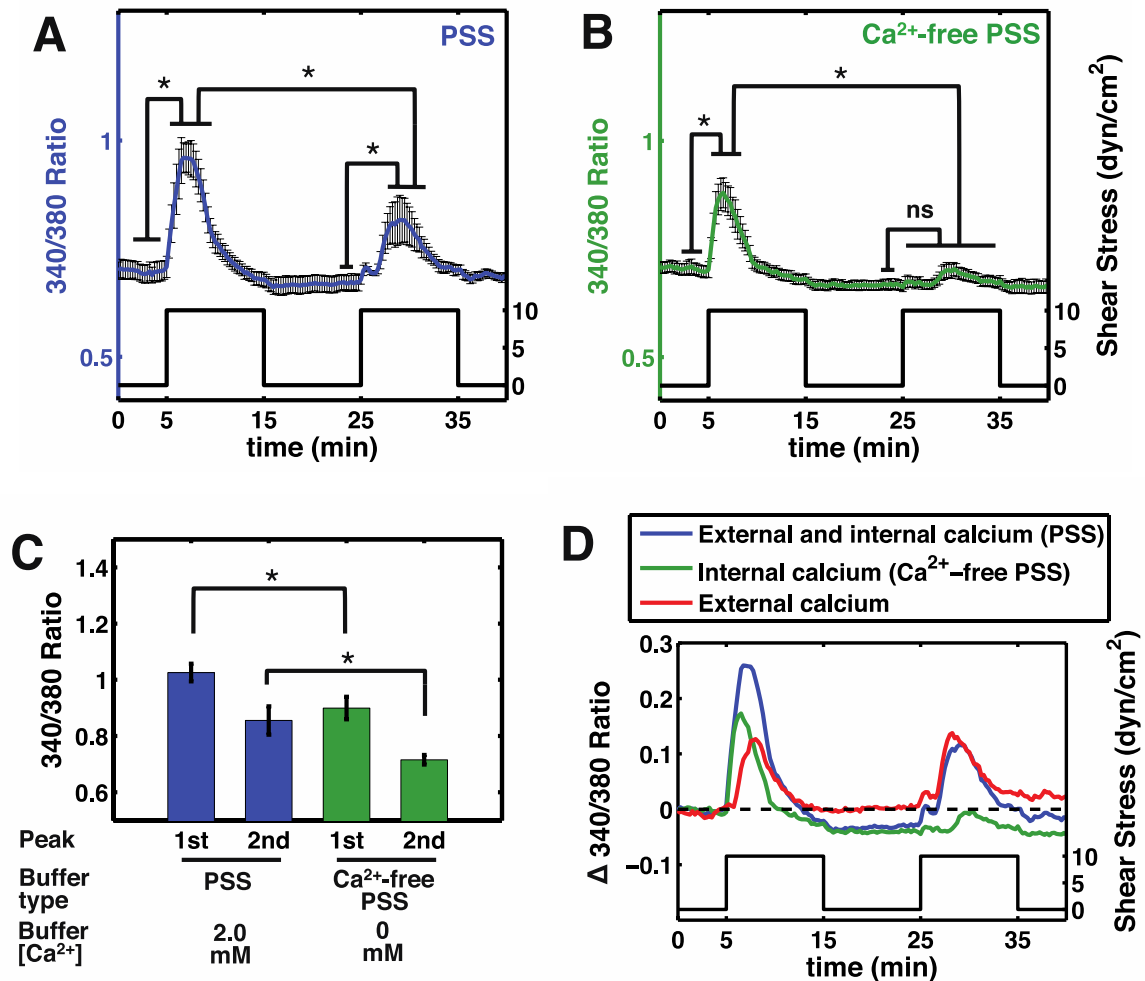


Figure 5.3. Effect of extracellular calcium concentration on $[Ca^{2+}]_i$ dynamics. **A.** HDLEC were subjected to the same shear protocol using Ca²⁺-containing PSS (2 mM) showed first and second peaks that were significantly different from their baseline. The second peak was also significantly smaller than the first peak (mean \pm SEM, $n = 9$). **B.** Exposing HDLEC to the same shear protocol using Ca²⁺-free PSS (0 mM) showed an increase for the first stimulus but the second stimulus failed to increase the $[Ca^{2+}]_i$ signal to levels significantly higher than the baseline. The first peak was also significantly higher than the second peak (mean \pm SEM, $n = 9$). **C.** Comparing the results from Ca²⁺-containing PSS with Ca²⁺-free PSS showed that both first and second peaks were larger in Ca²⁺-containing PSS than in Ca²⁺-free PSS. The peaks for this panel are calculated in each experiment individually and then are averaged over the number of experiments. **D.** Comparisons between Ca²⁺-containing PSS (blue), Ca²⁺-free PSS (green) and the calculated difference between these two signals (red) that represents the contribution of extracellular calcium entry indicated that the peak of external calcium happened 1.5 min later than the peak of Ca²⁺-free PSS. (*: $p < 0.05$, ns: non-significant).

either 0 or 2mM Ca^{2+} as described in the Methods section (Figure 5.3A-B). Shearing in 0mM Ca^{2+} attenuated the first peak and completely abolished the second peak compared to its own baseline, indicating a contribution of extracellular calcium entry in the shear-induced calcium response. The height of the first peak in Ca^{2+} -containing PSS (0.33 ratio, baseline-subtracted) was significantly higher than the first response in Ca^{2+} -free PSS (0.19 ratio) when 10 dyn/cm² shear was applied to the HDLEC (Figure 5.3C). This indicates that the calcium signal is dependent on both intracellular and extracellular sources (Figure 5.3D). To have a better representation of the extracellular calcium entry contribution, the difference between Ca^{2+} -containing signal and Ca^{2+} -free signal was calculated (Figure 5.3D). The extracellular calcium entry appears to reach a peak 1.5 min after the peak from Ca^{2+} -free PSS (representing only the intracellular calcium release). Additionally, the second peak from Ca^{2+} -free PSS was not significantly different from the baseline signal before the stimulus (Figure 5.3B).

5.3.3. Intracellular Calcium Release Is Essential for Shear-Mediated Response

Since the calcium signal was not completely inhibited with the removal of calcium from extracellular buffer, experiments were performed to determine the role of ER calcium stores in the shear-mediated $[\text{Ca}^{2+}]_i$ transients using available calcium ER pump blockers. Thapsigargin (Tg) is known to irreversibly block the sarco/endoplasmic reticulum Ca^{2+} -ATPase (SERCA) pumps responsible for calcium re-uptake from the cytoplasm back into the ER, maintaining low basal cytoplasmic calcium concentration. Upon treatment with 2 μM Tg, $[\text{Ca}^{2+}]_i$ increased substantially,

reaching an initial peak in 4.9 min followed by a slight dip in calcium before achieving a second higher peak after 8.2 min. This signal then decayed from the highest peak levels to a stable level (0.99 ± 0.04) that was significantly higher than the initial basal level (0.64 ± 0.02). These Tg-pretreated HDLEC were then subjected to 10 dyn/cm^2 but this did not produce a significant further change in $[\text{Ca}^{2+}]_i$ (Figure 5.4). The complete disappearance of the shear response (to 10 dyn/cm^2 shear stress) after SERCA blockade suggests an important role for ER calcium release in the generation of the shear-induced calcium response.

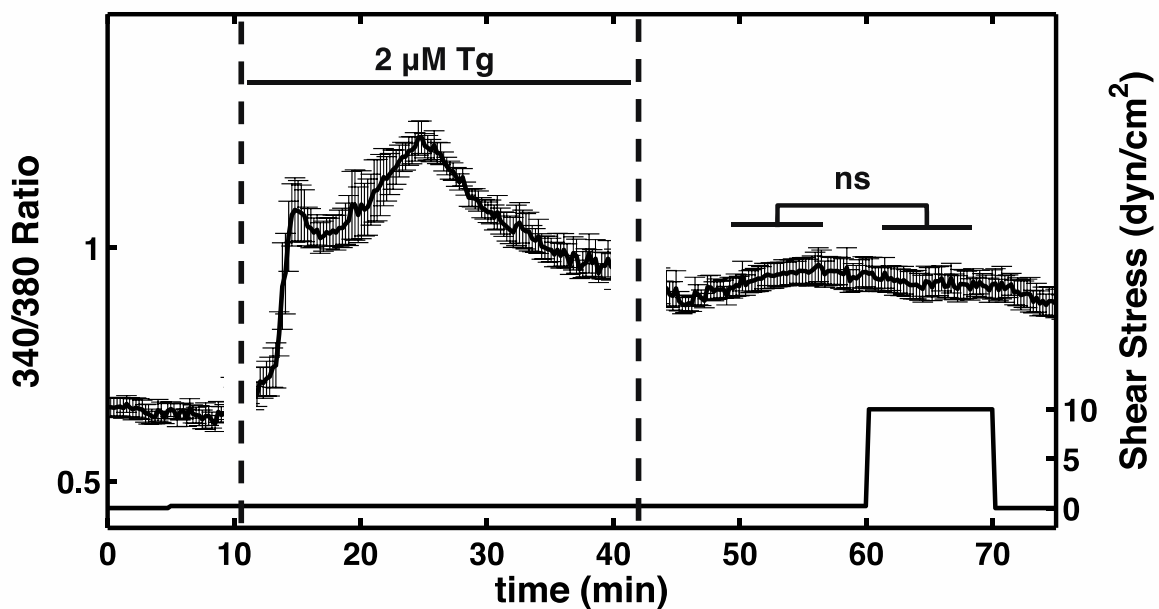


Figure 5.4. Effect of Tg on shear-mediated calcium changes. After reading the baseline signal in the first 5 min, HDLEC were perfused with a small flow of DMEM/F-12 ($\sim 0.2 \text{ dyn/cm}^2$) for another 5 min. The media was then switched to DMEM/F-12 with 2 M Tg with same slow perfusion rate. The HDLEC exhibited two consecutive transient peaks and approached toward a new stable elevated level. At this point the media was switched back to normal DMEM/F-12 when the new baseline was recorded and cells were subjected to 10 dyn/cm^2 shear stress for 10 min. Shear stress did not change the signal significantly in this experiment (mean \pm SEM, $n = 6$, ns: non-significant).

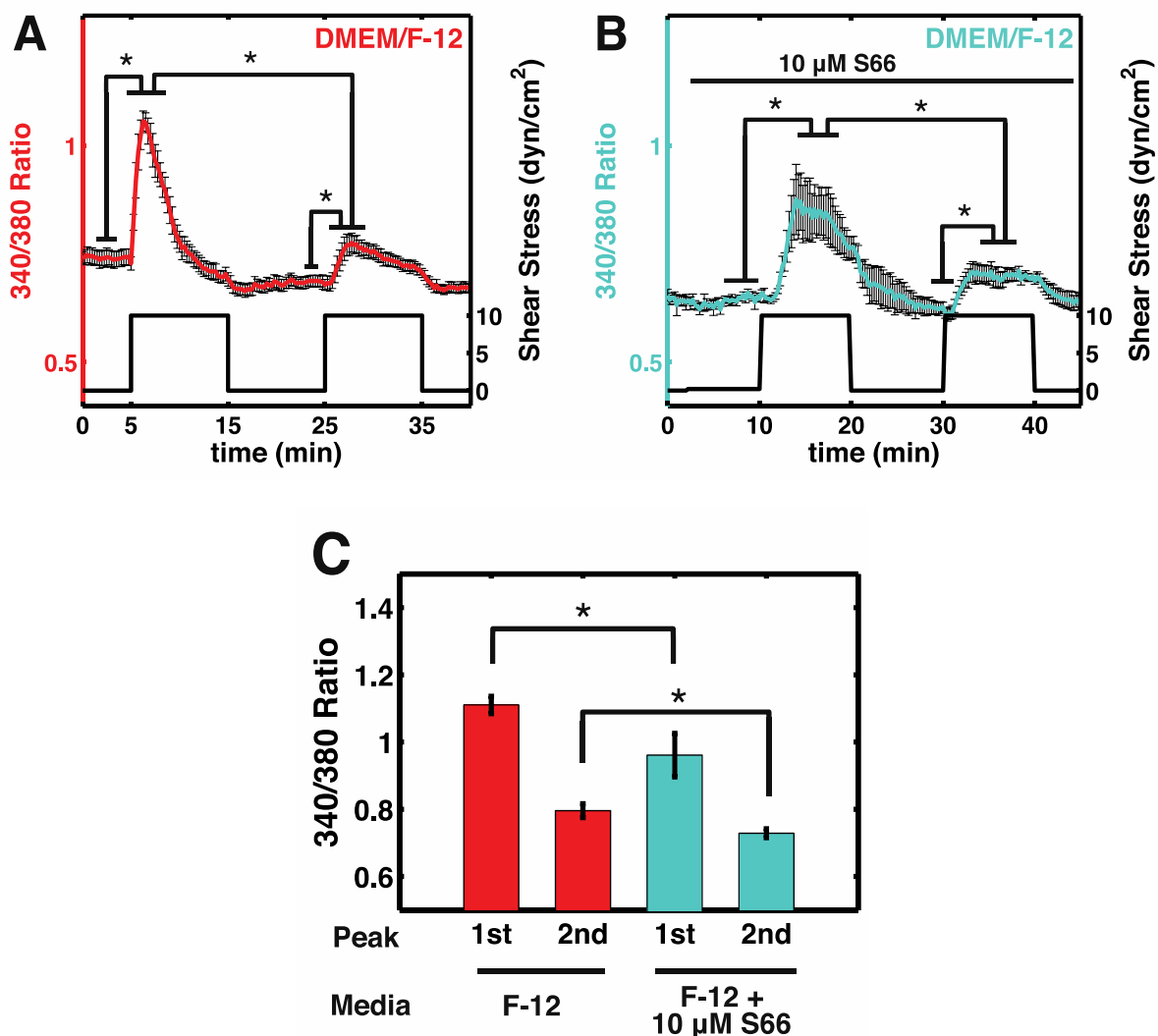


Figure 5.5. Effect of a CRAC channel blocker S66 on $[Ca^{2+}]_i$ dynamics to shear. **A.** Shear-mediated calcium transient under 10 dyn/cm^2 using DMEM/F-12 is shown here (similar to Figure 2C, $\text{mean} \pm \text{SEM}$, $n = 9$). **B.** After recording the baseline for 2 min, HDLEC were perfused slowly ($\sim 0.2 \text{ dyn/cm}^2$) with 10 M S66 in DMEM/F-12 for 8 min. Then a similar shear stress waveform to previous experiments was used to investigate the effect of blocking CRAC channels flow-induced calcium signals ($\text{mean} \pm \text{SEM}$, $n = 5$). The first and second peaks were both higher than their baselines. The second peak was also significantly smaller than the first peak. **C.** Blocking CRAC channels by S66 resulted in smaller first and second peaks compared to control experiments with DMEM/F-12 under 10 dyn/cm^2 . The peaks for this panel are calculated in each experiment individually and then are averaged over the number of experiments. (*: $p < 0.05$).

5.3.4. CRAC Channels Contribute to Extracellular Calcium Entry

The specific role of calcium release-activated calcium (CRAC) channels in mediating Ca^{2+} entry in response to the ER calcium release was investigated by inhibiting these channels using Syntha66 (also known as S66, a specific CRAC channel blocker) [233-235], thereby revealing their contribution to the shear-mediated $[\text{Ca}^{2+}]_i$ signal (Figure 5.5A-B). Blockade of CRAC channels decreased the height of both the first (1.02 ± 0.03) and second peaks (0.73 ± 0.01) relative to their untreated controls (Figure 5.4C). Moreover, S66 treatment often produced a delay of about 2-5 min in the shear-induced calcium response. Specifically, S66 increased the time to reach the first peak to 5.2 ± 0.4 min (2-5 min delay + an increase with a rate of 0.165 ratio/min (Table 5.2)) compared to 1.8 ± 0.1 min without CRAC channel blockade (Figure 5.5A-B).

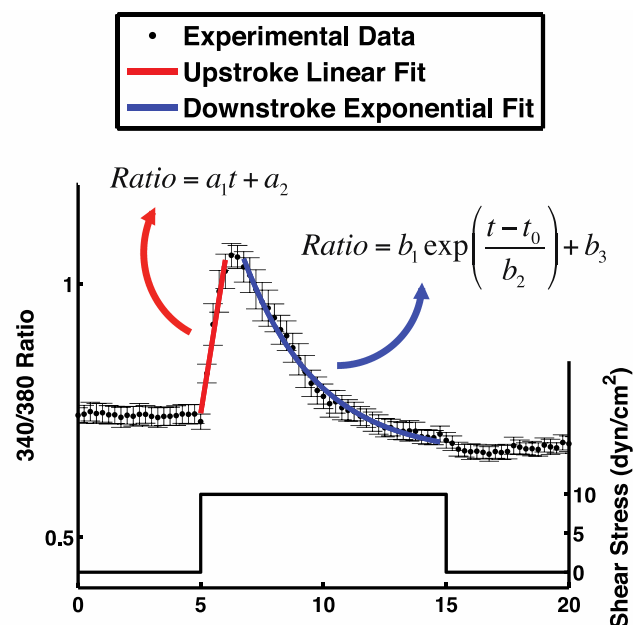


Figure 5.6. Curve-fit to the upstroke and downstroke of the calcium spike. The first peak of the calcium response to 10 dyn/cm^2 shear stress is shown with filled circles (mean \pm SEM, $n = 9$). A sample linear fit of the form $\text{ratio} = a_1 \times t + a_2$ to the upstroke (the red line) and a sample exponential fit of the form $\text{ratio} = b_1 \times \exp((t - t_0)/b_2) + b_3$ to the downstroke (the blue curve) are shown in this figure. a_1 and b_2 are the main parameters that are reported in the Table 1.

Table 5.1. Shear stress level, extracellular calcium concentration and curve-fit parameters for the experiments.

Media	Shear Stress (dyn/cm ²)	Media Calcium Concentration (mM)	1st peak		2nd peak	
			Upstroke Slope – a ₁ (ratio/min)	Downstroke time const. – b ₂ (min)	Upstroke Slope – a ₁ (ratio/min)	Downstroke time const. – b ₂ (min)
DMEM/F-12	1	1.05	0.058	4.6	0.023	10.2
DMEM/F-12	3	1.05	0.192	3.9	0.063	16.1
DMEM/F-12	10	1.05	0.302	3.0	0.057	11.5
DMEM/F-12 (30 min between two stimuli)	10	1.05	0.258	2.7	0.123	5.1
DMEM/F-12 + 10 μ M S66	10	1.05	0.165	5.0	0.053	28.9
PSS	10	2.00	0.163	2.3	0.083	2.6
Ca-free PSS	10	0.00	0.167	2.6	0.024	3.5

5.3.5. Rates of the Calcium Dynamics

The calcium responses to shear were fit to mathematical function to extract parameters for subsequent modelling efforts (Figure 5.6). The $[Ca^{2+}]_i$ increased rapidly to reach a peak value, which was approximated using a linear function in the form of $ratio = a_1 \times t + a_2$ (Figure 5.6, red line). The gradual drop in signal suggested an exponential fit ($ratio = b_1 \times \exp((t - t_0)/b_2) + b_3$) as an adequate approximation for this part of the response (Figure 6, blue curve). Among the curve-fitting parameters, the upstroke slope showing the $[Ca^{2+}]_i$ increase rate (a_1) and the downstroke time constant (b_2) are the most important parameters and are reported for the various cases tested in this study for the first and second peaks (Table 5.1). When the shear stress increased from 1 to 10 dyn/cm² in the absence of inhibitors, the upstroke slope increased six fold for the first peak suggesting a faster increase in the signal,

and the downstroke time constant decreased from 4.6 min to 3.0 min meaning that the signal dropped faster when the shear stress was higher (Table 5.1).

5.4. Discussion

Our findings demonstrate that HDLEC respond to physiologically relevant shear stress with a transient increase in $[Ca^{2+}]_i$ arising from a combination of release from intracellular stores and entry of extracellular calcium (Figure 5.7). With the onset of a constant shear stress, $[Ca^{2+}]_i$ increased quickly and peaked within minutes (usually 100-200 s). This was followed by a gradual decay to levels often below the initial basal concentrations. This calcium response is quite different from that observed with blood ECs, where the signal increases in a shorter time and sometimes a sustained elevation in cytosolic calcium is observed. However, the shear-dependent response of calcium in blood ECs has been shown to be dependent on numerous factors in addition to shear, Table 5.2 [214, 219, 230]. Because this is the first study of this nature done in lymphatic ECs it is difficult at this time to know if these factors play a significant role in the shear-sensitive calcium response we observed. Further studies need to be done to carefully evaluate these factors and the apparent differences in blood and lymphatic EC response to shear. Dull and Davies observed a shear-induced $[Ca^{2+}]_i$ spike that peaked at 134 nM in 6-10s for shear stresses under 6.3 dyn/cm^2 in bovine aortic endothelial cells (BAEC) that was only observed when ATP was present in the media [214]. The current study uses DMEM/F-12 lacking ATP, yet a $[Ca^{2+}]_i$ peak is present when stimulated by shear stress. Additionally, the shear-induced peak time for BAEC with ATP-containing media is much shorter than shear-induced HDLEC with ATP-free media (6-10 s vs. 100-200

s). Liu et al. also measured $[Ca^{2+}]_i$ in BAEC using FRET biosensors under shear stress and observed a doubling in FRET signal in about 10 s that was sustained during the first 300 s [219]. This signal dropped to about 40% after 1000 s. The time to peak is shorter than the present study (10 s vs. 100-200 s), and the rapid decay that was observed in HDLEC in the present study is different from sustained increase in $[Ca^{2+}]_i$ measured in BAEC by Liu et al.

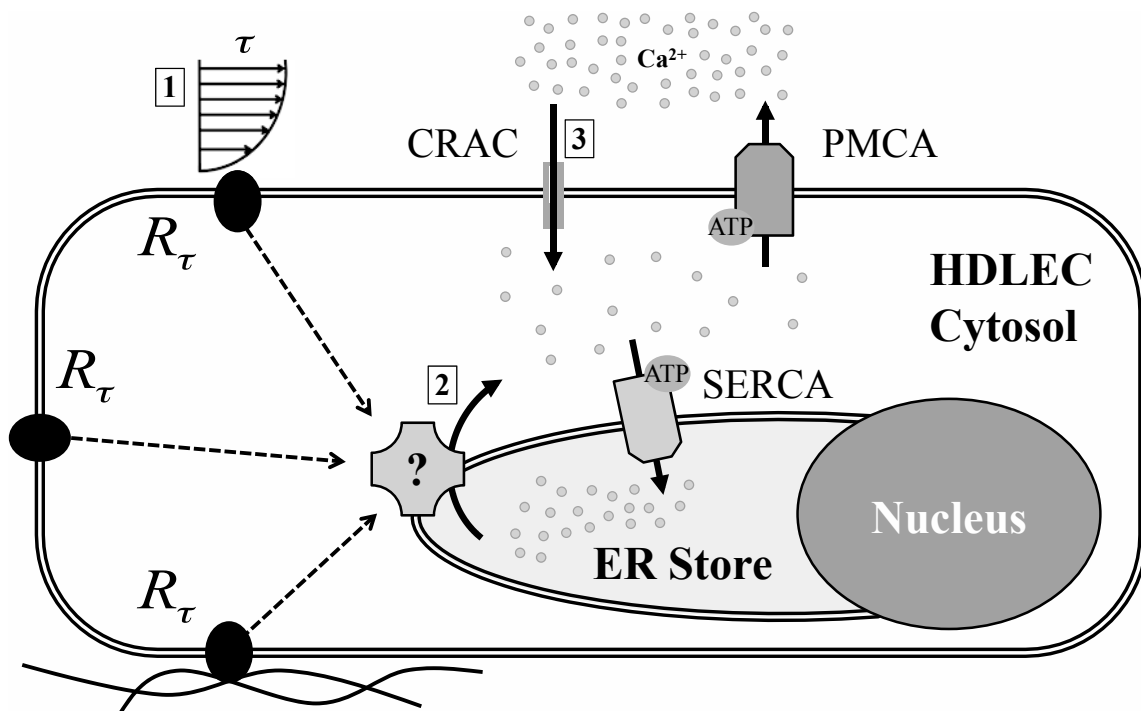


Figure 5.7. Schematic of shear-mediated calcium dynamics in HDLEC. The results of this work suggest that following shear stress mechanosensing in HDLEC [1], the intracellular calcium increases due to ER store calcium release [2]. The increase in $[Ca^{2+}]_i$ initiates Ca^{2+} entry to the cell through CRAC channels [3]. PMCA and SERCA pumps are constantly pumping the cytosolic Ca^{2+} to the extracellular space and ER store, respectively.

Table 5.2. Summary of shear-mediated calcium dynamics data available in the literature.

Paper	Cell Type	Peak Response	Shear Stress Level	Experimental Condition	Culture Condition
Current study	HDLEC	<i>Peak signal:</i> 126.2±5.8 nM <i>Peak time:</i> 100-200 s	10 dyn/cm ²	<i>Technique:</i> 2 μM Fura-2 AM <i>Exp. Buffer:</i> DMEM ^a /F-12	<i>Media:</i> MV2 ^b <i>ECM:</i> 2% gelatin <i>Seeding density:</i> 50% <i>Passage #:</i> < 6 <i>Time between seeding and experiment:</i> 3 days
Dull and Davies 1992	BAEC	<i>Peak signal:</i> 134 nM (avg) <i>Peak time:</i> 6-10 s	6.3 dyn/cm ²	<i>Technique:</i> 5 μM Fura-2 AM <i>Exp. Buffer:</i> DPBS ^c with 1.5 mM Ca ²⁺ + 2 μM ATP	<i>Media:</i> DMEM+HEPES+10% calf serum <i>ECM:</i> 0.1% gelatin
Shen et al. 1992	BAEC	<i>Peak signal:</i> 137 nM (avg) <i>Peak time:</i> 15-40 s	4 dyn/cm ²	<i>Technique:</i> 2 μM Fura-2 AM <i>Exp. Buffer:</i> HBSS ^d with 1.5 mM Ca ²⁺	<i>Media:</i> DMEM+ 10% calf serum <i>Passage #:</i> 5-30 <i>Time between seeding and experiment:</i> after confluence
Liu et al. 2012	BAEC	<i>Peak signal:</i> Two-folds <i>Peak time:</i> 10 s	65 dyn/cm ²	<i>Technique:</i> FRET ^e biosensor <i>Exp. Buffer:</i> DMEM + 10% FBS ^f	<i>Media:</i> DMEM + 10% FBS
Schwarz et al. 1992	HUVEC	<i>Peak signal:</i> 587±88 nM <i>Peak time:</i> ~60 s	~25 dyn/cm ²	<i>Technique:</i> 2 μM Fura-2 AM <i>Exp. Buffer:</i> Krebs Solution with 1.5 mM Ca ²⁺	<i>Media:</i> Medium 199 + 1 mg/ml ATP + 10% human serum <i>ECM:</i> gelatin <i>Passage #:</i> < 2 <i>Time between seeding and experiment:</i> 2-4 days

^a DMEM: Dulbecco's Modified Eagle Medium

^b MV2: Endothelial Cell Growth Medium MV2

^c DPBS: Dulbecco's Phosphate-Buffered Saline

^d HBSS: Hanks' balanced salt solution

^e FRET: Fluorescence resonance energy transfer

^f FBS: Fetal Bovine Serum

In another study, Shen et al. measured $[Ca^{2+}]_i$ in BAEC under shear stress and observed a peak of about 137 nM in 15-40 s under shear stresses higher than 4 dyn/cm², which declined to basal levels in 40-80 s [27]. Similar to other studies on BAEC, this peak time is shorter than that observed using HDLEC, while the peak values are similar. Schwarz et al. applied shear stress for a period of 60 s to individual HUVEC (human umbilical vein endothelial cell) and measured $[Ca^{2+}]_i$ [236]. After an initial increase in signal, they either observed an instantaneous decay of the signal at the offset of shear stress, or the signal continued to increase after shear stopped and reached a peak followed by a decay back to baseline. For a shear of 25 dyn/cm², $[Ca^{2+}]_i$ peaked at 530 nM with time constant of exponential decay reported to be 84 s compared to the HDLEC response to 10 dyn/cm² in this study that peaked at 126 nM with a time constant of 180 s. The time constant measured by Schwarz et al. is during the period that the shear was stopped while in this study the time constant was measured while shear was still applied. While the actual peak time is not reported by this group, the fact that $[Ca^{2+}]_i$ signal did not reach a peak during first 60 s suggests HUVEC have a more similar peak time compared to HDLEC than do BAEC.

The shear-induced rate of increase of $[Ca^{2+}]_i$ was more sensitive to shear magnitude in the low shears (0-1 dyn/cm²) compared to the high shear ranges (3-10 dyn/cm²) (Table 5.1). This suggests either a higher mechanosensitivity of HDLEC to shear stress in low shear ranges, or activation of a strong calcium extrusion mechanism simultaneously that requires higher shears to be fully activated. The shear stress environment to which LECs and blood ECs are subjected are quite different. Local shear stress in the lymphatics is dependent upon the type of lymphatic vessel involved and the conditions to which that lymphatic vessel is

currently exposed. Further, lymph flow in a given lymphangion is highly complex and dynamic due to variable levels of lymph formation upstream coupled with the periodic contraction/relaxation of lymphangions. In rat mesenteric prenodal collecting lymphatics, the resulting wall shear stresses vary dynamically from slightly negative to approximately 12 dynes/cm² in straight segments away from the valves in a matter of a few seconds [30]. In addition, because of the heterogeneous shape of these vessels, shears vary dramatically along the lymphangion, and are up to 2-3x higher on the valve leaflets compared to the downstream straight segments [111]. Furthermore, shear stresses can increase 10x with the increases in lymph formation seen during oedemagenic fluid balance shifts [237]. To the degree that it is relevant to describe flow in a collecting lymphatic with a time-average value, under basal physiological conditions shear stress was approximately 0.64 dynes/cm² in the straight lymphatic segments [30]. However, it is important to note that LEC are only instantaneously and irregularly subjected to this level of shear stress as flow accelerates or decelerates. Shear stresses in pre-collectors and lymphatic capillaries are even lower (~ 0.001 in mouse tail capillaries [238], and ~0.003 dynes/cm² in human skin capillaries [62]). Given the dynamics of this vascular system, it is reasonable to assume LEC are sensitive to transients in shear stress. The results of this study support that hypothesis, and further suggest that HDLEC may respond to smaller transient increases in shear stress than blood ECs. Our results indicate that the shear-mediated [Ca²⁺]_i response is sensitive to shear magnitude between 0 and 3 dyn/cm² (Figure 2D). With increases in shears to levels above that (10 dyn/cm²), the response does not appear to be much different from that seen at 3 dyn/cm². Comparing our data with shear-mediated [Ca²⁺]_i responses in BAEC supports this hypothesis. Specifically, Liu et al. showed a relatively linear increase in the shear-

mediated $[Ca^{2+}]_i$ response in BAEC in the shear stress range of 15 dyn/cm² to 65 dyn/cm² suggesting BAEC are sensitive to a higher range of shear magnitudes compared to HDLEC [219]. This data from BAEC contradicts the study by Shen et al. that reported a signal plateau at 4 dyn/cm² for BAEC [27]. Schwarz et al. applied shear stresses of up to 52 dyn/cm² to HUVECs and observed that the response to shear reached a plateau at about 40 dyn/cm², which is still higher than that observed in HDLEC in this study [236]. Kawai and Ohhashi reported a significant upregulation in eNOS (a molecular signal in the NO pathway downstream of $[Ca^{2+}]_i$) after treatment of collecting LEC with shear stresses between 0.5-1 dyn/cm² for two hours [31], indicating a sensitivity to low levels of shear stress. Furthermore these pattern of shear-sensitive calcium responses and eNOS expression in cultured LEC in general matches the patterns of eNOS expression and NO production we have observed experimentally in rat mesenteric collecting lymphatics in situ [239, 240] and predicted computationally [111].

This study also attempts to distinguish between the role of extracellular calcium entry versus ER calcium store release in the resulting $[Ca^{2+}]_i$ signal. Reduction of the shear-induced calcium response as a result of the calcium removal from the external buffer (cf. Figure 5.3) suggests that the observed calcium rise was in part due to extracellular calcium influx (40% of the first peak height). A similar conclusion was made by Shen et al. when they used EGTA to chelate Ca^{2+} ions in the buffer before applying shear stress on BAEC [27]. In contrast, Schwarz et al. observed that the $[Ca^{2+}]_i$ signal was completely abolished using Ca^{2+} -free buffer. Our results are consistent with the hypothesis that the $[Ca^{2+}]_i$ signal generated in HDLEC subjected to shear in the absence of external calcium comes from intracellular calcium stores, most likely from ER calcium release. We kept the pretreatment time

in Ca^{2+} -free solution to a minimum (2-3 min) in these experiments to minimize the potential loss of intracellular calcium stores that occurs when cells are maintained in a calcium-free environment. In DMEM/F12 experiments, the magnitude of the second stimulus was significantly lower than the first one for shears higher than 1 dyn/cm^2 . Allowing a longer resting interval between repeated stimuli resulted in a greater response to a second application of shear, that was still significantly lower than the first peak (cf. Figure 5.2E). This implies that the shear-activated depletion of calcium stores gradually refill between consecutive shear stimuli. A stronger recovery of the 2nd peak in the case with Ca^{2+} -containing PSS versus an non-significant recovery in the Ca^{2+} -free PSS confirms that external calcium is necessary for the full restoration of the intracellular ER calcium stores. When $[\text{Ca}^{2+}]_i$ increases, the plasma membrane Ca^{2+} ATPase (PMCA) pumps cytosolic Ca^{2+} to the extracellular space and SERCA pumps return cytosolic Ca^{2+} back into the ER to reinstate a low cytoplasmic calcium level. The lack of a significant second peak generated in the absence of extracellular Ca^{2+} indicates that the SERCA pumps may not have effectively restored $[\text{Ca}^{2+}]_{\text{ER}}$ after the shear-stimulated calcium release due to limited $[\text{Ca}^{2+}]_i$. Thus when extracellular calcium is present, recovery of the second peak $[\text{Ca}^{2+}]_i$ response can be achieved by increasing the time between two stimuli and hence providing more time to restore the initial $[\text{Ca}^{2+}]_{\text{ER}}$.

Using BAEC, Liu et al. concluded that the first phase of the shear induced calcium response is caused by extracellular calcium entry and the prolonged increase is from intracellular sources [219]. Our data in HDLEC shows significant differences between BAEC and HDLEC in this respect. In HDLEC, neither the timing nor the slope of the initial rise in the signal is significantly altered by removal of the extracellular calcium (cf. Figure 5.3 and Table 5.1), indicating that the initial phase of

the $[Ca^{2+}]_i$ rise after shear is mainly due to the release of calcium from the ER. The relative contribution of the intracellular and extracellular calcium to the shear-dependent $[Ca^{2+}]_i$ rise is indicated in Figure 3D and suggests that extracellular calcium influx increases the peak magnitude and duration. The elevation in calcium is then followed by a reduction to levels that were often lower than the initial baseline. This unique feature has not been observed in the shear mediated calcium changes in blood ECs and suggests that cytoplasmic calcium removal systems in HDLEC have been activated by shear. Moreover, the decay time constant (b_2 in Table 5.1) appears to be dependent on the shear stress magnitude and decreases as the magnitude increases, thus supporting the shear-activated Ca^{2+} extrusion hypothesis. Mathematical modelling of agonist-induced $[Ca^{2+}]_i$ dynamics in arterial ECs have been developed that include contributions from channels and pumps on the plasmalemmal and ER membrane [241-243]. The effects of shear stress is also included in some models describing $[Ca^{2+}]_i$ dynamics in arterial ECs [243]. However, these models are not able to capture the reduction of calcium below basal levels we observed in HDLEC. We suspect that this particular characteristic of the $[Ca^{2+}]_i$ response in HDLEC is caused by the activation of extracellular and/or intracellular calcium pumps that are either not present or do not have significant effects in blood ECs. Further studies are needed to investigate this important and unique shear-dependent characteristic of HDLEC and to identify the responsible calcium extrusion mechanisms.

Tg (a SERCA inhibitor) administration completely eliminated the shear-induced response, suggesting a critical role for SERCA pumps in the shear-induced calcium response. These data, in combination with the experiments on the effect of extracellular calcium, suggest that extracellular calcium entry is significantly

activated only when the store release process is initiated. Blocking SERCA pumps eventually leads to depletion of ER stores and in turn activates the CRAC channels resulting in the elevation of the calcium signal while under no shear. However, in addition to the depletion of ER stores, the rise in the cytosolic calcium caused by Tg may have also contributed to the loss of the shear-mediated signal. Although Tg is widely used in calcium studies as the first candidate for SERCA inhibition, it may affect other cellular pathways as well. To further delineate the plasma membrane calcium channels involved in the extracellular calcium influx, we investigated the role of CRAC channels using the specific inhibitor S66. S66 blockade of CRAC channels reduced the magnitude of the shear-induced calcium rise, though inhibition of the extracellular calcium entry through CRAC channels did not diminish the calcium rise to the same degree as exposure to calcium free media. The blockade of CRAC channels reduced both the first and second peaks of $[Ca^{2+}]_i$ for 10 dyn/cm² shear relative to the control, and caused a significant delay of 2-5 min in the initiation of the $[Ca^{2+}]_i$ response to shear. The mechanisms by which the CRAC channel inhibition by S66 delays the onset of the initial calcium rise to shear are not clear and have not been reported before in other EC lines. Because removing extracellular Ca²⁺ did not lead to a significant delay of shear-induced $[Ca^{2+}]_i$ signal, it is possible that the delay caused by S66 incubation is due to some unknown effects of S66. It is also possible that preincubation of HDLEC with S66 reduces store content by blocking Ca²⁺ entry through CRAC channels under the basal status. Thus it appears that CRAC channels play a significant role in the rise of $[Ca^{2+}]_i$ induced by shear in HDLEC and other calcium-permeable channels in the plasmalemmal maybe also involved in this process. Further studies on the identities and specific roles of these channels in HDLEC remain to be elucidated.

Although there is a wide range of temporal and spatial variance in shear stress magnitude applied to LEC in different vessels throughout the lymphatics, the step changes in shear stress used here serve to illustrate the basic dynamics behind calcium responses to temporal changes in shear stress. Given the variety of shear stresses to which LEC are exposed *in vivo*, it makes sense to initially “standardize” the shear stress waveform for these kinds of experiments. Future experiments should investigate responses to specific *in vivo* shear stress waveforms, but these would not be expected to significantly alter the conclusions drawn from this study. The images in this study were captured every 15 s, which means the temporal resolution of the results in this study is limited by this time step. Although *in-vitro* studies provide good control over the mechanical forces applied on the LEC, they inherently lack the detailed microenvironmental features present *in vivo* such as the stiffness and complex composition of extracellular matrix (ECM), and lymph composition that may play important roles in LEC mechanosensing. The extent to which these differences can affect the results needs to be addressed in future studies on LEC flow responses. Additionally, the LEC mechanosensors and transduction pathways are yet to be elucidated. The role of ATP-binding purinergic P2X/2Y receptors has been emphasized by several studies [214, 230] in arterial EC, however, there exist several other candidates such as glycocalyx complexes on the plasma membrane [28], primary cilia [226], and numerous ion channels [23] that can mediate this signal. Although the baseline media (DMEM/F-12) used in this study was ATP-free, endogenous ATP release could still potentially stimulate P2X/2Y receptors. This work suggests that at least one HDLEC mechanosensor initiates a pathway resulting in ER store Ca^{2+} release followed by extracellular Ca^{2+} entry, however further experiments are necessary to identify the details of this pathway in

HDLEC. Commercial HDLEC lines are isolated in a manner in which we know they are lymphatic in origin though we cannot determine exactly which type of lymphatic vessels they represent. The HDLEC line used in this study contains a mixture of endothelial cells from collecting and capillary lymphatics in the human foreskin that is expected to exhibit heterogeneity in their response. These HDLECs have been used extensively by scientists in the field and thus represent a good example to allow comparisons with others work on lymphatic endothelium. Lastly, it is also not clear how cultured HDLEC may change *in vitro* under typical culture conditions, though this general approach has been broadly and effectively utilized to study BAEC.

In summary, because of well-defined sensitivities of lymphatic vessels *in vivo* and *in vitro* to flow/shear in terms of modulating lymphatic tone, lymph pumping and nitric oxide production, we evaluated the shear-sensitive changes in HDLEC cytoplasmic calcium. We measured $[Ca^{2+}]_i$ dynamics in cultured HDLEC in response to step changes in physiologically relevant shear stress and showed that the magnitude of the calcium rise is dependent on the magnitude of shear stress. Furthermore, we have identified specific calcium sources that contributed to this signal. We demonstrated that the intracellular calcium store release was mainly responsible for the peak observed after the shear started, whereas extracellular calcium entry contributed to the magnitude and duration of the calcium signal. Furthermore shear was not able to initiate the spike when the ER stores had been depleted. Further investigations are necessary to refine the mechanotransduction signalling pathway responsible for $[Ca^{2+}]_i$ sensitivity to shear in HDLEC.

CHAPTER 6

CONCLUSIONS AND FUTURE WORK

6.1. Conclusions

This thesis set out with the aim to examine the patterns of lymph transport in the LN (Chapter 2). The model developed here showed that under baseline (healthy) conditions, about 90% of the afferent lymph flowed through peripheral paths of the LNs in high velocities (mm/min), while smaller portion of the fluid slowly ($\mu\text{m}/\text{min}$) percolated through follicles and cortex. The percolated fluid is transported to blood vessels in homeostasis to assist the fluid balance role of the lymphatic system and is an often-neglected role of LN. With the help of parameter sensitivity analysis, surface area of the blood vessels was identified as an important parameter of the system that needs to be accurately measured. Our model supported the concept that the direction of the exchange flow with blood vessels could be changed depending on the hydrodynamic conditions in the node, notably blood pressure and oncotic pressures, which might play a role in the function of the LNs during infection and chronic inflammation.

Among the other parameters, the hydraulic conductivity of medulla appeared to be the main determinant of overall LN resistance and changes in this property further modulate lymph flow to cortical regions. To investigate the role of the medulla in more detail, a set of experiments was designed to measure LN resistance in healthy WT mice, which resulted in an indirect measurement of medulla hydraulic conductivity (Chapter 3). The resistance of the lymph node exhibited a dynamic behaviour that increased in 24 hr, while it decreased back to near baseline levels by 72 hr. Additionally, the computational model predicted that the dynamic increase in LN resistance with inflammation could only be explained by lowered hydraulic conductivity of medulla. From the results of Chapters 2 and 3 we conclude that flow properties including patterns of lymph distribution can dramatically change in LN,

which modulates antigen, cytokine, chemokine and immune cell transport to different regions, and likely play an important role in immune response and inflammation.

In Chapter 4, the model was applied further to include transport and reactions of two important chemokines (CCL19 and CCL21) that modulate immune cell homing to LN. CCL21 forms gradients in the interfollicular zone that trigger APC migration into the cortex, and further experiments showed that bound CCL21 concentrations were uniform in ACKR4 knockout mice. Based on the parallel observation that ACKR4 are only present on the SCS ceiling, it was concluded that scavenging by these cells is required for interfollicular gradient formation [19]. We combined our LN flow model with equations describing chemokine ligand receptor interactions to build a comprehensive model of CCL19 and CCL21 transport and gradient formation. Our results refine the previous hypothesis by suggesting that the lack of ACKR4 in the collecting lymphatic vessels (and correspondingly higher afferent CCL21 concentrations) is actually responsible for the observed gradient disruption, rather than the lack of ACKR4 on the ceiling of the LN capsule. Moreover, we showed that either ACKR4 or afferent flow is necessary for sustained gradients, which emphasizes the important role of flow in modulating concentration distributions. There are many inherent confounding factors in the experiments that are often difficult to isolate, hence limiting the conditions by which hypotheses can be tested. This platform can be utilized to examine hard-to-test hypotheses and can be adapted to study any chemokine or cytokine ligand-receptor axis.

Additionally we approached the fluid transport in lymphatics and LN from another angle by investigating shear mediated calcium response in LEC. Lymphatic vessels have shown well-defined sensitivities to flow/shear by modulating lymphatic tone, lymph pumping and nitric oxide production, which motivated us to evaluate the

shear-sensitive changes in HDLEC cytoplasmic calcium (Chapter 5). Measured $[Ca^{2+}]_i$ dynamics showed that calcium increase depends on the magnitude of shear stress, with contributions from both intracellular calcium store release and extracellular calcium entry. We further demonstrated that shear was not able to initiate the spike when the ER stores had been depleted, but more studies are necessary to refine the mechanotransduction signalling pathway responsible for $[Ca^{2+}]_i$ sensitivity to shear in LEC. Furthermore, the effect of shear stress on subcapsular sinus LECs with the shear profile quantified in Chapter 1 remains to be elucidated. Overall, this study serves as a foundation to study how shear stress, which can be modulated by inflammation and infection, affects LECs in LN and the upstream collecting lymphatic vessels.

These insights identify fluid and mass transport in the LN to be intertwined with inflammation and immune response and can serve as potential therapeutic targets. On one hand, flow could regulate gradients of key LN chemokines (CCL19 and CCL21) essential for adaptive immunity (Chapter 4). On the other hand, hydraulic resistance of LN was modulated with remodelling associated with inflammation (Chapter 3). Large molecules (> 70 kDa) and cells are predominantly transported from interstitial space to sinuses of LNs [78]. Thus, drug-loaded nanoparticles can target medullary sinuses to modify hydraulic conductivity with the aim to modulate immune response. Additionally, this work will help in development of artificial tissue-engineered LN by providing information about the essential flow features of the LN that needs to be included in the design. Moreover, our detailed examination of LN homing chemokines will serve as the groundwork for design and development of chemokine and cytokine-loaded injectable gel vaccines [244, 245]. These chemokine-loaded materials are showed to form structures that attract DCs to

activate them with inflammatory cytokines in the presence of desired antigen (can be tumour antigen) for inducing strong cellular immune response [244, 246].

6.2. Recommendations and Future Work

The work presented here addressed several questions about the fluid and mass transport in the LN. However as expected, learning more about the details of the system has revealed new issues and questions to be addressed.

What is the accurate blood vessel surface area and blood pressure distribution in the LN? In Chapter 2, fluid exchange between lymph and blood vessels was shown to be sensitive to surface area of the blood vessels, which was assumed to be homogeneously distributed in B and T cell regions, and was estimated from confocal microscopy images of optically cleared LN. However, it was not possible to segment the small capillaries, which include a great portion of total surface area of the blood vessels in the LN. This was due to the shrinkage of tissue and small size of the capillaries. Also, there was a clear drop in signal intensity deep in the sample that added extra hardship during segmentation. A LN blood vessel cast that could be scanned using a high-resolution micro computed tomography (μ CT) system can not only capture the surface area distribution of the vessels in LN, but also provide the information needed to estimate blood pressure distribution. Having the surface area density and blood pressure fields would improve the input parameters for Starling's Equation to calculate fluid exchange with blood vessels.

How does inclusion of conduit network affect LN flow? Is anisotropy a main determinant of the flow distribution? The conduit system of LN has been subject to more attention during the past few years [78, 115]. This interconnected network of alighted collagen bundles cover the porous regions and act as conduits for the fluid to shuttle through the LN. The computational model developed in Chapter 2 assumed isotropic material for these porous regions. More experimental studies are required to visualize and quantify the conduit network and characterize its properties and constituents to allow inclusion of this important component of LN fluid and mass transport. With the data available in the current literature, the conduits appear to be anisotropic and have the ability to change the direction of the path of least resistance in the porous regions of the LN.

Do any of the conclusions change if instead of idealized geometry, an image-based geometry was used? What are the main features that need to be extracted from the images to describe the LN for flow analysis? For all LN modelling work in this study, we developed an idealized geometry that had gone through an extensive iterative process with our immunologist collaborators to make sure it included all the important geometrical features of mouse popliteal LN. It is important to demonstrate if an image-based geometry of LN would have similar conclusions to the idealized geometry. Confocal microscopy of optically cleared tissue can be utilized to quantify antibody stained cellular regions of LN, but subsequent application into a computational mesh would require sophisticated image segmentation protocols. Additionally, preparation of samples often leads to shrinkage and collapse of subcapsular sinus (10-20 μm height). Certainly, the flow patterns will be significantly changed without the low resistance path through

subcapsular sinus. On the other hand, μ CT scanning of the phosphotungstic acid (PTA) stained LN can provide information on tissue density distribution. μ CT images are easier to segment being an inherent advantage of tomography techniques, but they lack the specific information accessible from antibody-staining and light microscopy. The height and boundary of subcapsular sinus, number and size of B cell follicles, boundary of medulla, number and location of afferent and efferent vessels, and the whole LN capsule boundary are the necessary parameters that need to be measurable from the images to be able to reconstruct a better representing geometry of the LN. In my opinion, a detailed segmentation of the sinuses connecting afferent vessel(s) through subcapsular sinus and medullary sinuses to efferent vessel(s) could be the most important geometrical feature in determining the most physiologic flow distribution model in LN.

Is it possible to experimentally confirm the role of medulla as the main regulator of LN resistance in the first 24 hr of inflammation? We hypothesized in Chapter 3 that lymphocyte entry and proliferation in LN paracortex pushes to the medulla to close (or reduce passageway diameters of) some of the sinuses and hence increase the resistance of the peripheral path. Unfortunately, there are no specific experimental data to support this hypothesis. Immunostaining for lymphatic endothelial cells (LYVE-1, PROX-1, or VEGFR3) on sections that pass through both afferent and efferent vessels (anteroposterior axis) may demonstrate if the sinuses shrink after inflammation. Furthermore, Measuring LN cellularity as well as wet weight (or volume) would allow us to compare cell-to-volume ratio to assess indirectly if there is shrinkage in the sinuses. Overall, the strength of the model is to

predict and suggest more probable hypotheses that can then be tested experimentally to better understand the system.

How do the afferent lymphatic vessels respond to the increased afterload? The increase in LN resistance results in a higher afterload on the pumping afferent lymphatic vessels. Although the resistance increase is temporary (it is reduced back down in 72 hr after inflammation), it can temporarily affect the pumping of the afferent lymphatic vessels. Isolated lymphatic vessel experiments with a downstream capillary tubing that have resistances close to healthy or inflamed LNs can simulate *in vivo* situation. Measurement of the diameters and/or flow can determine if the pumping behaviour of these vessels has changed. It is important to establish how the collecting vessels respond, because the contractile activity of afferent vessel determines the afferent flow, which is a boundary condition for the lymph node simulations.

Does inclusion of CXCL13 and its receptor (CXCR5) affect CCL19 and CCL21 gradients in the LN? Would chemokine cooperation play an important role during rapid inflammation-mediated lymphocyte entry? In addition to CCL19 and CCL21, CXCL13 is the other important homeostatic chemokine in the LN that is crucial for the formation of B cell follicles [89]. CXCL13 is mainly produced by follicular dendritic cells (FDCs, a LN stromal cell population) that are essential for B cell activation and survival [206]. Gradient of CXCL13 guides B cells that enter through HEVs toward B cell follicles [96, 204]. Furthermore, T follicular helper cells (T_{FH} cell) upregulate CXCR5, and migrate toward the B cell-T cell border to start germinal centre reaction [203, 247]. Moreover, CXCL13 like CCL21 can bind to

proteoglycans and form immobilized gradients on the extracellular matrix (ECM) [92]. More studies are necessary to address if there is any CCL21/CXCL13 cooperation in the LN [248]. An expansion of this question will be to investigate if there is any cooperation between CCL21 or CXCL13 and inflammatory chemokines such as CCL2 (that also binds to ECM) [249]. We can think about a hypothetical case where CCL21 (that binds in high concentrations to the ECM in LN) is mobilized when an inflammatory chemokine that can bind to the same ECM binding sites is washed to the LN. The incoming chemokine will replace some of bound CCL21 (depending on relative binding/unbinding rates) and leads to a rapid release of “reserved” CCL21 that will be transported by flow to the HEVs and can enhance T cell transmigration to the LN [9, 157]. Examination of chemokine cooperation is an interesting topic that can be well explored using the model developed here.

Can the models of chemokine dynamics be coupled to agent-based models of cellular motility and migration? Agent-based models (ABMs) use probabilistic rules to model cell motility and migration [116]. There have been models of T cell-dendritic cell interactions in LN to simulate T cell activation [118]. The rules of ABM can be improved to take into account the gradients of CCL19 and CCL21 (fluid and mass transport coupling to ABM). Additionally, ABM can simulate the change in cell number, LN size, and receptor expression changes during the time course of inflammation (or any other disease) that can be fed to the fluid and mass transport model to update the chemokine gradients. This coupling in three-dimensions would be the first model that couples the fluid and mass transport to popular ABM of T cell activation in LN.

Is ACKR4 expressed in greater degree in LECs of collecting lymphatic vessels versus initial lymphatic? Is ACKR4 modulated with shear stress? A recent study by our collaborators showed only 15-20% of total LECs in mouse ear and dorsal skin express ACKR4 [102]. This study used flow cytometry, so they could not separate the percentage of LECs from initial lymphatics versus collecting lymphatics. Initial LECs most likely do not express ACKR4, because gradients of CCL19 and CCL21 towards the initial lymphatics in the tissue are essential for DC migration out of the vessels [87]. However, our model showed that if a high concentration of chemokine (relative to K_D of ECM binding) enters the LN, it will abolish the gradient of bound CCL21 and hence a diminished immune response similar to ACKR4-deficient mice [19]. Therefore, a collecting lymphatic vessel ACKR4 that scavenges CCL19 and CCL21 ensures a high concentration in initials so that DCs can migrate toward them, and a low concentration in the afferent lymph to help stabilize the interfollicular gradients. Indeed, there exist other molecules with same pattern of expression. For instance, LYVE-1 is expressed by initial LECs while it is greatly downregulated in the collecting vessel LECs [250]. We hypothesize that ACKR4 expression on LECs is opposite to LYVE-1 expression patterns. To the best of author's knowledge, ACKR4 has not yet shown to be regulated by shear stress in lymphatic endothelium.

BIBLIOGRAPHY

- [1] Thomas, S. N., Rutkowski, J. M., Pasquier, M., Kuan, E. L., Alitalo, K., Randolph, G. J., and Swartz, M. A., 2012, "Impaired humoral immunity and tolerance in K14-VEGFR-3-Ig mice that lack dermal lymphatic drainage," *Journal of immunology* (Baltimore, Md. : 1950), 189(5), pp. 2181-2190.
- [2] Lund, A. W., Duraes, F. V., Hirosue, S., Raghavan, V. R., Nembrini, C., Thomas, S. N., Issa, A., Hugues, S., and Swartz, M. A., 2012, "VEGF-C promotes immune tolerance in B16 melanomas and cross-presentation of tumor antigen by lymph node lymphatics," *Cell reports*, 1(3), pp. 191-199.
- [3] Thomas, S. N., Vokali, E., Lund, A. W., Hubbell, J. A., and Swartz, M. A., 2014, "Targeting the tumor-draining lymph node with adjuvanted nanoparticles reshapes the anti-tumor immune response," *Biomaterials*, 35(2), pp. 814-824.
- [4] Jeanbart, L., Ballester, M., de Titta, A., Corthesy, P., Romero, P., Hubbell, J. A., and Swartz, M. A., 2014, "Enhancing efficacy of anticancer vaccines by targeted delivery to tumor-draining lymph nodes," *Cancer immunology research*, 2(5), pp. 436-447.
- [5] Liu, H., Moynihan, K. D., Zheng, Y., Szeto, G. L., Li, A. V., Huang, B., Van Egeren, D. S., Park, C., and Irvine, D. J., 2014, "Structure-based programming of lymph-node targeting in molecular vaccines," *Nature*, 507(7493), pp. 519-522.
- [6] Phan, T. G., Grigorova, I., Okada, T., and Cyster, J. G., 2007, "Subcapsular encounter and complement-dependent transport of immune complexes by lymph node B cells," *Nature immunology*, 8(9), pp. 992-1000.
- [7] Junt, T., Moseman, E. A., Iannacone, M., Massberg, S., Lang, P. A., Boes, M., Fink, K., Henrickson, S. E., Shayakhmetov, D. M., Di Paolo, N. C., van Rooijen, N., Mempel, T. R., Whelan, S. P., and von Andrian, U. H., 2007, "Subcapsular sinus macrophages in lymph nodes clear lymph-borne viruses and present them to antiviral B cells," *Nature*, 450(7166), pp. 110-114.
- [8] Carrasco, Y. R., and Batista, F. D., 2007, "B cells acquire particulate antigen in a macrophage-rich area at the boundary between the follicle and the subcapsular sinus of the lymph node," *Immunity*, 27(1), pp. 160-171.
- [9] Palframan, R. T., Jung, S., Cheng, G., Weninger, W., Luo, Y., Dorf, M., Littman, D. R., Rollins, B. J., Zwerink, H., Rot, A., and von Andrian, U. H., 2001, "Inflammatory chemokine transport and presentation in HEV: a remote control mechanism for monocyte recruitment to lymph nodes in inflamed tissues," *J Exp Med*, 194(9), pp. 1361-1373.
- [10] Nakano, H., Lin, K. L., Yanagita, M., Charbonneau, C., Cook, D. N., Kakiuchi, T., and Gunn, M. D., 2009, "Blood-derived inflammatory dendritic cells in lymph nodes stimulate acute T helper type 1 immune responses," *Nature immunology*, 10(4), pp. 394-402.

- [11] Kumar, V., Chyou, S., Stein, J. V., and Lu, T. T., 2012, "Optical projection tomography reveals dynamics of HEV growth after immunization with protein plus CFA and features shared with HEVs in acute autoinflammatory lymphadenopathy," *Frontiers in immunology*, 3, p. 282.
- [12] Girard, J. P., Moussion, C., and Forster, R., 2012, "HEVs, lymphatics and homeostatic immune cell trafficking in lymph nodes," *Nat Rev Immunol*, 12(11), pp. 762-773.
- [13] Tan, K. W., Yeo, K. P., Wong, F. H., Lim, H. Y., Khoo, K. L., Abastado, J. P., and Angeli, V., 2012, "Expansion of cortical and medullary sinuses restrains lymph node hypertrophy during prolonged inflammation," *Journal of immunology (Baltimore, Md. : 1950)*, 188(8), pp. 4065-4080.
- [14] Platt, A. M., and Randolph, G. J., 2013, "Dendritic cell migration through the lymphatic vasculature to lymph nodes," *Advances in immunology*, 120, pp. 51-68.
- [15] Schmidt, S., and Friedl, P., 2010, "Interstitial cell migration: integrin-dependent and alternative adhesion mechanisms," *Cell and tissue research*, 339(1), pp. 83-92.
- [16] Lammermann, T., Bader, B. L., Monkley, S. J., Worbs, T., Wedlich-Soldner, R., Hirsch, K., Keller, M., Forster, R., Critchley, D. R., Fassler, R., and Sixt, M., 2008, "Rapid leukocyte migration by integrin-independent flowing and squeezing," *Nature*, 453(7191), pp. 51-55.
- [17] Kuan, E. L., Ivanov, S., Bridenbaugh, E. A., Victora, G., Wang, W., Childs, E. W., Platt, A. M., Jakubzick, C. V., Mason, R. J., Gashev, A. A., Nussenzweig, M., Swartz, M. A., Dustin, M. L., Zawieja, D. C., and Randolph, G. J., 2015, "Collecting Lymphatic Vessel Permeability Facilitates Adipose Tissue Inflammation and Distribution of Antigen to Lymph Node-Homing Adipose Tissue Dendritic Cells," *Journal of immunology (Baltimore, Md. : 1950)*.
- [18] Tal, O., Lim, H. Y., Gurevich, I., Milo, I., Shipony, Z., Ng, L. G., Angeli, V., and Shakhar, G., 2011, "DC mobilization from the skin requires docking to immobilized CCL21 on lymphatic endothelium and intralymphatic crawling," *J Exp Med*, 208(10), pp. 2141-2153.
- [19] Ulvmar, M. H., Werth, K., Braun, A., Kelay, P., Hub, E., Eller, K., Chan, L., Lucas, B., Novitzky-Basso, I., Nakamura, K., Rulicke, T., Nibbs, R. J., Worbs, T., Forster, R., and Rot, A., 2014, "The atypical chemokine receptor CCRL1 shapes functional CCL21 gradients in lymph nodes," *Nature immunology*, 15(7), pp. 623-630.
- [20] McHale, N. G., and Roddie, I. C., 1976, "The effect of transmural pressure on pumping activity in isolated bovine lymphatic vessels," *The Journal of Physiology*, 261, pp. 255-269.
- [21] Koller, A., Mizuno, R., and Kaley, G., 1999, "Flow reduces the amplitude and increases the frequency of lymphatic vasomotion: role of endothelial prostanoids."
- [22] Ando, J., and Yamamoto, K., 2009, "Vascular Mechanobiology - Endothelial Cell Responses to Fluid Shear Stress.," *Circulation Journal*, 73(11), pp. 1983-1992.

- [23] Davies, P. F., 1995, "Flow-mediated endothelial mechanotransduction," *Physiol Rev*, 75(3), pp. 519-560.
- [24] Helmlinger, G., Berk, B. C., and Nerem, R. M., 1996, "Pulsatile and steady flow-induced calcium oscillations in single cultured endothelial cells," *J Vasc Res*, 33(5), pp. 360-369.
- [25] Warboys, C. M., Eric Berson, R., Mann, G. E., Pearson, J. D., and Weinberg, P. D., 2010, "Acute and chronic exposure to shear stress have opposite effects on endothelial permeability to macromolecules," *American journal of physiology. Heart and circulatory physiology*, 298(6), pp. H1850-1856.
- [26] Li, Y. S., Haga, J. H., and Chien, S., 2005, "Molecular basis of the effects of shear stress on vascular endothelial cells," *J Biomech*, 38(10), pp. 1949-1971.
- [27] Shen, J., Lusinskas, F. W., Connolly, A., Dewey, C. F., Jr., and Gimbrone, M. A., Jr., 1992, "Fluid shear stress modulates cytosolic free calcium in vascular endothelial cells," *The American journal of physiology*, 262(2 Pt 1), pp. C384-390.
- [28] Tarbell, J. M., and Ebong, E. E., 2008, "The endothelial glycocalyx: a mechanosensor and -transducer," *Sci Signal*, 1(40), p. pt8.
- [29] Tarbell, J. M., Weinbaum, S., and Kamm, R. D., 2005, "Cellular fluid mechanics and mechanotransduction," *Ann Biomed Eng*, 33(12), pp. 1719-1723.
- [30] Dixon, J. B., Greiner, S. T., Gashev, A. A., Cote, G. L., Moore, J. E., and Zawieja, D. C., 2006, "Lymph flow, shear stress, and lymphocyte velocity in rat mesenteric prenodal lymphatics," *Microcirculation*, 13(7), pp. 597-610.
- [31] Kawai, Y., Yokoyama, Y., Kaidoh, M., and Ohhashi, T., 2010, "Shear stress-induced ATP-mediated endothelial constitutive nitric oxide synthase expression in human lymphatic endothelial cells," *American journal of physiology. Cell physiology*, 298(3), pp. C647-655.
- [32] Rockson, S. G., 2010, "Causes and consequences of lymphatic disease," *Ann N Y Acad Sci*, 1207 Suppl 1, pp. E2-6.
- [33] Rockson, S. G., 2008, "Diagnosis and management of lymphatic vascular disease," *J Am Coll Cardiol*, 52(10), pp. 799-806.
- [34] Cooper, G., and Bagnall, A., 2016, "Prevalence of lymphoedema in the UK: focus on the southwest and West Midlands," *British journal of community nursing*, 21 Suppl 4, pp. S6-s14.
- [35] Zampell, J. C., Elhadad, S., Avraham, T., Weitman, E., Aschen, S., Yan, A., and Mehrara, B. J., 2012, "Toll-like receptor deficiency worsens inflammation and lymphedema after lymphatic injury," *American journal of physiology. Cell physiology*, 302(4), pp. C709-719.

- [36] Zampell, J. C., Yan, A., Avraham, T., Andrade, V., Malliaris, S., Aschen, S., Rockson, S. G., and Mehrara, B. J., 2011, "Temporal and spatial patterns of endogenous danger signal expression after wound healing and in response to lymphedema," *American journal of physiology. Cell physiology*, 300(5), pp. C1107-1121.
- [37] Angeli, V., Llodra, J., Rong, J. X., Satoh, K., Ishii, S., Shimizu, T., Fisher, E. A., and Randolph, G. J., 2004, "Dyslipidemia associated with atherosclerotic disease systemically alters dendritic cell mobilization," *Immunity*, 21(4), pp. 561-574.
- [38] Karpanen, T., and Alitalo, K., 2008, "Molecular biology and pathology of lymphangiogenesis," *Annual review of pathology*, 3, pp. 367-397.
- [39] Zawieja, S. D., Wang, W., Wu, X., Nepiyushchikh, Z. V., Zawieja, D. C., and Muthuchamy, M., 2012, "Impairments in the intrinsic contractility of mesenteric collecting lymphatics in a rat model of metabolic syndrome," *American journal of physiology. Heart and circulatory physiology*, 302(3), pp. H643-653.
- [40] Blum, K. S., Karaman, S., Proulx, S. T., Ochsenbein, A. M., Luciani, P., Leroux, J. C., Wolfrum, C., and Detmar, M., 2014, "Chronic high-fat diet impairs collecting lymphatic vessel function in mice," *PLoS One*, 9(4), p. e94713.
- [41] Weitman, E. S., Aschen, S. Z., Farias-Eisner, G., Albano, N., Cuzzone, D. A., Ghanta, S., Zampell, J. C., Thorek, D., and Mehrara, B. J., 2013, "Obesity impairs lymphatic fluid transport and dendritic cell migration to lymph nodes," *PLoS One*, 8(8), p. e70703.
- [42] Huang, L. H., Elvington, A., and Randolph, G. J., 2015, "The role of the lymphatic system in cholesterol transport," *Frontiers in pharmacology*, 6, p. 182.
- [43] Lim, H. Y., Rutkowski, J. M., Helft, J., Reddy, S. T., Swartz, M. A., Randolph, G. J., and Angeli, V., 2009, "Hypercholesterolemic mice exhibit lymphatic vessel dysfunction and degeneration," *Am J Pathol*, 175(3), pp. 1328-1337.
- [44] Lim, H. Y., Thiam, C. H., Yeo, K. P., Bisioendial, R., Hii, C. S., McGrath, K. C., Tan, K. W., Heather, A., Alexander, J. S., and Angeli, V., 2013, "Lymphatic vessels are essential for the removal of cholesterol from peripheral tissues by SR-BI-mediated transport of HDL," *Cell metabolism*, 17(5), pp. 671-684.
- [45] Martel, C., Li, W., Fulp, B., Platt, A. M., Gautier, E. L., Westerterp, M., Bittman, R., Tall, A. R., Chen, S. H., Thomas, M. J., Kreisel, D., Swartz, M. A., Sorci-Thomas, M. G., and Randolph, G. J., 2013, "Lymphatic vasculature mediates macrophage reverse cholesterol transport in mice," *Journal of Clinical Investigation*, 123(4), pp. 1571-1579.
- [46] Van Kruiningen, H. J., and Colombel, J. F., 2008, "The forgotten role of lymphangitis in Crohn's disease," *Gut*, 57(1), pp. 1-4.
- [47] Kovi, J., Duong, H. D., and Hoang, C. T., 1981, "Ultrastructure of intestinal lymphatics in Crohn's disease," *American journal of clinical pathology*, 76(4), pp. 385-394.

- [48] von der Weid, P. Y., and Rainey, K. J., 2010, "Review article: lymphatic system and associated adipose tissue in the development of inflammatory bowel disease," *Alimentary pharmacology & therapeutics*, 32(6), pp. 697-711.
- [49] Shields, J. D., Fleury, M. E., Yong, C., Tomei, A. A., Randolph, G. J., and Swartz, M. A., 2007, "Autologous chemotaxis as a mechanism of tumor cell homing to lymphatics via interstitial flow and autocrine CCR7 signaling," *Cancer Cell*, 11(6), pp. 526-538.
- [50] Steele, K. E., Anderson, A. O., and Mohamadzadeh, M., 2009, "Fibroblastic reticular cell infection by hemorrhagic fever viruses," *Immunotherapy*, 1(2), pp. 187-197.
- [51] Twenhafel, N. A., Mattix, M. E., Johnson, J. C., Robinson, C. G., Pratt, W. D., Cashman, K. A., Wahl-Jensen, V., Terry, C., Olinger, G. G., Hensley, L. E., and Honko, A. N., 2013, "Pathology of experimental aerosol Zaire ebolavirus infection in rhesus macaques," *Veterinary pathology*, 50(3), pp. 514-529.
- [52] Steele, K. E., Anderson, A. O., and Mohamadzadeh, M., 2009, "Fibroblastic reticular cells and their role in viral hemorrhagic fevers," *Expert review of anti-infective therapy*, 7(4), pp. 423-435.
- [53] Zeng, M., Smith, A. J., Wietgreffe, S. W., Southern, P. J., Schacker, T. W., Reilly, C. S., Estes, J. D., Burton, G. F., Silvestri, G., Lifson, J. D., Carlis, J. V., and Haase, A. T., 2011, "Cumulative mechanisms of lymphoid tissue fibrosis and T cell depletion in HIV-1 and SIV infections," *Journal of Clinical Investigation*, 121(3), pp. 998-1008.
- [54] Estes, J., Baker, J. V., Brenchley, J. M., Khoruts, A., Barthold, J. L., Bantle, A., Reilly, C. S., Beilman, G. J., George, M. E., Douek, D. C., Haase, A. T., and Schacker, T. W., 2008, "Collagen deposition limits immune reconstitution in the gut," *The Journal of infectious diseases*, 198(4), pp. 456-464.
- [55] Estes, J. D., Reilly, C., Trubey, C. M., Fletcher, C. V., Cory, T. J., Piatak, M., Jr., Russ, S., Anderson, J., Reimann, T. G., Star, R., Smith, A., Tracy, R. P., Berglund, A., Schmidt, T., Coalter, V., Chertova, E., Smedley, J., Haase, A. T., Lifson, J. D., and Schacker, T. W., 2015, "Antifibrotic therapy in simian immunodeficiency virus infection preserves CD4+ T-cell populations and improves immune reconstitution with antiretroviral therapy," *The Journal of infectious diseases*, 211(5), pp. 744-754.
- [56] Aspelund, A., Antila, S., Proulx, S. T., Karlsen, T. V., Karaman, S., Detmar, M., Wiig, H., and Alitalo, K., 2015, "A dural lymphatic vascular system that drains brain interstitial fluid and macromolecules," *J Exp Med*, 212(7), pp. 991-999.
- [57] Louveau, A., Smirnov, I., Keyes, T. J., Eccles, J. D., Rouhani, S. J., Peske, J. D., Derecki, N. C., Castle, D., Mandell, J. W., Lee, K. S., Harris, T. H., and Kipnis, J., 2015, "Structural and functional features of central nervous system lymphatic vessels," *Nature*, 523(7560), pp. 337-341.
- [58] Levick, J. R., and Michel, C. C., 2010, "Microvascular fluid exchange and the revised Starling principle," *Cardiovasc Res*, 87(2), pp. 198-210.

- [59] Schmid-Schonbein, G. W., 1990, "Microlymphatics and lymph flow," *Physiol Rev*, 70(4), pp. 987-1028.
- [60] Li, B., Silver, I., Szalai, J. P., and Johnston, M. G., 1998, "Pressure-volume relationships in sheep mesenteric lymphatic vessels in situ: response to hypovolemia," *Microvasc Res*, 56(2), pp. 127-138.
- [61] Ushiki, T., 1990, "The three-dimensional organization and ultrastructure of lymphatics in the rat intestinal mucosa as revealed by scanning electron microscopy after KOH-collagenase treatment," *Arch Histol Cytol*, 53 Suppl, pp. 127-136.
- [62] Fischer, M., Franzeck, U. K., Herrig, I., Costanzo, U., Wen, S., Schiesser, M., Hoffmann, U., and Bollinger, A., 1996, "Flow velocity of single lymphatic capillaries in human skin," *American Journal of Physiology - Heart and Circulatory Physiology*, 270(1), pp. H358-H363.
- [63] Zweifach, B. W., and Prather, J. W., 1975, "Micromanipulation of pressure in terminal lymphatics in the mesentery," *The American journal of physiology*, 228(5), pp. 1326-1335.
- [64] Breslin, J. W., 2014, "Mechanical forces and lymphatic transport," *Microvasc Res*, 96, pp. 46-54.
- [65] Baluk, P., Fuxe, J., Hashizume, H., Romano, T., Lashnits, E., Butz, S., Vestweber, D., Corada, M., Molendini, C., Dejana, E., and McDonald, D. M., 2007, "Functionally specialized junctions between endothelial cells of lymphatic vessels," *J Exp Med*, 204(10), pp. 2349-2362.
- [66] Gannon, B. J., and Carati, C. J., 2003, "Endothelial distribution of the membrane water channel molecule aquaporin-1: implications for tissue and lymph fluid physiology?," *Lymphat Res Biol*, 1(1), pp. 55-66.
- [67] Trzewik, J., Mallipattu, S. K., Artmann, G. M., Delano, F. A., and Schmid-Schonbein, G. W., 2001, "Evidence for a second valve system in lymphatics: endothelial microvalves," *FASEB journal : official publication of the Federation of American Societies for Experimental Biology*, 15(10), pp. 1711-1717.
- [68] Lynch, P. M., Delano, F. A., and Schmid-Schonbein, G. W., 2007, "The primary valves in the initial lymphatics during inflammation," *Lymphat Res Biol*, 5(1), pp. 3-10.
- [69] Zawieja, D. C., von der Weid, P. Y., and Gashev, A. A., 2011, "Microlymphatic Biology.," *Comprehensive Physiology*, . pp. 125–158.
- [70] von der Weid, P. Y., and Zawieja, D. C., 2004, "Lymphatic smooth muscle: the motor unit of lymph drainage," *Int J Biochem Cell Biol*, 36(7), pp. 1147-1153.
- [71] Zawieja, D. C., 2009, "Contractile physiology of lymphatics," *Lymphat Res Biol*, 7(2), pp. 87-96.

- [72] Kislitsyn, A., Savinkov, R., Novkovic, M., Onder, L., and Bocharov, G., 2015, "Computational Approach to 3D Modeling of the Lymph Node Geometry," *Computation*, 3(2), p. 222.
- [73] Kumar, V., Scandella, E., Danuser, R., Onder, L., Nitschke, M., Fukui, Y., Halin, C., Ludewig, B., and Stein, J. V., 2010, "Global lymphoid tissue remodeling during a viral infection is orchestrated by a B cell-lymphotoxin-dependent pathway," *Blood*, 115(23), pp. 4725-4733.
- [74] Comerford, I., Harata-Lee, Y., Bunting, M. D., Gregor, C., Kara, E. E., and McColl, S. R., 2013, "A myriad of functions and complex regulation of the CCR7/CCL19/CCL21 chemokine axis in the adaptive immune system," *Cytokine & growth factor reviews*, 24(3), pp. 269-283.
- [75] Ohtani, O., and Ohtani, Y., 2008, "Structure and function of rat lymph nodes," *Archives of Histology and Cytology*, 71(2), pp. 69-76.
- [76] Das, S., Sarrou, E., Podgrabinska, S., Cassella, M., Mungamuri, S. K., Feirt, N., Gordon, R., Nagi, C. S., Wang, Y., Entenberg, D., Condeelis, J., and Skobe, M., 2013, "Tumor cell entry into the lymph node is controlled by CCL1 chemokine expressed by lymph node lymphatic sinuses," *J Exp Med*, 210(8), pp. 1509-1528.
- [77] Woodruff, M. C., Herndon, C. N., Heesters, B. A., and Carroll, M. C., 2013, "Contextual Analysis of Immunological Response through Whole-Organ Fluorescent Imaging," *Lymphatic Research and Biology*, 11(3), pp. 121-127.
- [78] Roozendaal, R., Mempel, T. R., Pitcher, L. A., Gonzalez, S. F., Verschoor, A., Mebius, R. E., von Andrian, U. H., and Carroll, M. C., 2009, "Conduits mediate transport of low-molecular-weight antigen to lymph node follicles," *Immunity*, 30(2), pp. 264-276.
- [79] Gretz, J. E., Norbury, C. C., Anderson, A. O., Proudfoot, A. E., and Shaw, S., 2000, "Lymph-borne chemokines and other low molecular weight molecules reach high endothelial venules via specialized conduits while a functional barrier limits access to the lymphocyte microenvironments in lymph node cortex," *J Exp Med*, 192(10), pp. 1425-1440.
- [80] Kelch, I. D., Bogle, G., Sands, G. B., Phillips, A. R., LeGrice, I. J., and Dunbar, P. R., 2015, "Organ-wide 3D-imaging and topological analysis of the continuous microvascular network in a murine lymph node," *Scientific reports*, 5, p. 16534.
- [81] Gonzalez, S. F., Degn, S. E., Pitcher, L. A., Woodruff, M., Heesters, B. A., and Carroll, M. C., 2011, "Trafficking of B cell antigen in lymph nodes," *Annual review of immunology*, 29, pp. 215-233.
- [82] Truskey, G. A., Yuan, F., and Katz, D. F., 2004, *Transport phenomena in biological systems*, Pearson/Prentice Hall, Upper Saddle River, N.J.
- [83] Sokol, C. L., and Luster, A. D., 2015, "The chemokine system in innate immunity," *Cold Spring Harb Perspect Biol*, 7(5).

- [84] Griffith, J. W., Sokol, C. L., and Luster, A. D., 2014, "Chemokines and chemokine receptors: positioning cells for host defense and immunity," *Annual review of immunology*, 32, pp. 659-702.
- [85] Sallusto, F., Lenig, D., Forster, R., Lipp, M., and Lanzavecchia, A., 1999, "Two subsets of memory T lymphocytes with distinct homing potentials and effector functions," *Nature*, 401(6754), pp. 708-712.
- [86] Yoshida, R., Nagira, M., Kitaura, M., Imagawa, N., Imai, T., and Yoshie, O., 1998, "Secondary lymphoid-tissue chemokine is a functional ligand for the CC chemokine receptor CCR7," *The Journal of biological chemistry*, 273(12), pp. 7118-7122.
- [87] Weber, M., Hauschild, R., Schwarz, J., Moussion, C., de Vries, I., Legler, D. F., Luther, S. A., Bollenbach, T., and Sixt, M., 2013, "Interstitial dendritic cell guidance by haptotactic chemokine gradients," *Science (New York, N.Y.)*, 339(6117), pp. 328-332.
- [88] Nibbs, R. J., and Graham, G. J., 2013, "Immune regulation by atypical chemokine receptors," *Nat Rev Immunol*, 13(11), pp. 815-829.
- [89] von Andrian, U. H., and Mempel, T. R., 2003, "Homing and cellular traffic in lymph nodes," *Nat Rev Immunol*, 3(11), pp. 867-878.
- [90] Hirose, J., Kawashima, H., Yoshie, O., Tashiro, K., and Miyasaka, M., 2001, "Versican interacts with chemokines and modulates cellular responses," *The Journal of biological chemistry*, 276(7), pp. 5228-5234.
- [91] Hirose, J., Kawashima, H., Swope Willis, M., Springer, T. A., Hasegawa, H., Yoshie, O., and Miyasaka, M., 2002, "Chondroitin sulfate B exerts its inhibitory effect on secondary lymphoid tissue chemokine (SLC) by binding to the C-terminus of SLC," *Biochimica et biophysica acta*, 1571(3), pp. 219-224.
- [92] de Paz, J. L., Moseman, E. A., Noti, C., Polito, L., von Andrian, U. H., and Seeberger, P. H., 2007, "Profiling heparin-chemokine interactions using synthetic tools," *ACS chemical biology*, 2(11), pp. 735-744.
- [93] Patel, D. D., Koopmann, W., Imai, T., Whichard, L. P., Yoshie, O., and Krangel, M. S., 2001, "Chemokines have diverse abilities to form solid phase gradients," *Clinical immunology (Orlando, Fla.)*, 99(1), pp. 43-52.
- [94] Yang, B. G., Tanaka, T., Jang, M. H., Bai, Z., Hayasaka, H., and Miyasaka, M., 2007, "Binding of lymphoid chemokines to collagen IV that accumulates in the basal lamina of high endothelial venules: its implications in lymphocyte trafficking," *Journal of immunology (Baltimore, Md. : 1950)*, 179(7), pp. 4376-4382.
- [95] Schumann, K., Lammermann, T., Bruckner, M., Legler, D. F., Polleux, J., Spatz, J. P., Schuler, G., Forster, R., Lutz, M. B., Sorokin, L., and Sixt, M., 2010, "Immobilized chemokine fields and soluble chemokine gradients cooperatively shape migration patterns of dendritic cells," *Immunity*, 32(5), pp. 703-713.

- [96] Reif, K., Ekland, E. H., Ohl, L., Nakano, H., Lipp, M., Forster, R., and Cyster, J. G., 2002, "Balanced responsiveness to chemoattractants from adjacent zones determines B-cell position," *Nature*, 416(6876), pp. 94-99.
- [97] Szanya, V., Ermann, J., Taylor, C., Holness, C., and Fathman, C. G., 2002, "The subpopulation of CD4+CD25+ splenocytes that delays adoptive transfer of diabetes expresses L-selectin and high levels of CCR7," *Journal of immunology (Baltimore, Md. : 1950)*, 169(5), pp. 2461-2465.
- [98] Ohl, L., Mohaupt, M., Czeloth, N., Hintzen, G., Kiafard, Z., Zwirner, J., Blankenstein, T., Henning, G., and Forster, R., 2004, "CCR7 governs skin dendritic cell migration under inflammatory and steady-state conditions," *Immunity*, 21(2), pp. 279-288.
- [99] Forster, R., Davalos-Miszlitz, A. C., and Rot, A., 2008, "CCR7 and its ligands: balancing immunity and tolerance," *Nat Rev Immunol*, 8(5), pp. 362-371.
- [100] Heng, T. S., and Painter, M. W., 2008, "The Immunological Genome Project: networks of gene expression in immune cells," *Nature immunology*, 9(10), pp. 1091-1094.
- [101] Comerford, I., Milasta, S., Morrow, V., Milligan, G., and Nibbs, R., 2006, "The chemokine receptor CCX-CKR mediates effective scavenging of CCL19 in vitro," *European journal of immunology*, 36(7), pp. 1904-1916.
- [102] Bryce, S. A., Wilson, R. A., Tiplady, E. M., Asquith, D. L., Bromley, S. K., Luster, A. D., Graham, G. J., and Nibbs, R. J., 2016, "ACKR4 on Stromal Cells Scavenges CCL19 To Enable CCR7-Dependent Trafficking of APCs from Inflamed Skin to Lymph Nodes," *Journal of immunology (Baltimore, Md. : 1950)*, 196(8), pp. 3341-3353.
- [103] Glynn, P., Unudurthi, S. D., and Hund, T. J., 2014, "Mathematical modeling of physiological systems: An essential tool for discovery," *Life Sci*, 111(1-2), pp. 1-5.
- [104] Mirsky, H. P., Miller, M. J., Linderman, J. J., and Kirschner, D. E., 2011, "Systems biology approaches for understanding cellular mechanisms of immunity in lymph nodes during infection," *Journal of Theoretical Biology*, 287(0), pp. 160-170.
- [105] Kirschner, D. E., and Linderman, J. J., 2009, "Mathematical and computational approaches can complement experimental studies of host-pathogen interactions," *Cellular microbiology*, 11(4), pp. 531-539.
- [106] Bailey, J. E., 1998, "Mathematical modeling and analysis in biochemical engineering: past accomplishments and future opportunities," *Biotechnology progress*, 14(1), pp. 8-20.
- [107] Walpole, J., Papin, J. A., and Peirce, S. M., 2013, "Multiscale computational models of complex biological systems," *Annual review of biomedical engineering*, 15, pp. 137-154.
- [108] Jamalian, S., Bertram, C. D., Richardson, W. J., and Moore, J. E., Jr., 2013, "Parameter sensitivity analysis of a lumped-parameter model of a chain of lymphangions in series," *American journal of physiology. Heart and circulatory physiology*, 305(12), pp. H1709-1717.

- [109] Jamalian, S., Davis, M. J., Zawieja, D. C., and Moore, J. E., Jr., 2016, "Network Scale Modeling of Lymph Transport and Its Effective Pumping Parameters," *PLoS One*, 11(2), p. e0148384.
- [110] Wilson, J. T., van Loon, R., Wang, W., Zawieja, D. C., and Moore, J. E., Jr., 2015, "Determining the combined effect of the lymphatic valve leaflets and sinus on resistance to forward flow," *J Biomech*, 48(13), pp. 3584-3590.
- [111] Wilson, J. T., Wang, W., Hellerstedt, A. H., Zawieja, D. C., and Moore, J. E., 2013, "Confocal Image-Based Computational Modeling of Nitric Oxide Transport in a Rat Mesenteric Lymphatic Vessel," *Journal of Biomechanical Engineering*, 135(5), pp. 051005-051005.
- [112] Bocharov, G., Danilov, A., Vassilevski, Y., Marchuk, G. I., Chereshev, V. A., and Ludewig, B., 2011, "Reaction-Diffusion Modelling of Interferon Distribution in Secondary Lymphoid Organs," *Mathematical Modelling of Natural Phenomena*, 6(07), pp. 13-26.
- [113] Cooper, L. J., Heppell, J. P., Clough, G. F., Ganapathisubramani, B., and Roose, T., 2016, "An Image-Based Model of Fluid Flow Through Lymph Nodes," *Bulletin of mathematical biology*, 78(1), pp. 52-71.
- [114] Jafarnejad, M., Woodruff, M. C., Zawieja, D. C., Carroll, M. C., and Moore, J. E., Jr., 2015, "Modeling Lymph Flow and Fluid Exchange with Blood Vessels in Lymph Nodes," *Lymphat Res Biol*, 13(4), pp. 234-247.
- [115] Rantakari, P., Auvinen, K., Jappinen, N., Kapraali, M., Valtonen, J., Karikoski, M., Gerke, H., Iftakhar, E. K. I., Keuschnigg, J., Umemoto, E., Tohya, K., Miyasaka, M., Elima, K., Jalkanen, S., and Salmi, M., 2015, "The endothelial protein PLVAP in lymphatics controls the entry of lymphocytes and antigens into lymph nodes," *Nature immunology*, 16(4), pp. 386-396.
- [116] Mirsky, H. P., Miller, M. J., Linderman, J. J., and Kirschner, D. E., 2011, "Systems biology approaches for understanding cellular mechanisms of immunity in lymph nodes during infection," *J Theor Biol*, 287, pp. 160-170.
- [117] Vroomans, R. M., Maree, A. F., de Boer, R. J., and Beltman, J. B., 2012, "Chemotactic migration of T cells towards dendritic cells promotes the detection of rare antigens," *PLoS computational biology*, 8(11), p. e1002763.
- [118] Bogle, G., and Dunbar, P. R., 2012, "On-Lattice Simulation of T Cell Motility, Chemotaxis, and Trafficking in the Lymph Node Paracortex," *PLoS ONE*, 7(9), p. e45258.
- [119] Heath, T. J., Kerlin, R. L., and Spalding, H. J., 1986, "Afferent pathways of lymph flow within the popliteal node in sheep," *J Anat*, 149, pp. 65-75.
- [120] Fossum, S., 1980, "The architecture of rat lymph nodes. IV. Distribution of ferritin and colloidal carbon in the draining lymph nodes after foot-pad injection," *Scandinavian journal of immunology*, 12(5), pp. 433-441.

- [121] Roozendaal, R., Mebius, R. E., and Kraal, G., 2008, "The conduit system of the lymph node," *International immunology*, 20(12), pp. 1483-1487.
- [122] Steer, H. W., and Foot, R. A., 1987, "Changes in the medulla of the parathyroid lymph nodes of the rat during acute gastro-intestinal inflammation," *J Anat*, 152, pp. 23-36.
- [123] Gonzalez, S. F., Kuligowski, M. P., Pitcher, L. A., Roozendaal, R., and Carroll, M. C., 2010, "The role of innate immunity in B cell acquisition of antigen within LNs," *Advances in immunology*, 106, pp. 1-19.
- [124] Adair, T. H., and Guyton, A. C., 1983, "Modification of lymph by lymph nodes. II. Effect of increased lymph node venous blood pressure," *The American journal of physiology*, 245(4), pp. H616-622.
- [125] Adair, T. H., and Guyton, A. C., 1985, "Modification of lymph by lymph nodes. III. Effect of increased lymph hydrostatic pressure," *The American journal of physiology*, 249(4 Pt 2), pp. H777-782.
- [126] Lammermann, T., and Sixt, M., 2008, "The microanatomy of T-cell responses," *Immunological reviews*, 221, pp. 26-43.
- [127] Anderson, J., 1995, *Computational Fluid Dynamics*, McGraw-Hill Science/Engineering/Math.
- [128] Aukland, K., and Reed, R. K., 1993, "Interstitial-lymphatic mechanisms in the control of extracellular fluid volume," *Physiol Rev*, 73(1), pp. 1-78.
- [129] Hama, H., Kurokawa, H., Kawano, H., Ando, R., Shimogori, T., Noda, H., Fukami, K., Sakaue-Sawano, A., and Miyawaki, A., 2011, "Scale: a chemical approach for fluorescence imaging and reconstruction of transparent mouse brain," *Nature neuroscience*, 14(11), pp. 1481-1488.
- [130] Swartz, M. A., and Fleury, M. E., 2007, "Interstitial flow and its effects in soft tissues," *Annual review of biomedical engineering*, 9, pp. 229-256.
- [131] Jain, R. K., Tong, R. T., and Munn, L. L., 2007, "Effect of Vascular Normalization by Antiangiogenic Therapy on Interstitial Hypertension, Peritumor Edema, and Lymphatic Metastasis: Insights from a Mathematical Model," *Cancer Research*, 67(6), pp. 2729-2735.
- [132] Boucher, Y., Brekken, C., Netti, P. A., Baxter, L. T., and Jain, R. K., 1998, "Intratumoral infusion of fluid: estimation of hydraulic conductivity and implications for the delivery of therapeutic agents," *British journal of cancer*, 78(11), pp. 1442-1448.
- [133] Adamson, R. H., Sarai, R. K., Altangerel, A., Clark, J. F., Weinbaum, S., and Curry, F. E., 2013, "Microvascular permeability to water is independent of shear stress, but dependent on flow direction," *American journal of physiology. Heart and circulatory physiology*, 304(8), pp. H1077-1084.

- [134] Sill, H. W., Chang, Y. S., Artman, J. R., Frangos, J. A., Hollis, T. M., and Tarbell, J. M., 1995, "Shear stress increases hydraulic conductivity of cultured endothelial monolayers," *The American journal of physiology*, 268(2 Pt 2), pp. H535-543.
- [135] Zawieja, D. C., and Barber, B. J., 1987, "Lymph protein concentration in initial and collecting lymphatics of the rat," *The American journal of physiology*, 252(5 Pt 1), pp. G602-606.
- [136] Zaias, J., Mineau, M., Cray, C., Yoon, D., and Altman, N. H., 2009, "Reference values for serum proteins of common laboratory rodent strains," *Journal of the American Association for Laboratory Animal Science : JAALAS*, 48(4), pp. 387-390.
- [137] Adair, T. H., Moffatt, D. S., Paulsen, A. W., and Guyton, A. C., 1982, "Quantitation of changes in lymph protein concentration during lymph node transit," *The American journal of physiology*, 243(3), pp. H351-359.
- [138] Moore, J. E., Jr., Xu, C., Glagov, S., Zarins, C. K., and Ku, D. N., 1994, "Fluid wall shear stress measurements in a model of the human abdominal aorta: oscillatory behavior and relationship to atherosclerosis," *Atherosclerosis*, 110(2), pp. 225-240.
- [139] Nibbs, R. J., Kriehuber, E., Ponath, P. D., Parent, D., Qin, S., Campbell, J. D., Henderson, A., Kerjaschki, D., Maurer, D., Graham, G. J., and Rot, A., 2001, "The beta-chemokine receptor D6 is expressed by lymphatic endothelium and a subset of vascular tumors," *Am J Pathol*, 158(3), pp. 867-877.
- [140] Knox, P., and Pflug, J. J., 1983, "The effect of the canine popliteal node on the composition of lymph," *J Physiol*, 345, pp. 1-14.
- [141] Nagai, T., Ikomi, F., Suzuki, S., and Ohhashi, T., 2008, "In situ lymph dynamic characterization through lymph nodes in rabbit hind leg: special reference to nodal inflammation," *The journal of physiological sciences : JPS*, 58(2), pp. 123-132.
- [142] Tomei, A. A., Siegert, S., Britschgi, M. R., Luther, S. A., and Swartz, M. A., 2009, "Fluid flow regulates stromal cell organization and CCL21 expression in a tissue-engineered lymph node microenvironment," *Journal of immunology (Baltimore, Md. : 1950)*, 183(7), pp. 4273-4283.
- [143] Grigorova, I. L., Schwab, S. R., Phan, T. G., Pham, T. H., Okada, T., and Cyster, J. G., 2009, "Cortical sinus probing, S1P1-dependent entry and flow-based capture of egressing T cells," *Nature immunology*, 10(1), pp. 58-65.
- [144] Bouta, E. M., Wood, R. W., Brown, E. B., Rahimi, H., Ritchlin, C. T., and Schwarz, E. M., 2014, "In vivo quantification of lymph viscosity and pressure in lymphatic vessels and draining lymph nodes of arthritic joints in mice," *J Physiol*, 592(Pt 6), pp. 1213-1223.
- [145] Quin, J. W., and Shannon, A. D., 1977, "The influence of the lymph node on the protein concentration of efferent lymph leaving the node," *J Physiol*, 264(2), pp. 307-321.

- [146] Ushiki, T., Ohtani, O., and Abe, K., 1995, "Scanning electron microscopic studies of reticular framework in the rat mesenteric lymph node," *The Anatomical record*, 241(1), pp. 113-122.
- [147] Hudack, S., and McMaster, P. D., 1932, "I. The permeability of the wall of the lymphatic capillary," *The Journal of Experimental Medicine*, 56(2), pp. 223-238.
- [148] Sainte-Marie, G., Peng, F. S., and Belisle, C., 1982, "Overall architecture and pattern of lymph flow in the rat lymph node," *The American journal of anatomy*, 164(4), pp. 275-309.
- [149] Hendriks, H. R., and Eestermans, I. L., 1983, "Disappearance and reappearance of high endothelial venules and immigrating lymphocytes in lymph nodes deprived of afferent lymphatic vessels: a possible regulatory role of macrophages in lymphocyte migration," *European journal of immunology*, 13(8), pp. 663-669.
- [150] Lee, J. W., Epardaud, M., Sun, J., Becker, J. E., Cheng, A. C., Yonekura, A. R., Heath, J. K., and Turley, S. J., 2007, "Peripheral antigen display by lymph node stroma promotes T cell tolerance to intestinal self," *Nature immunology*, 8(2), pp. 181-190.
- [151] Platt, A. M., Rutkowski, J. M., Martel, C., Kuan, E. L., Ivanov, S., Swartz, M. A., and Randolph, G. J., 2013, "Normal dendritic cell mobilization to lymph nodes under conditions of severe lymphatic hypoplasia," *Journal of immunology (Baltimore, Md. : 1950)*, 190(9), pp. 4608-4620.
- [152] Hughes, G. A., and Allen, J. M., 1993, "Neural modulation of bovine mesenteric lymph node contraction," *Experimental physiology*, 78(5), pp. 663-674.
- [153] Thornbury, K. D., McHale, N. G., Allen, J. M., and Hughes, G., 1990, "Nerve-mediated contractions of sheep mesenteric lymph node capsules," *J Physiol*, 422, pp. 513-522.
- [154] Tumer, A., Ozturk-Demir, N., Basar-Eroglu, C., and Noyan, A., 1983, "Spontaneous contractions and stretch-evoked responses of isolated lymph nodes," *Journal of muscle research and cell motility*, 4(1), pp. 103-113.
- [155] Lee, J. S., 1986, "Lymph pressure in rat intestinal lymph duct with lymphatic obstruction," *The American journal of physiology*, 251(3 Pt 1), pp. G321-325.
- [156] Rohner, N. A., McClain, J., Tuell, S. L., Warner, A., Smith, B., Yun, Y., Mohan, A., Sushnitha, M., and Thomas, S. N., 2015, "Lymph node biophysical remodeling is associated with melanoma lymphatic drainage," *FASEB journal : official publication of the Federation of American Societies for Experimental Biology*, 29(11), pp. 4512-4522.
- [157] Baekkevold, E. S., Yamanaka, T., Palframan, R. T., Carlsen, H. S., Reinholt, F. P., von Andrian, U. H., Brandtzaeg, P., and Haraldsen, G., 2001, "The CCR7 ligand elc (CCL19) is transcytosed in high endothelial venules and mediates T cell recruitment," *J Exp Med*, 193(9), pp. 1105-1112.

- [158] Mempel, T. R., Henrickson, S. E., and Von Andrian, U. H., 2004, "T-cell priming by dendritic cells in lymph nodes occurs in three distinct phases," *Nature*, 427(6970), pp. 154-159.
- [159] Langenkamp, A., Casorati, G., Garavaglia, C., Dellabona, P., Lanzavecchia, A., and Sallusto, F., 2002, "T cell priming by dendritic cells: thresholds for proliferation, differentiation and death and intraclonal functional diversification," *European journal of immunology*, 32(7), pp. 2046-2054.
- [160] Webster, B., Ekland, E. H., Agle, L. M., Chyou, S., Ruggieri, R., and Lu, T. T., 2006, "Regulation of lymph node vascular growth by dendritic cells," *J Exp Med*, 203(8), pp. 1903-1913.
- [161] Soderberg, K. A., Payne, G. W., Sato, A., Medzhitov, R., Segal, S. S., and Iwasaki, A., 2005, "Innate control of adaptive immunity via remodeling of lymph node feed arteriole," *Proc Natl Acad Sci U S A*, 102(45), pp. 16315-16320.
- [162] Randolph, G. J., Angeli, V., and Swartz, M. A., 2005, "Dendritic-cell trafficking to lymph nodes through lymphatic vessels," *Nat Rev Immunol*, 5(8), pp. 617-628.
- [163] Katakai, T., Hara, T., Sugai, M., Gonda, H., and Shimizu, A., 2004, "Lymph node fibroblastic reticular cells construct the stromal reticulum via contact with lymphocytes," *J Exp Med*, 200(6), pp. 783-795.
- [164] Scandella, E., Bolinger, B., Lattmann, E., Miller, S., Favre, S., Littman, D. R., Finke, D., Luther, S. A., Junt, T., and Ludewig, B., 2008, "Restoration of lymphoid organ integrity through the interaction of lymphoid tissue-inducer cells with stroma of the T cell zone," *Nature immunology*, 9(6), pp. 667-675.
- [165] Browse, N. L., Doig, R. L., and Sizeland, D., 1984, "The resistance of a lymph node to lymph flow," *The British journal of surgery*, 71(3), pp. 192-196.
- [166] Papp, M., Makara, G. B., and Hajtman, B., 1971, "The resistance of in situ perfused lymph trunks and lymph nodes to flow," *Experientia*, 27(4), pp. 391-392.
- [167] Scallan, J. P., and Davis, M. J., 2013, "Genetic removal of basal nitric oxide enhances contractile activity in isolated murine collecting lymphatic vessels," *The Journal of Physiology*, 591(Pt 8), pp. 2139-2156.
- [168] Takedachi, M., Qu, D., Ebisuno, Y., Oohara, H., Joachims, M. L., McGee, S. T., Maeda, E., McEver, R. P., Tanaka, T., Miyasaka, M., Murakami, S., Krahn, T., Blackburn, M. R., and Thompson, L. F., 2008, "CD73-generated adenosine restricts lymphocyte migration into draining lymph nodes," *Journal of immunology (Baltimore, Md. : 1950)*, 180(9), pp. 6288-6296.
- [169] Delgado, M. F., Coviello, S., Monsalvo, A. C., Melendi, G. A., Hernandez, J. Z., Batalle, J. P., Diaz, L., Trento, A., Chang, H. Y., Mitzner, W., Ravetch, J., Melero, J. A., Irusta, P. M., and Polack, F. P., 2009, "Lack of antibody affinity maturation due to poor Toll-like receptor stimulation leads to enhanced respiratory syncytial virus disease," *Nat Med*, 15(1), pp. 34-41.

- [170] Uchida, T., Scumpia, P. O., Murasko, D. M., Seki, S., Woulfe, S., Clare-Salzler, M. J., and Moldawer, L. L., 2007, "Variable requirement of dendritic cells for recruitment of NK and T cells to different TLR agonists," *Journal of immunology (Baltimore, Md. : 1950)*, 178(6), pp. 3886-3892.
- [171] Zhao, J., Wohlford-Lenane, C., Zhao, J., Fleming, E., Lane, T. E., McCray, P. B., Jr., and Perlman, S., 2012, "Intranasal treatment with poly(I*C) protects aged mice from lethal respiratory virus infections," *Journal of virology*, 86(21), pp. 11416-11424.
- [172] Sherwood, J. M., Reina-Torres, E., Bertrand, J. A., Rowe, B., and Overby, D. R., 2016, "Measurement of Outflow Facility Using iPerfusion," *PLoS One*, 11(3), p. e0150694.
- [173] Davis, M. J., Scallan, J. P., Wolpers, J. H., Muthuchamy, M., Gashev, A. A., and Zawieja, D. C., 2012, "Intrinsic increase in lymphangion muscle contractility in response to elevated afterload," *American journal of physiology. Heart and circulatory physiology*, 303(7), pp. H795-808.
- [174] van Breugel, H. F., de Groot, P. G., Heethaar, R. M., and Sixma, J. J., 1992, "Role of plasma viscosity in platelet adhesion," *Blood*, 80(4), pp. 953-959.
- [175] Woodruff, M. C., Heesters, B. A., Herndon, C. N., Groom, J. R., Thomas, P. G., Luster, A. D., Turley, S. J., and Carroll, M. C., 2014, "Trans-nodal migration of resident dendritic cells into medullary interfollicular regions initiates immunity to influenza vaccine," *J Exp Med*, 211(8), pp. 1611-1621.
- [176] Umarova, B. A., Lelekova, T. V., Kopylova, G. N., Goncharova, E. L., Bakaeva, Z. V., and Samonina, G. E., 2006, "The role of protective effects of proline-containing peptides (PGP, PG, and GP) in contractile dysfunction of mesenteric lymphatic vessels in rats with experimental acute peritonitis," *Bulletin of experimental biology and medicine*, 142(3), pp. 279-282.
- [177] Wu, T. F., Carati, C. J., Macnaughton, W. K., and von der Weid, P. Y., 2006, "Contractile activity of lymphatic vessels is altered in the TNBS model of guinea pig ileitis," *American journal of physiology. Gastrointestinal and liver physiology*, 291(4), pp. G566-574.
- [178] Liao, S., Cheng, G., Conner, D. A., Huang, Y., Kucherlapati, R. S., Munn, L. L., Ruddle, N. H., Jain, R. K., Fukumura, D., and Padera, T. P., 2011, "Impaired lymphatic contraction associated with immunosuppression," *Proc Natl Acad Sci U S A*, 108(46), pp. 18784-18789.
- [179] Aldrich, M. B., and Sevick-Muraca, E. M., 2013, "Cytokines are systemic effectors of lymphatic function in acute inflammation," *Cytokine*, 64(1), pp. 362-369.
- [180] Rot, A., and von Andrian, U. H., 2004, "Chemokines in innate and adaptive host defense: basic chemokines grammar for immune cells," *Annual review of immunology*, 22, pp. 891-928.
- [181] Bardi, G., Lipp, M., Baggiolini, M., and Loetscher, P., 2001, "The T cell chemokine receptor CCR7 is internalized on stimulation with ELC, but not with SLC," *European journal of immunology*, 31(11), pp. 3291-3297.

- [182] Kohout, T. A., Nicholas, S. L., Perry, S. J., Reinhart, G., Junger, S., and Struthers, R. S., 2004, "Differential desensitization, receptor phosphorylation, beta-arrestin recruitment, and ERK1/2 activation by the two endogenous ligands for the CC chemokine receptor 7," *The Journal of biological chemistry*, 279(22), pp. 23214-23222.
- [183] Haessler, U., Pisano, M., Wu, M., and Swartz, M. A., 2011, "Dendritic cell chemotaxis in 3D under defined chemokine gradients reveals differential response to ligands CCL21 and CCL19," *Proc Natl Acad Sci U S A*, 108(14), pp. 5614-5619.
- [184] Bao, X., Moseman, E. A., Saito, H., Petryanik, B., Thiriot, A., Hatakeyama, S., Ito, Y., Kawashima, H., Yamaguchi, Y., Lowe, J. B., von Andrian, U. H., and Fukuda, M., 2010, "Endothelial Heparan Sulfate Controls Chemokine Presentation in Recruitment of Lymphocytes and Dendritic Cells to Lymph Nodes," *Immunity*, 33(5), pp. 817-829.
- [185] Love, M., Sandberg, J. L., Ziarek, J. J., Gerarden, K. P., Rode, R. R., Jensen, D. R., McCaslin, D. R., Peterson, F. C., and Veldkamp, C. T., 2012, "Solution structure of CCL21 and identification of a putative CCR7 binding site," *Biochemistry*, 51(3), pp. 733-735.
- [186] Veldkamp, C. T., Kiermaier, E., Gabel-Eissens, S. J., Gillitzer, M. L., Lippner, D. R., DiSilvio, F. A., Mueller, C. J., Wantuch, P. L., Chaffee, G. R., Famiglietti, M. W., Zgoba, D. M., Bailey, A. A., Bah, Y., Engebretson, S. J., Graupner, D. R., Lackner, E. R., LaRosa, V. D., Medeiros, T., Olson, M. L., Phillips, A. J., Pyles, H., Richard, A. M., Schoeller, S. J., Touzeau, B., Williams, L. G., Sixt, M., and Peterson, F. C., 2015, "Solution Structure of CCL19 and Identification of Overlapping CCR7 and PSGL-1 Binding Sites," *Biochemistry*, 54(27), pp. 4163-4166.
- [187] Heinzl, K., Benz, C., and Bleul, C. C., 2007, "A silent chemokine receptor regulates steady-state leukocyte homing in vivo," *Proc Natl Acad Sci U S A*, 104(20), pp. 8421-8426.
- [188] Lin, F., and Butcher, E. C., 2008, "Modeling the role of homologous receptor desensitization in cell gradient sensing," *Journal of immunology (Baltimore, Md. : 1950)*, 181(12), pp. 8335-8343.
- [189] Wang, Y., and Irvine, D. J., 2013, "Convolution of chemoattractant secretion rate, source density, and receptor desensitization direct diverse migration patterns in leukocytes," *Integrative biology : quantitative biosciences from nano to macro*, 5(3), pp. 481-494.
- [190] Ricart, B. G., John, B., Lee, D., Hunter, C. A., and Hammer, D. A., 2011, "Dendritic cells distinguish individual chemokine signals through CCR7 and CXCR4," *Journal of immunology (Baltimore, Md. : 1950)*, 186(1), pp. 53-61.
- [191] Dominguez, G. A., and Hammer, D. A., 2014, "Effect of adhesion and chemokine presentation on T-lymphocyte haptokinesis," *Integrative biology : quantitative biosciences from nano to macro*, 6(9), pp. 862-873.
- [192] Byers, M. A., Calloway, P. A., Shannon, L., Cunningham, H. D., Smith, S., Li, F., Fassold, B. C., and Vines, C. M., 2008, "Arrestin 3 mediates endocytosis of CCR7 following ligation of CCL19 but not CCL21," *Journal of immunology (Baltimore, Md. : 1950)*, 181(7), pp. 4723-4732.

- [193] Britschgi, M. R., Link, A., Lissandrin, T. K., and Luther, S. A., 2008, "Dynamic modulation of CCR7 expression and function on naive T lymphocytes in vivo," *Journal of immunology* (Baltimore, Md. : 1950), 181(11), pp. 7681-7688.
- [194] Otero, C., Groettrup, M., and Legler, D. F., 2006, "Opposite fate of endocytosed CCR7 and its ligands: recycling versus degradation," *Journal of immunology* (Baltimore, Md. : 1950), 177(4), pp. 2314-2323.
- [195] Malhotra, D., Fletcher, A. L., Astarita, J., Lukacs-Kornek, V., Tayalia, P., Gonzalez, S. F., Elpek, K. G., Chang, S. K., Knoblich, K., Hemler, M. E., Brenner, M. B., Carroll, M. C., Mooney, D. J., and Turley, S. J., 2012, "Transcriptional profiling of stroma from inflamed and resting lymph nodes defines immunological hallmarks," *Nature immunology*, 13(5), pp. 499-510.
- [196] Qi, Y., Li, X., Zhang, Q., Huang, F., Lin, D., Zhou, Y., Hong, J., Cui, B., Wang, W., Ning, G., and Wang, S., 2015, "Increased chemokine (C-C motif) ligand 21 expression and its correlation with osteopontin in Graves' disease," *Endocrine*, 50(1), pp. 123-129.
- [197] Russo, E., Teijeira, A., Vaahtomeri, K., Willrodt, A. H., Bloch, J. S., Nitschke, M., Santambrogio, L., Kerjaschki, D., Sixt, M., and Halin, C., 2016, "Intralymphatic CCL21 Promotes Tissue Egress of Dendritic Cells through Afferent Lymphatic Vessels," *Cell reports*, 14(7), pp. 1723-1734.
- [198] Scallan, J. P., and Huxley, V. H., 2010, "In vivo determination of collecting lymphatic vessel permeability to albumin: a role for lymphatics in exchange," *J Physiol*, 588(Pt 1), pp. 243-254.
- [199] Acton, S. E., Farrugia, A. J., Astarita, J. L., Mourão-Sá, D., Jenkins, R. P., Nye, E., Hooper, S., van Blijswijk, J., Rogers, N. C., Snelgrove, K. J., Rosewell, I., Moita, L. F., Stamp, G., Turley, S. J., Sahai, E., and Sousa, C. R. e., 2014, "Dendritic Cells Control Fibroblastic Reticular Network Tension and Lymph Node Expansion," *Nature*, 514(7523), pp. 498-502.
- [200] Fletcher, A. L., Malhotra, D., Acton, S. E., Lukacs-Kornek, V., Bellemare-Pelletier, A., Curry, M., Armant, M., and Turley, S. J., 2011, "Reproducible isolation of lymph node stromal cells reveals site-dependent differences in fibroblastic reticular cells," *Frontiers in immunology*, 2, p. 35.
- [201] Cilfone, N. A., Ford, C. B., Marino, S., Mattila, J. T., Gideon, H. P., Flynn, J. L., Kirschner, D. E., and Linderman, J. J., 2015, "Computational modeling predicts IL-10 control of lesion sterilization by balancing early host immunity-mediated antimicrobial responses with caseation during mycobacterium tuberculosis infection," *Journal of immunology* (Baltimore, Md. : 1950), 194(2), pp. 664-677.
- [202] Marino, S., Hogue, I. B., Ray, C. J., and Kirschner, D. E., 2008, "A methodology for performing global uncertainty and sensitivity analysis in systems biology," *J Theor Biol*, 254(1), pp. 178-196.
- [203] Estes, J. D., Thacker, T. C., Hampton, D. L., Kell, S. A., Keele, B. F., Palenske, E. A., Druey, K. M., and Burton, G. F., 2004, "Follicular dendritic cell regulation of CXCR4-

mediated germinal center CD4 T cell migration," *Journal of immunology* (Baltimore, Md. : 1950), 173(10), pp. 6169-6178.

[204] Cyster, J. G., Ansel, K. M., Reif, K., Ekland, E. H., Hyman, P. L., Tang, H. L., Luther, S. A., and Ngo, V. N., 2000, "Follicular stromal cells and lymphocyte homing to follicles," *Immunological reviews*, 176, pp. 181-193.

[205] Levick, R. J., 2009, *An Introduction to Cardiovascular Physiology 5E*, Taylor & Francis.

[206] Wang, X., Cho, B., Suzuki, K., Xu, Y., Green, J. A., An, J., and Cyster, J. G., 2011, "Follicular dendritic cells help establish follicle identity and promote B cell retention in germinal centers," *J Exp Med*, 208(12), pp. 2497-2510.

[207] Gashev, A. A., Davis, M. J., Delp, M. D., and Zawieja, D. C., 2004, "Regional variations of contractile activity in isolated rat lymphatics," *Microcirculation*, 11(6), pp. 477-492.

[208] Andrews, A. M., Jaron, D., Buerk, D. G., Kirby, P. L., and Barbee, K. A., 2010, "Direct, real-time measurement of shear stress-induced nitric oxide produced from endothelial cells in vitro," *Nitric Oxide*, 23(4), pp. 335-342.

[209] Kuchan, M. J., and Frangos, J. A., 1994, "Role of calcium and calmodulin in flow-induced nitric oxide production in endothelial cells," *The American journal of physiology*, 266(3 Pt 1), pp. C628-636.

[210] Kuchan, M. J., and Frangos, J. A., 1993, "Shear stress regulates endothelin-1 release via protein kinase C and cGMP in cultured endothelial cells," *The American journal of physiology*, 264(1 Pt 2), pp. H150-156.

[211] Dancu, M. B., Berardi, D. E., Vanden Heuvel, J. P., and Tarbell, J. M., 2007, "Atherogenic Endothelial Cell eNOS and ET-1 Responses to Asynchronous Hemodynamics are Mitigated by Conjugated Linoleic Acid," *Ann Biomed Eng*, 35(7), pp. 1111-1119.

[212] Toda, M., Yamamoto, K., Shimizu, N., Obi, S., Kumagaya, S., Igarashi, T., Kamiya, A., and Ando, J., 2008, "Differential gene responses in endothelial cells exposed to a combination of shear stress and cyclic stretch," *J Biotechnol*, 133(2), pp. 239-244.

[213] Bhagyalakshmi, A., and Frangos, J. A., 1989, "Mechanism of shear-induced prostacyclin production in endothelial cells," *Biochem Biophys Res Commun*, 158(1), pp. 31-37.

[214] Dull, R. O., and Davies, P. F., 1991, "Flow modulation of agonist (ATP)-response (Ca²⁺) coupling in vascular endothelial cells," *The American journal of physiology*, 261(1 Pt 2), pp. H149-154.

[215] Corson, M. A., James, N. L., Latta, S. E., Nerem, R. M., Berk, B. C., and Harrison, D. G., 1996, "Phosphorylation of endothelial nitric oxide synthase in response to fluid shear stress," *Circ Res*, 79(5), pp. 984-991.



- [216] Dimmeler, S., Fleming, I., Fisslthaler, B., Hermann, C., Busse, R., and Zeiher, A. M., 1999, "Activation of nitric oxide synthase in endothelial cells by Akt-dependent phosphorylation," *Nature*, 399(6736), pp. 601-605.
- [217] Tiruppathi, C., Minshall, R. D., Paria, B. C., Vogel, S. M., and Malik, A. B., 2002, "Role of Ca²⁺ signaling in the regulation of endothelial permeability," *Vascul Pharmacol*, 39(4-5), pp. 173-185.
- [218] Miteva, D. O., Rutkowski, J. M., Dixon, J. B., Kilarski, W., Shields, J. D., and Swartz, M. A., 2010, "Transmural flow modulates cell and fluid transport functions of lymphatic endothelium," *Circ Res*, 106(5), pp. 920-931.
- [219] Liu, B., Lu, S., Zheng, S., Jiang, Z., and Wang, Y., 2011, "Two distinct phases of calcium signalling under flow," *Cardiovasc Res*, 91(1), pp. 124-133.
- [220] Berk, B. C., Corson, M. A., Peterson, T. E., and Tseng, H., 1995, "Protein kinases as mediators of fluid shear stress stimulated signal transduction in endothelial cells: A hypothesis for calcium-dependent and calcium-independent events activated by flow," *Journal of Biomechanics*, 28(12), pp. 1439-1450.
- [221] Berridge, M. J., and Irvine, R. F., 1989, "Inositol phosphates and cell signalling," *Nature*, 341(6239), pp. 197-205.
- [222] Tran, Q. K., Ohashi, K., and Watanabe, H., 2000, "Calcium signalling in endothelial cells," *Cardiovasc Res*, 48(1), pp. 13-22.
- [223] Prasad, A. R., Logan, S. A., Nerem, R. M., Schwartz, C. J., and Sprague, E. A., 1993, "Flow-related responses of intracellular inositol phosphate levels in cultured aortic endothelial cells," *Circ Res*, 72(4), pp. 827-836.
- [224] Bhagyalakshmi, A., Berthiaume, F., Reich, K. M., and Frangos, J. A., 1992, "Fluid shear stress stimulates membrane phospholipid metabolism in cultured human endothelial cells," *J Vasc Res*, 29(6), pp. 443-449.
- [225] Tzima, E., Irani-Tehrani, M., Kiosses, W. B., Dejana, E., Schultz, D. A., Engelhardt, B., Cao, G., DeLisser, H., and Schwartz, M. A., 2005, "A mechanosensory complex that mediates the endothelial cell response to fluid shear stress," *Nature*, 437(7057), pp. 426-431.
- [226] Nauli, S. M., Kawanabe, Y., Kaminski, J. J., Pearce, W. J., Ingber, D. E., and Zhou, J., 2008, "Endothelial cilia are fluid shear sensors that regulate calcium signaling and nitric oxide production through polycystin-1," *Circulation*, 117(9), pp. 1161-1171.
- [227] Gudi, S., Nolan, J. P., and Frangos, J. A., 1998, "Modulation of GTPase activity of G proteins by fluid shear stress and phospholipid composition," *Proceedings of the National Academy of Sciences*, 95(5), pp. 2515-2519.
- [228] Ando, J., and Yamamoto, K., 2013, "Flow detection and calcium signalling in vascular endothelial cells," *Cardiovascular Research*, 99(2), pp. 260-268.

- [229] James, N. L., Harrison, D. G., and Nerem, R. M., 1995, "Effects of shear on endothelial cell calcium in the presence and absence of ATP," *The FASEB Journal*, 9(10), pp. 968-973.
- [230] Yamamoto, K., Korenaga, R., Kamiya, A., and Ando, J., 2000, "Fluid Shear Stress Activates Ca²⁺ Influx Into Human Endothelial Cells via P2X₄ Purinoceptors," *Circulation Research*, 87(5), pp. 385-391.
- [231] Shin, Y., Han, S., Jeon, J. S., Yamamoto, K., Zervantonakis, I. K., Sudo, R., Kamm, R. D., and Chung, S., 2012, "Microfluidic assay for simultaneous culture of multiple cell types on surfaces or within hydrogels," *Nat. Protocols*, 7(7), pp. 1247-1259.
- [232] Zheng, H., Zhou, M.-H., Hu, C., Kuo, E., Peng, X., Hu, J., Kuo, L., and Zhang, S. L., 2013, "Differential Roles of the C and N Termini of Orai1 Protein in Interacting with Stromal Interaction Molecule 1 (STIM1) for Ca²⁺ Release-activated Ca²⁺ (CRAC) Channel Activation," *Journal of Biological Chemistry*, 288(16), pp. 11263-11272.
- [233] Di Sabatino, A., Rovedatti, L., Kaur, R., Spencer, J. P., Brown, J. T., Morisset, V. D., Biancheri, P., Leakey, N. A., Wilde, J. I., Scott, L., Corazza, G. R., Lee, K., Sengupta, N., Knowles, C. H., Gunthorpe, M. J., McLean, P. G., MacDonald, T. T., and Kruidenier, L., 2009, "Targeting gut T cell Ca²⁺ release-activated Ca²⁺ channels inhibits T cell cytokine production and T-box transcription factor T-bet in inflammatory bowel disease," *Journal of immunology (Baltimore, Md. : 1950)*, 183(5), pp. 3454-3462.
- [234] Li, J., McKeown, L., Ojelabi, O., Stacey, M., Foster, R., O'Regan, D., Porter, K. E., and Beech, D. J., 2011, "Nanomolar potency and selectivity of a Ca(2)(+) release-activated Ca(2)(+) channel inhibitor against store-operated Ca(2)(+) entry and migration of vascular smooth muscle cells," *British journal of pharmacology*, 164(2), pp. 382-393.
- [235] Ng, S. W., di Capite, J., Singaravelu, K., and Parekh, A. B., 2008, "Sustained activation of the tyrosine kinase Syk by antigen in mast cells requires local Ca²⁺ influx through Ca²⁺ release-activated Ca²⁺ channels," *The Journal of biological chemistry*, 283(46), pp. 31348-31355.
- [236] Schwarz, G., Callewaert, G., Droogmans, G., and Nilius, B., 1992, "Shear stress-induced calcium transients in endothelial cells from human umbilical cord veins," *The Journal of Physiology*, 458(1), pp. 527-538.
- [237] Rahbar, E., Akl, T., Coté, G. L., Moore, J. E., and Zawieja, D. C., 2014, "Lymph transport in rat mesenteric lymphatics experiencing edemagenic stress," *Microcirculation*, pp. n/a-n/a.
- [238] Berk, D. A., Swartz, M. A., Leu, A. J., and Jain, R. K., 1996, "Transport in lymphatic capillaries. II. Microscopic velocity measurement with fluorescence photobleaching," *American Journal of Physiology - Heart and Circulatory Physiology*, 270(1), pp. H330-H337.
- [239] Bohlen, H. G., Gasheva, O. Y., and Zawieja, D. C., 2011, "Nitric oxide formation by lymphatic bulb and valves is a major regulatory component of lymphatic pumping," *American journal of physiology. Heart and circulatory physiology*, 301(5), pp. H1897-1906.

- [240] Bohlen, H. G., Wang, W., Gashev, A., Gasheva, O., and Zawieja, D., 2009, "Phasic contractions of rat mesenteric lymphatics increase basal and phasic nitric oxide generation in vivo," *American journal of physiology. Heart and circulatory physiology*, 297(4), pp. H1319-1328.
- [241] Koenigsberger, M., Sauser, R., Beny, J. L., and Meister, J. J., 2005, "Role of the endothelium on arterial vasomotion," *Biophys J*, 88(6), pp. 3845-3854.
- [242] Silva, H. S., Kapela, A., and Tsoukias, N. M., 2007, "A mathematical model of plasma membrane electrophysiology and calcium dynamics in vascular endothelial cells," *American journal of physiology. Cell physiology*, 293(1), pp. C277-293.
- [243] Wiesner, T. F., Berk, B. C., and Nerem, R. M., 1997, "A mathematical model of the cytosolic-free calcium response in endothelial cells to fluid shear stress," *Proc Natl Acad Sci U S A*, 94(8), pp. 3726-3731.
- [244] Verbeke, C. S., and Mooney, D. J., 2015, "Injectable, Pore-Forming Hydrogels for In Vivo Enrichment of Immature Dendritic Cells," *Advanced healthcare materials*, 4(17), pp. 2677-2687.
- [245] Ali, O. A., Verbeke, C., Johnson, C., Sands, R. W., Lewin, S. A., White, D., Doherty, E., Dranoff, G., and Mooney, D. J., 2014, "Identification of immune factors regulating antitumor immunity using polymeric vaccines with multiple adjuvants," *Cancer Res*, 74(6), pp. 1670-1681.
- [246] Ali, O. A., Huebsch, N., Cao, L., Dranoff, G., and Mooney, D. J., 2009, "Infection-mimicking materials to program dendritic cells in situ," *Nature materials*, 8(2), pp. 151-158.
- [247] Vinuesa, C. G., Linterman, M. A., Yu, D., and MacLennan, I. C., 2016, "Follicular Helper T Cells," *Annual review of immunology*, 34, pp. 335-368.
- [248] Verkaar, F., van Offenbeek, J., van der Lee, M. M., van Lith, L. H., Watts, A. O., Rops, A. L., Aguilar, D. C., Ziarek, J. J., van der Vlag, J., Handel, T. M., Volkman, B. F., Proudfoot, A. E., Vischer, H. F., Zaman, G. J., and Smit, M. J., 2014, "Chemokine cooperativity is caused by competitive glycosaminoglycan binding," *Journal of immunology (Baltimore, Md. : 1950)*, 192(8), pp. 3908-3914.
- [249] Lau, E. K., Paavola, C. D., Johnson, Z., Gaudry, J. P., Geretti, E., Borlat, F., Kungl, A. J., Proudfoot, A. E., and Handel, T. M., 2004, "Identification of the glycosaminoglycan binding site of the CC chemokine, MCP-1: implications for structure and function in vivo," *The Journal of biological chemistry*, 279(21), pp. 22294-22305.
- [250] Sweet, D. T., Jimenez, J. M., Chang, J., Hess, P. R., Mericko-Ishizuka, P., Fu, J., Xia, L., Davies, P. F., and Kahn, M. L., 2015, "Lymph flow regulates collecting lymphatic vessel maturation in vivo," *Journal of Clinical Investigation*, 125(8), pp. 2995-3007.

APPENDIX A

PERMISSION DOCUMENTS FOR REPRINT

From: Ballen, Karen KBallen@liebertpub.com  
Subject: RE: Request Permission to Reuse Materials in Thesis
Date: April 22, 2016 at 4:06 PM
To: Jafarnejad, Mohammad m.jafarnejad12@imperial.ac.uk



Dear Mohammad:



Copyright permission is granted for this request.



Kind regards,



Karen Ballen

Manager



From: Jafarnejad, Mohammad [<mailto:m.jafarnejad12@imperial.ac.uk>]

Sent: Friday, April 22, 2016 9:34 AM

To: Ballen, Karen

Subject: Request Permission to Reuse Materials in Thesis

Dear Madame/Sir,

I would like to request permission to use the figures and text published in my published first author paper:

Jafarnejad Mohammad, Woodruff Matthew C., Zawieja David C., Carroll Michael C., and Moore J.E. Jr. Lymphatic Research and Biology. December 2015, 13(4): 234-247. doi:10.1089/lrb.2015.0028.

In the online form there was not an option to select reuse in thesis and dissertation. I was wondering if I will have permission to reuse the material (text/figures) from my first author paper in my thesis. Please let me know.

Kind regards,
Mohammad

**Imperial College
London**

Mohammad Jafarnejad
PhD Student
Department of Bioengineering,
Imperial College London
South Kensington Campus
London SW7 2AZ
United Kingdom

+44 (0)7841 116997
m.jafarnejad12@imperial.ac.uk

Figure A.1. Permission for reprint of Chapter 2.



Title: Measurement of shear stress-mediated intracellular calcium dynamics in human dermal lymphatic endothelial cells

Author: M. Jafarnejad, W. E. Cromer, R. R. Kaunas, S. L. Zhang, D. C. Zawieja, J. E. Moore

Publication: Am J Physiol- Heart and Circulatory Physiology

Publisher: The American Physiological Society

Date: Apr 1, 2015

Logged in as:
Mohammad Jafarnejad
Account # :
3001021321

LOGOUT

Copyright © 2015, Copyright © 2015 the American Physiological Society. Licensed under Creative Commons Attribution CC-BY 3.0: © the American Physiological Society.

Permission Not Required

Permission is not required for this type of use.

BACK

CLOSE WINDOW

Copyright © 2016 Copyright Clearance Center, Inc. All Rights Reserved. [Privacy statement](#). [Terms and Conditions](#).
Comments? We would like to hear from you. E-mail us at customercare@copyright.com

Figure A.2. Permission for reprint of Chapter 5.